



STRESS ANALYSIS OF A FLEXIBLE PIPE TENSILE ARMOR WIRE DURING
AND AFTER THE END-FITTING MOUNTING

Marcelo Noboro Ralim Miyazaki

Dissertação de Mestrado apresentada ao Programa de Pós-graduação em Engenharia Civil, COPPE, da Universidade Federal do Rio de Janeiro, como parte dos requisitos necessários à obtenção do título de Mestre em Engenharia Civil.

Orientador(es): Gilberto Bruno Ellwanger

José Renato Mendes de Sousa

Rio de Janeiro
Outubro de 2015


STRESS ANALYSIS OF A FLEXIBLE PIPE TENSILE ARMOR WIRE DURING
AND AFTER THE END-FITTING MOUNTING

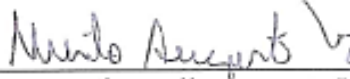
Marcelo Noboro Ralim Miyazaki

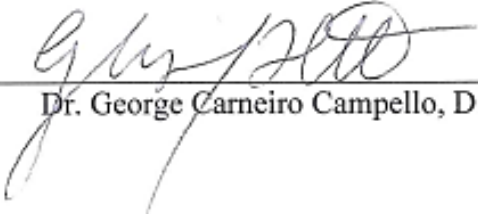
DISSERTAÇÃO SUBMETIDA AO CORPO DOCENTE DO INSTITUTO ALBERTO
LUIZ COIMBRA DE PÓS-GRADUAÇÃO E PESQUISA DE ENGENHARIA (COPPE)
DA UNIVERSIDADE FEDERAL DO RIO DE JANEIRO COMO PARTE DOS
REQUISITOS NECESSÁRIOS PARA A OBTENÇÃO DO GRAU DE MESTRE EM
CIÊNCIAS EM ENGENHARIA CIVIL.

Examinada por:


Prof. Gilberto Bruno Ellwanger, D.Sc.


Prof. José Renato Mendes de Sousa, D.Sc.


Prof. Murilo Augusto Vaz, Ph.D.


Dr. George Carneiro Campello, D.Sc.

RIO DE JANEIRO, RJ - BRASIL

OUTUBRO DE 2015

Miyazaki, Marcelo Noboro Ralim

Stress Analysis of a Flexible Pipe Tensile Armor Wire
During and After the End-Fitting Mounting / Marcelo
Noboro Ralim Miyazaki. – Rio de Janeiro: UFRJ/COPPE,
2015.

XVIII, 103 p.: il.; 29,7 cm.

Orientadores: Gilberto Bruno Ellwanger

José Renato Mendes de Sousa

Dissertação (mestrado) – UFRJ/ COPPE/ Programa de
Engenharia Civil, 2015.

Referências Bibliográficas: p. 90-93.

1. Flexible pipe. 2. End-fitting. 3. Finite element. 4. 3D
model. 5. Mounting process. I. Ellwanger, Gilberto Bruno
et al. II. Universidade Federal do Rio de Janeiro, COPPE,
Programa de Engenharia Civil. III. Título.

To my family, friends and fiancé Gabrielly.

ACKNOWLEDGEMENT

I would like to express my gratitude to my advisors José Renato Mendes de Sousa and Gilberto Bruno Ellwanger. Thanks for helping and guiding me in this study.

I want to let here my special thanks to my friends with whom I have had good discussions about this dissertation in the coffee-breaks Vinicius Ribeiro Silva, Fernando Pires, Victor Chaves, Mario Vignoles and Felipe Reis.

For the development of the models presented in this study I would like to give my sincere thanks to Pedro Kawasaki, Mario Castro, Hugo Almeida, Jerome Naturel and Dominique Bigot.

To Technip for the opportunity, especially to Roberta Pires who encouraged and gave me support to complete this master.

The last and more than special thanks goes to parents Otto Miyazaki and Esmeralda Miyazaki and to my fiancé Gabrielly Silva who have dedicated part of her time to me and have gave up of many weekends to let me work in this dissertation.

Resumo da Dissertação apresentada à COPPE/UFRJ como parte dos requisitos necessários para a obtenção do grau de Mestre em Ciências (M.Sc.)

ANÁLISE DE TENSÃO EM UM FIO DE ARMADURA DE TRAÇÃO DE UM
DUTO FLEXÍVEL DURANTE E APÓS O PROCESSO DE MONTAGEM DO
CONECTOR

Marcelo Noboro Ralim Miyazaki

Outubro/2015

Orientadores: Gilberto Bruno Ellwanger

José Renato Mendes de Sousa

Programa: Engenharia Civil

Essa dissertação apresenta dois modelos 3D em elementos finitos para análise do comportamento estrutural dos arames da armadura de tração de dutos flexíveis no interior de seus conectores. No modelo proposto, pode-se simular não só a montagem do conector, o que permite a avaliação das tensões residuais e descontinuidades geométricas impostas aos arames, como é possível considerar a ação de cargas oriundas de testes pré-operacionais e de cargas operacionais. Esse modelo em elementos finitos consiste na representação do conector e de um arame da armadura de tração do duto flexível, além de componentes auxiliares na montagem do conector tal como o gabarito de dobramento. Considera-se o comportamento não linear físico do material que forma o arame, possíveis não linearidades geométricas, além da interação entre o arame, o conector e, após a simulação da montagem, a resina que envolve o arame. Os resultados mostram que parte do processo de montagem de um conector pode ser modelado analiticamente a partir de modelos disponíveis na literatura. A geometria do arame após a montagem é descontínua e de difícil modelagem analítica. Além disso, os resultados de alívio de tensões mostram que a tensão residual varia significativamente ao longo do arame.

Abstract of Dissertation presented to COPPE/UFRJ as a partial fulfillment of the requirements for the degree of Master of Science (M.Sc.)

STRESS ANALYSIS OF A FLEXIBLE PIPE TENSILE ARMOR WIRE DURING
AND AFTER THE END-FITTING MOUNTING

Marcelo Noboro Ralim Miyazaki

October/2015

Advisors: Gilberto Bruno Ellwanger
José Renato Mendes de Sousa

Department: Civil Engineering

This dissertation presents two 3D finite based approaches of the structural behavior of the tensile armor wires of flexible pipes inside the end-fitting (EF). In the proposed model it is possible to simulate the end-fitting mounting process where the residual stresses and geometric discontinuities in the wires are evaluated. Additionally, it is possible to impose pretest and operational loadings in the tensile wires and evaluate the final residual stress along the wire. This model consists in representing the EF with one tensile armor wire of a flexible pipe and also auxiliary components as the folding collar. A non-linear behavior of the armor wire is considered for the armor wire, geometric non-linearity and the interaction between the wire with the EF and, after the mounting simulation, with the resin which involves the wire. The results presented here show that part of the EF mounting can be studied with analytical models available in the literature. The wire geometry after the mounting process is difficult to be modeled analytically due to its discontinuities. Moreover, the results of stress relief present a significant variation along the tensile armor wire inside the EF.

TABLE OF CONTENTS

CHAPTER 1 - PRESENTATION.....	1
1.1 INTRODUCTION	1
1.2 OBJECTIVE	4
1.3 SPECIFIC OBJECTIVES AND DEFINITIONS	4
1.4 DISSERTATION DESCRIPTION.....	5
CHAPTER 2 - FLEXIBLE PIPE AND END-FITTING.....	6
2.1 INTRODUCTION	6
2.2 CARCASS	7
2.3 PRESSURE SHEATH.....	9
2.4 PRESSURE ARMOR.....	10
2.6 TENSILE ARMOR.....	12
2.7 ANTI-WEAR TAPES, HIGH STRENGTH TAPES AND THERMAL INSULATION.....	13
2.9 OUTER AND PROTECTIVE SHEATHS	14
2.10 END-FITTING (EF).....	14
2.11 EF PARTS	15
2.12 END-FITTING MOUNTING PROCESS	17
CHAPTER 3 - STATE OF THE ART	22
3.1 REMARKS ON THE ANALYTICAL MODEL.....	27
3.1.1 FOLDING COLLAR RADIUS AND MAXIMUM STRAIN	27
3.1.2 STRESS DECAY INSIDE THE END-FITTING	29
3.1.3 FIRST FORMULATION	29
3.1.4 SECOND FORMULATION	31
CHAPTER 4 - 3D FINITE ELEMENT BASED APPROACH FOR LOCAL ANALYSIS INSIDE THE EF.....	32
4.1 INTRODUCTION	32
4.2 SIMULATION OF THE FOLDING/UNFOLDING PROCESS	33
4.2.1 PREMISES	33

4.2.2	GEOMETRY	33
4.2.3	FE MESH CHARACTERISTICS	34
4.2.5	BOUNDARY CONDITIONS	39
4.2.7	METHODOLOGY	40
4.4	SIMULATION OF THE STRESS RELIEF AND THE APPLICATION OF TENSILE LOADS.....	42
4.4.1	GEOMETRY	42
4.4.2	FE MESH CHARACTERISTICS	42
4.4.3	BOUNDARY CONDITIONS	44
4.4.4	METHODOLOGY	45
4.5	FEATURES TO AID THE FE MODEL CONVERGENCE	47
CHAPTER 5 - CASE STUDY		48
5.1	MATERIALS.....	48
5.2	GEOMETRIES	49
5.2.1	END-FITTING (EF) AND MODEL ASSEMBLY.....	49
5.2.2	INTERNAL TUBE AND TENSILE ARMOR WIRE	49
5.2.3	RESIN.....	50
5.2.5	FOLDING COLLAR.....	51
5.3	INTERACTION BETWEEN COMPONENTS	51
5.5	LOAD CASES.....	52
5.5.1	FOLDING/UNFOLDING SIMULATION.....	52
5.5.2	STRESS RELIEF AND OPERATIONAL LOADS.....	52
5.7	FE MESH.....	53
5.9	CONVENTIONS	54
5.10	RESULTS AND DISCUSSION.....	55
5.10.1	COLLAR RADIUS (RG) X ELLIPSE RADIUS (RE)	55
5.10.2	MESH TEST	56
5.10.3	STEP 1 TO 3 (FOLD, FREE AND UNFOLD STEPS).....	58
5.10.4	STEP 4 (TENSILE LOAD).....	69

5.10.5	STRESS RELIEF AND RESIDUAL STRESS	74
5.10.6	STRESS CONCENTRATION FACTOR, ALTERNATE AND MEAN STRESS	79
5.10.7	RESIDUAL STRESS IN R30A30, R60A30 AND R90A30 SIMULATIONS	84
CHAPTER 6 - CONCLUSIONS AND FUTURE WORKS		86
6.1	CONCLUSIONS	86
6.2	FUTURE WORKS	88
BIBLIOGRAPHY		90
APPENDIX A – SNAPSHOTS OF EACH STEP (1 TO 3) OF THE FOLDING/ UNFOLDING 3D FE MODEL		94
APPENDIX B – ONE WIRE AXISYMMETRIC VALIDATION – FE MODEL		96
APPENDIX C - CONTACT BETWEEN RESIN AND WIRE – FE MODEL		100

LIST OF FIGURES

Figure 1. Global investment in fossil fuel supply (INTERNATIONAL ENERGY AGENCY, 2014).	1
Figure 2. Fossil fuel demand (INTERNATIONAL ENERGY AGENCY, 2014).	2
Figure 3. Armor wire failure in the EF (MARINHO <i>et al.</i> , 2007).	3
Figure 4. Typical flexible pipe structure (MERINO <i>et al.</i> , 2009).	6
Figure 5. Carcass machine (BARTELL, 2015).	7
Figure 6. (a) Carcass overview; (b) Carcass profile (LAMBERT <i>et al.</i> , 2012).	8
Figure 7. Thermoplastic extrusion process (TECHNIP, 2015).	9
Figure 8. Triple layer barrier (FERNANDO <i>et al.</i> , 2013).	10
Figure 9. Pressure armor profiles: (a) Z-shape; (b) C-shape; (c) T-shape 1; (d) T-shape 2 – modified from (AMERICAN PETROLEUM INDUSTRY, 2014) – and (e) PSI (PAUMIER <i>et al.</i> , 2011).	11
Figure 10. Tensile armoring machine (BARTELL, 2015).	12
Figure 11. Flexible pipe with birdcage (BECTARTE <i>et al.</i> , 2004).	13
Figure 12. End-fitting illustration based on (BOUN <i>et al.</i> , 2005).	15
Figure 13. Different types of anchoring systems used in civil construction (LEONHARDT <i>apud</i> XAVIER, 2009).	16
Figure 14. Metallic layers blocked to avoid movement – modified from (CAMPELLO, 2014).	18
Figure 15. End-fitting mounting - folding process (TECHNIP, 2015).	18
Figure 16. Presusre armour (a) cut and (b) welding. (CAMPELLO, 2014).	19
Figure 17. (a) Front crimping ring and (b) vault positioning. (CAMPELLO, 2014)	19
Figure 18. Tensile armor wires (a) release and (b) unfold (CAMPELLO, 2014).	20
Figure 19. Anchoring and alignment of the tensile armor wires inside the EF (DAFLON, 2010).	20
Figure 20. Fastening the rear flange of the EF (DAFLON, 2010).	21
Figure 21. Resin injection after EF mounting (DAFLON, 2010).	21
Figure 22. FEA model of EF tensile wire (SHEN, <i>et al.</i> , 2008).	22
Figure 23. Three anchoring system models analysed by XAVIER (2009).	23

Figure 24. Tip of the tensile armor wire in the 2D FE model presented by CAMPELLO (2014).	26
Figure 25. Collar and ellipse radius illustration (CAMPELLO, 2014).	28
Figure 26. Illustration of a flexible line over a cylinder – modified from (BROWN, 1999).	30
Figure 27. Complete 3D FE model overview.....	32
Figure 28. General overview of the FE model parts (step 3 – unfold process).....	34
Figure 29. SOLID186 definition (ANSYS, 2014).....	34
Figure 30. First model (folding/ unfolding) – mesh images.....	35
Figure 31. CONTA174 geometry (ANSYS, 2014).	36
Figure 32. Penetration illustration between contact and target elements (ANSYS, 2014).	36
Figure 33. Friction decay illustration.	37
Figure 34. Boundary conditions of the steps 1 to 3 – folding/ unfolding FE model.	39
Figure 35. Step 1 illustration – folding process.....	40
Figure 36. Step 2 illustration – free position.	41
Figure 37. Step 3 illustration – unfolding process.....	41
Figure 38. Second 3D FE model with only one tensile armor wire.	42
Figure 39. SOLID187 definition (ANSYS, 2014).....	43
Figure 40. Second model (stress relief and loads) – mesh images.....	43
Figure 41. Boundary conditions of step 4 – folding/ unfolding model.	45
Figure 42. Step 4 illustration – stress relief.....	46
Figure 43. Carbon steel stress vs strain curve – modified from (CAMPELLO, 2014). .	48
Figure 44. EF dimensions and model assembly (dimensions in mm).	49
Figure 45. Armor wire dimensions (15x5) mm – simplified from (CAMPELLO, 2014).	50
Figure 46. (a) Illustration of the resin inside the EF: vault (red) and resin (blue); (b) Resin slice used in the simulation (shaded).....	50
Figure 47. Folding collar dimensions (mm).	51
Figure 48. Global and local conventions.	54
Figure 49. Reference points at the armor wire.	54
Figure 50. Reference points in the folding collar. (a) Isometric view and (b) section view.	55
Figure 51. Mesh test results (point N1).	57

Figure 52. Strain ratio computed with different FE meshes.....	57
Figure 53. General overview of the simulation steps - Step 1.....	59
Figure 54. Collar folding radius and folding angle results – Step 1 (maximum strain). 60	
Figure 55. General overview of the simulation steps - Step 2.....	61
Figure 56. Collar folding radius and folding angle results – Step 2 (residual stress)....	63
Figure 57. Collar folding radius and folding angle results – Step 2 (residual radius)....	63
Figure 58. General overview of the simulation steps - Step 3.....	64
Figure 59. Collar folding radius and folding angle results – Step 3 (residual radius)....	65
Figure 60. Von Mises stress along the wire’s extrados (fold and unfold positions) – simulation R60A30.....	66
Figure 61. Folding/ unfolding process VM stress.	66
Figure 62. Local stress along the wire’s extrados (fold and unfold positions) – simulation R60A30.....	67
Figure 63. General overview of the simulation steps - Step 4.....	70
Figure 64. First and second stress decay formulations results for $\tau = 0$ MPa – at point N1 and without residual stress.....	71
Figure 65. Stress decay or capstan effect results – at point N1 and without residual stress.	72
Figure 66. Residual stress results – step 4 of model R60A30.	75
Figure 67. Residual stress and stress decay curves comparison – step 4 of model R60A30.	76
Figure 68. Residual stresses along the tensile armor wire – step 4 of model R60A30. .	77
Figure 69. Stress level under different loads after stress relief (UF=82%) – point N1. .	80
Figure 70. Von Mises (VM) stress concentration factor of R60A30 (stress relief of UF=82%) – point N1.	81
Figure 71. Local (Sz) stress concentration factor of R60A30 (stress relief of UF=82%) – point N1.	81
Figure 72. Alternate and mean stress of R60A30 – point N1.	82
Figure 73. SCF of the pair maximum alternate stress with the minimum mean stress – point N1.	83
Figure 74. SCF of the pair minimum alternate stress with the maximum mean stress – point N1.	83
Figure 75. Residual stress with different collar folding radius at CHCP.	84

Figure 76. Minimum residual stress with different collar folding radius around CHCP.	85
Figure 77. Maximum residual stress with different collar folding radius around CHCP.	85
Figure 78. Boundary conditions of the axisymmetric model.	96
Figure 79. Armor wire's intrados (points I1 and I2) at the fixed point (BC-C) – axisymmetric FE model.....	97
Figure 80. Bending stress due to wire's constraint at face 1 (points E1 and E2).....	98
Figure 81. Stress comparison FE x Analytical model.	99
Figure 82. Resin x Wire FE model (dimensions in mm).....	100
Figure 83. Boundary conditions of the 'resin x wire' model	101
Figure 84. Resin x Wire contact FE model' mesh n° 3.	101
Figure 85. Thermal load result.	102
Figure 86. Axial load result.	102
Figure 87. Experimental data x 'resin x wire' model results – experimental data from (CAMPELLO, 2014).	103

LIST OF TABLES

Table 1. Planned investments (2014 – 2018) by Petrobras (PETROBRAS, 2015).....	2
Table 2. Contact among the surfaces of step 1 to 3.....	38
Table 3. Simulation steps and outputs summary.....	40
Table 4. Contact between wire and resin - step 4.....	44
Table 5. Simulation steps and outputs summary.....	46
Table 6. Carbon steel and epoxy resin characteristics (CAMPELLO, 2014).....	48
Table 7. Load cases for the first model – steps 1 to 3.	52
Table 8. Mesh characteristics – input for the mesh test.	53
Table 9. Total plastic deformation – collar radius x ellipse minimum radius.....	56
Table 10. Mesh test results – total strain (point N1).	58
Table 11. Strain results of step 1 – point N1.	60
Table 12. Residual radius and stress results of step 2 – point N1.	62
Table 13. Residual stress results for step 3 – point N1.	65
Table 14. Local stresses at the element nodes in step 1 – simulation R60A30.....	68
Table 15. Local stresses at the element nodes in step 3 – simulation R60A30.....	68
Table 16. Local stress at 530 mm (UF=0.64) – stress decay analysis without residual stress.	73
Table 17. VM at 530 mm – stress decay analysis without residual stress.....	73
Table 18. SCF of the stress decay analysis (no residual stress).	74
Table 19. Stress relief and residual stress results – step 4 of the model R60A30.....	74
Table 20. Stress relief – local stresses at the element nodes at CHCP (step 4, UF = 0.67) – simulation R60A30.....	78
Table 21. Residual stress – local stresses at the element nodes at CHCP (step 4, UF = 0.67) – simulation R60A30.	78
Table 22. Mesh characteristics – axisymmetric FE model.....	97
Table 23. Mesh characteristics – ‘resin x wire’ model.....	101

NOMENCLATURE

2D	Bi-dimensional
3D	Three-dimensional
a, b	Ellipse length parameters
AS	Axial stiffness
BC	Boundary condition
CHCP	Folding collar highest curvature point
EF	End-fitting
E&P	Exploration and production
F_0	Axial force applied on one tensile armor wire in the flexible pipe body
ff	Shape factor of the tensile armor wire
F_{sd}	Force due to stress decay inside the EF
FAT	Factory acceptance test
FCR	Folding collar radius
FE	Finite element
FEM	Finite element method
Flexible pipe's annulus	Region between the pressure sheath barrier and out an outer polymer barrier.
HIC	Hydrogen induced cracking
HDPE	High-density polyethylene
OLT	Offshore leak test
PA	Polyamide
p	Tensile armor wire perimeter

PVDF	Polyvinylidene difluoride
RAM	Random access memory
R30A10	Folding collar radius ($R = 30$ mm) and folding angle ($A = 10^\circ$)
Rg	Folding collar radius
Rr	Residual radius
Re	Ellipse radius
SCF	Stress concentration factor is the von Mises stress ratio of the tensile armor wire inside the EF and in the pipe body ($SCF = VM_{\text{Inside EF}} / VM_{\text{Tube}}$)
SR	Stress ratio of the tensile armor wire inside the EF (VM / YS)
SSC	Sulphide stress cracking
t	Tensile armor wire thickness
UF	Utilization factor of the tensile armor wire in the tube ($UF = VM / YS$)
UTS	Ultimate tensile stress
VM	Von Mises total equivalent stress
w	Tensile armor wire width
XLPE	Cross-linked polyethylene
YS	Yield stress
N1, N2	Middle point at extrados and at intrados of the tensile armor wire
B1, B2	Corners of the tensile armor wire
E1, E2	Extrados edges of the tensile armor wire
I1, I2	Intrados edges of the tensile armor wire
Sx, Sy, Sz	Element local stresses
x, y, z	Element local coordinates
X, Y, Z	Global coordinates

LIST OF SYMBOLS

τ	Shear stress
α	Armoring lay angle or folding angle.
ε	Strain
ε_y	Yield strain
φ	Angle between the tube and the EF' vault
θ	Contact angle for the capstan formulation
μ_s	Static friction coefficient
μ_d	Dynamic friction coefficient
β	Exponential decay coefficient (friction law)
v	Slip rate (friction law)
k_{Normal}	Normal stiffness
x_p	Penetration
σ_{VM}	Von Mises total equivalent stress
σ_y	Yield stress
$\mu\varepsilon$	Micro-strain
σ_{sdf}	Stress decay – formulations 1 and 2
η	Exponent of the stress decay formulation 2

CHAPTER 1

PRESENTATION

1.1 INTRODUCTION

Even with policies towards low-carbon consumption, the fossil fuels are the global primary energy used nowadays. As can be seen in Figure 1, since 2000, the invested capital in oil, gas and coal supply chain has continuously increased.

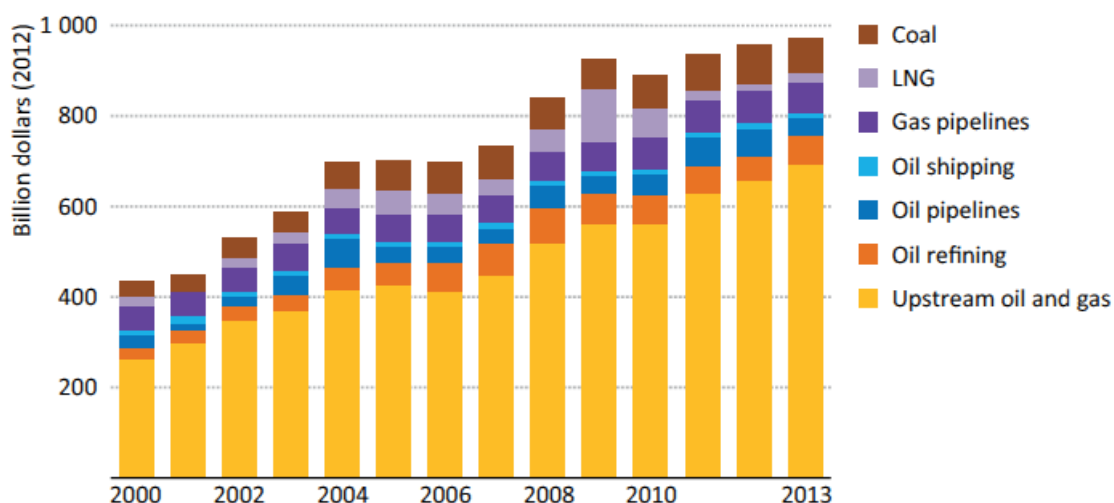


Figure 1. Global investment in fossil fuel supply (INTERNATIONAL ENERGY AGENCY, 2014).

Following the scenario of energy demand and supply projections (New Policies Scenario in Figure 2), the global demand of fossil fuel may have a significant increase until 2035. Nevertheless, following the investments associated with CO₂ emission-reduction (450 Scenario in Figure 2), the demand of fossil fuel may decrease until 2035. In this last scenario, gas is the only fossil fuel that has an increase in demand.

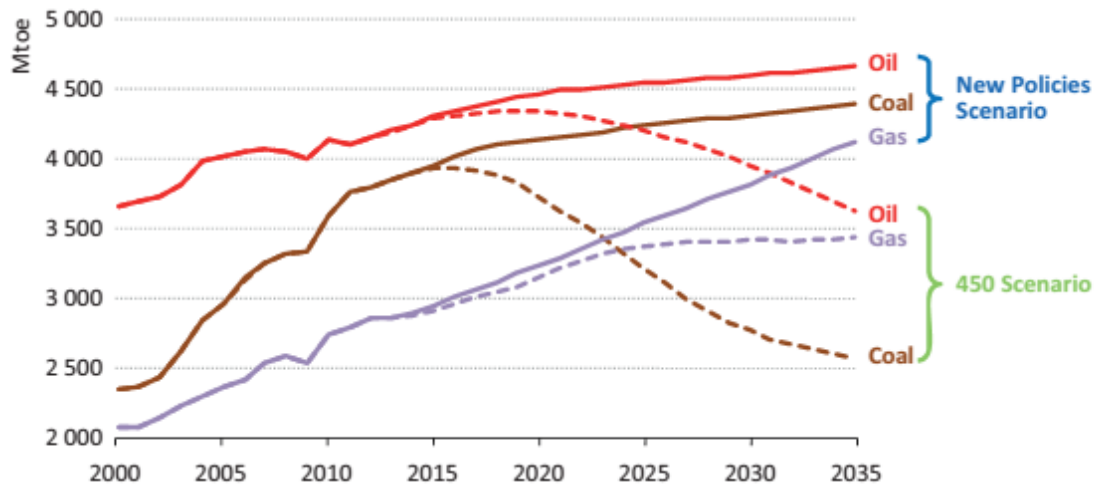


Figure 2. Fossil fuel demand (INTERNATIONAL ENERGY AGENCY, 2014).

In Brazil, studies and supply of renewable energy, such as biodiesel and ethanol, are growing. On the other hand, the investments in exploration and production of fossil fuels have also increased (Table 1). Most part of the investments (US\$ 153.9 billion) will be in exploration and production (E&P) – 73% for developing production, 15% for exploration and 12% for infrastructure – for pre-salt and post-salt fields. Until 2018, pre-salt field’s oil will correspond for 52% of total production (PETROBRAS, 2015).

Table 1. Planned investments (2014 – 2018) by Petrobras (PETROBRAS, 2015).

INVESTMENT BY SEGMENT – 2014-2018 BMP (US\$ billion)		
SEGMENT	INVESTMENT	%
E&P	153.9	69.8
Downstream	38.7	17.5
Gas & Power	10.1	4.6
International	9.7	4.4
Petrobras Biocombustível	2.3	1
Petrobras Distribuidora	2.7	1.2
Engineering, Technology and Materials	2.2	1
Other areas ¹	1	0.5
Total to be invested	220.6	100

¹ Finance, Strategic, Corporate and Services - business areas.

In the next few years, most part of the oil production in Brazil will be in deep or ultra-deep waters. The oil industry faces new challenges in deeper water depths such as

structural components, *e. g.*, flexible pipes, responsible for the transport of fluids from the well to the platform.

Flexible pipes are multilayer structures widely used on offshore applications. Its main function is to transport fluids between the well and the production platform. These pipes have accessories such as buoyancies, bend restrictors, bend stiffeners and end-fittings. This last one has an important role as a structural component since it is responsible for the connection between flexible pipes and the platform, manifold, etc.

One of the main problems when reaching deeper water depths is the top tension. The flexible pipe and its accessories must resist to high dynamic loads during their service lives, which are, typically, about 20 years or more. A critical region in the system is the end-fitting (EF) rear area (white arrow in Figure 3), where some failures were reported from the field as presented by MARINHO *et al.* (2007). The EF rear area sees a high plastification level during the mounting process due to an uncontrolled folding/ unfolding process, which may significantly reduce the service life of the flexible pipe.



Figure 3. Armor wire failure in the EF (MARINHO *et al.*, 2007).

Due to the importance of this accessory to the flexible pipe well-functioning, some studies devoted to predict the structural response of the tensile armors inside end-fittings have already been published in the public literature, but they are still only a few. Most of the works presented 2D finite element (FE) approaches aiming to assess the residual stresses due to the folding and unfolding process and/or predict the stresses in the tensile armors inside end-fittings. Recently, an analytical methodology to assess the stresses and the fatigue damage in the critical region of the end-fitting (rear area where the tensile

armor wires are folded during the mounting process) have also been proposed (CAMPELLO, 2014).

In the public literature, as far as the author knowledge, there is a complete lack of 3D models to access the wire behavior inside the EF. The use of a 3D FE based approach would possibly allow a better understanding of each step of the EF mounting process and tensile loads applications. Capture 3D effects along the tensile armor wire inside the EF would allow the complement of an analytical model for stress decay, stress relief, residual stress, load amplification due to wire geometry discontinuity etc.

1.2 OBJECTIVE

This dissertation aims to present a 3D approach to predict the stresses in the tensile armor wires inside the end-fitting of a typical flexible pipe. This 3D approach relies on two different 3D FE models and combines the residual stress from the end-fitting mounting, after stress relief (a factory acceptance test or an offshore leak test), with the tensile loads that a flexible pipe is subjected during its service life.

1.3 SPECIFIC OBJECTIVES AND DEFINITIONS

Here is detailed the specific objectives of the proposed FE approach.

In the analyses presented in this dissertation, the first FE model presents three different folding collars (see definition in chapter IV or item 5.2.4), which are simulated (30, 60 and 90 mm) combined with three different folding angles (force direction applied on the wire during the wire's folding process): 10°, 20° and 30°. The results from the folding and unfolding process are compared to those from analytical models in terms of maximum strain/ stress, residual stress and residual radius. Moreover, the final radius and residual stress of the tensile armor wire inside the EF are also obtained

The second FE model presents the tensile loads ranging from a utilization factor (UF) of 30% up to 91% - maximum load presented by (AMERICAN PETROLEUM INDUSTRY, 2009) – applied considering a folding angle of 30°. The expected results in this step are the stress decrease inside the EF, the stress ratio (SR) and the stress concentration factor (SCF).

It is important to remark that the SR is the ratio between the von Mises stress in the wire inside the EF and the yield stress of this wire, while the SCF is the ratio between the von Mises stress in the wire inside the EF and the stress in the wire outside the EF (i.e. in the flexible pipe body).

Additionally, the models names are based by letters as ‘G’ (model generation), ‘R’ (folding radius) and ‘A’ (folding angle); *e. g.* G3R60A30 (model third generation, collar radius with 60 mm and folding angle of 30°).

1.4 DISSERTATION DESCRIPTION

This section describes the contents of each chapter of this dissertation.

Chapter two of this work starts with a short description of the flexible pipe layers (carcass, pressure sheath, pressure armor, tensile armor, anti-wear and high strength tapes, thermal insulation, outer and protective sheaths) and the description of the end-fitting parts and its mounting process.

Chapter three presents the state of the art about local analysis inside the end-fitting. Also, a short description of the analytical models available in the literature is detailed. Those models are compared with the 3D FE based approach.

Chapter four describes the 3D FE based approach general characteristics such as elements, contacts, formulations and features to aid in convergence. Here, it is presented the two proposed models of the 3D FE based approach with its premises; steps of the simulations; outputs, boundary conditions and mesh used in each model.

Chapter five describes the material, the geometric characteristics of the components involved, the conventions adopted and the load cases.

Chapter six presents the results a case study involving also different folding collar radius and, when possible, the results obtained are compared with those calculated by a previously presented analytical approach.

Finally, in chapter seven, the main conclusions of this work are stated with some proposals for future works.

CHAPTER 2

FLEXIBLE PIPE AND END-FITTING

2.1 INTRODUCTION

A flexible pipe is a structure composed of several layers. Each layer has a defined mechanical function, i.e. sealing, structural, thermal insulation, protection etc. Depending on their function, these layers may be composed of polymer or steel. Each metallic and polymeric layer has specific characteristics in order to resist the local environmental conditions (pH, pressure, temperature etc).

An unbonded flexible pipe can work in different conditions of tensile load, crushing, bending, internal and external pressures. Depending on the application (water injection, production, gas injection or gas export), the number of layers and their main characteristics can be adjusted, which permits supplying flexible pipes that fits with a specific desired application.

A typical unbonded flexible pipe structure is composed of inner carcass, pressure sheath, pressure armor, tensile armor, anti-wear tapes and external sheath. An illustration of such structure is presented in Figure 4.

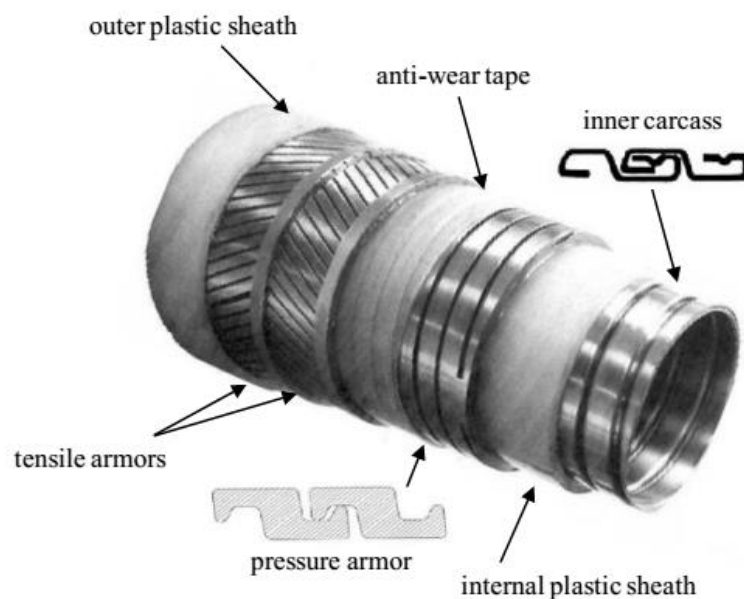


Figure 4. Typical flexible pipe structure (MERINO *et al.*, 2009).

Hereafter, the typical layers of a flexible pipe are described focusing on their structural functions, section profiles and materials.

2.2 CARCASS

Normally, the carcass is the innermost layer of a flexible pipe structure. It is very flexible and has no resistance to tension, only to radial loads as external loads (hydrostatic pressure and crushing during the installation process). This flexibility is due to its geometry, which is constructed with metallic strips shaped into a fully interlocked section in several steps. Figure 5 shows a carcass machine with several forming rolls that progressively changes the flat strip into an interlocked section, as presented in Figure 6. The lay angle of a typical carcass is near 90° . Although the cross-section of the carcass seems to be locked (Figure 6), internal clearances between the interlocked sections allow the carcass to move axially.

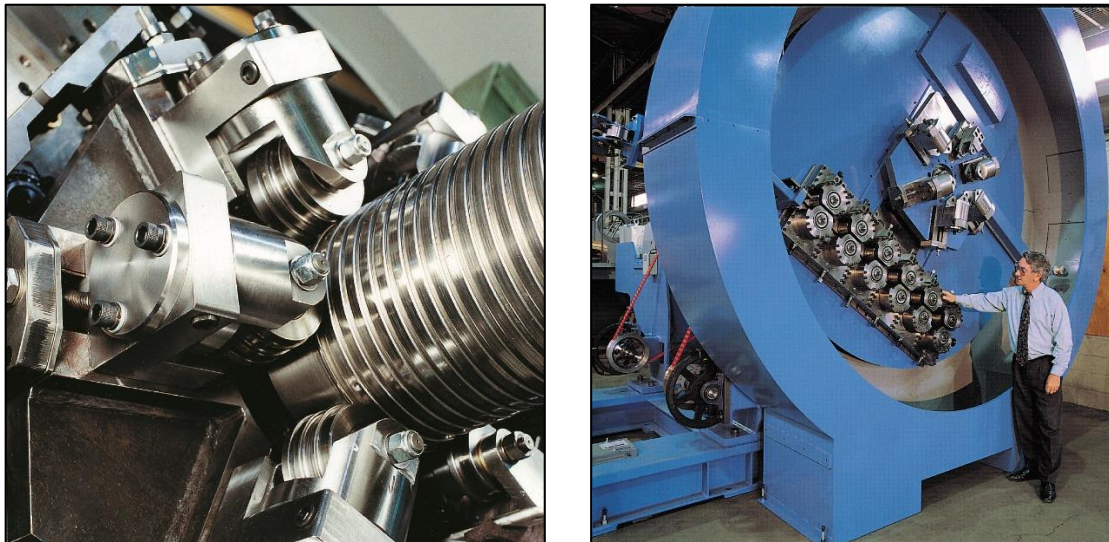


Figure 5. Carcass machine (BARTELL, 2015).

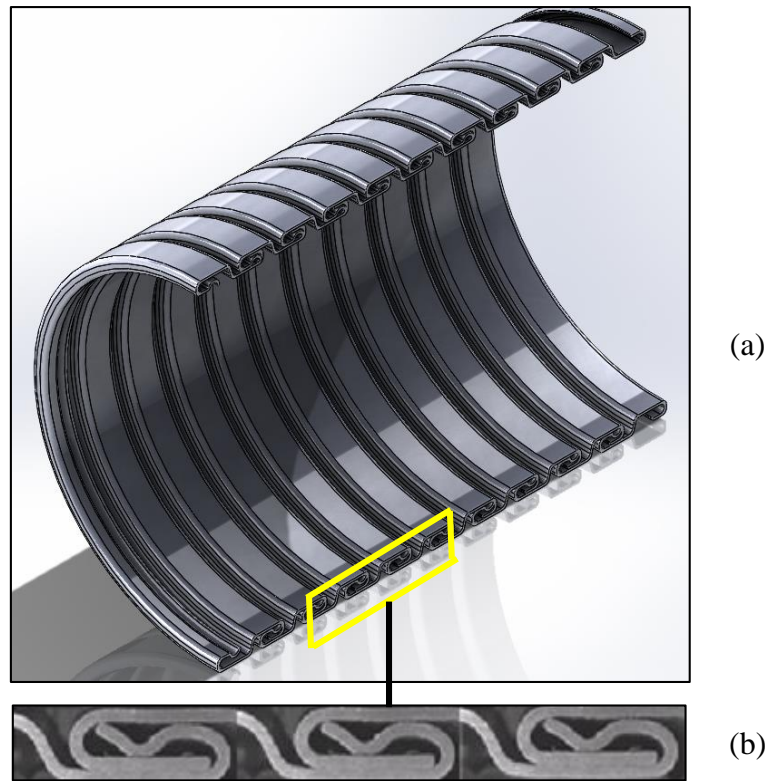


Figure 6. (a) Carcass overview; (b) Carcass profile (LAMBERT *et al.*, 2012).

The carcass main functions are to resist:

- Collapse due to external pressure applied on the pressure sheath.
- Collapse due to sudden pressure drop. This, normally, can happen when there is gas in the fluid.
- Crushing loads during installation process.
- Erosion due to solid particles transported in the fluid (i.e. sand, rock).
- Wear due to tool passing inside the pipe (i.e. pigs, workover equipment).
- SSC, HIC, hydrogen embrittlement and corrosion.

The carcass design depends on the application (transported fluid), the radial loads (collapse, crushing, sudden pressure drop) imposed on the layer and the erosion, wear and corrosion caused by the transported fluid as well as its temperature and pH. The materials typically used for carcasses, according to (AMERICAN PETROLEUM INDUSTRY, 2014), are:

- Carbon steel.
- Ferritic stainless steel (AISI 409 and AISI 430).
- Austenitic stainless steel (AISI 304, 304L, 316 and 316L).

- High-alloyed stainless steel (Duplex UNS S31803).
- Nickel-based alloys (such as N08825).

2.3 PRESSURE SHEATH

The pressure sheath is a polymeric layer that is normally extruded over the carcass. The polymer extrusion process, as shown in Figure 7, is continuous. In order to avoid any mechanical property loss, the extrusion temperature and sheath thickness are respected within narrow manufacturing tolerances.

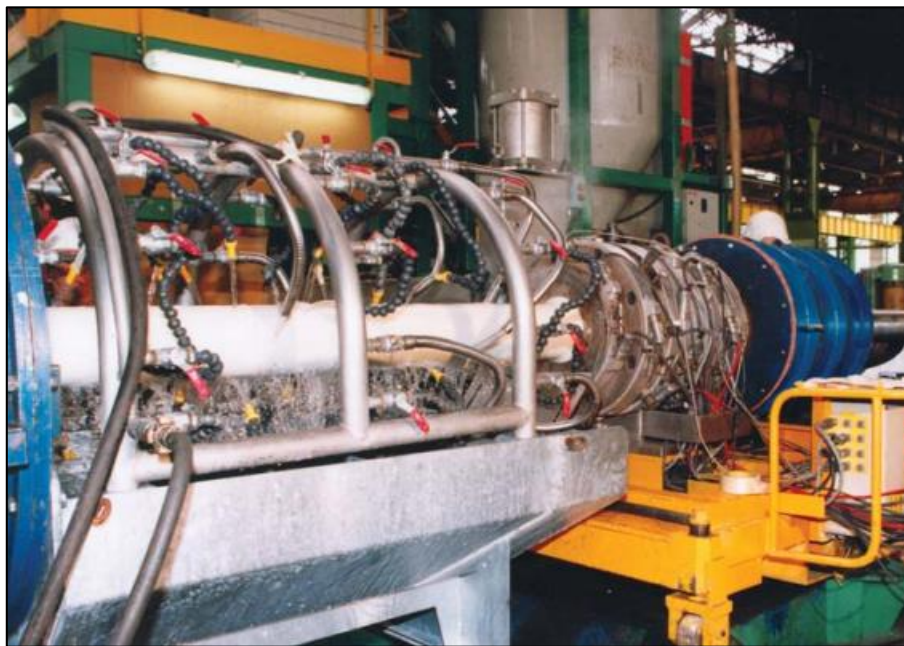


Figure 7. Thermoplastic extrusion process (TECHNIP, 2015).

The main functions of the pressure sheath are:

- Seal the flexible pipe, *i. e.*, no leak is acceptable on this sheath.
- Reduce the diffusion of corrosive gases into the flexible pipe's annulus (region between the pressure sheath barrier and out an outer polymer barrier).

It may be composed of one or more layers. The number of layers depends on the mechanical behavior of the material. Normally, the first or third layer is a sacrificial

sheath that extrudes into the carcass or pressure armor gaps due to creep and may receive the mechanical loads at that region. Those layers are not tight, different from the second barrier. Figure 8 illustrates the sacrificial sheaths extruding into the gaps of the carcass and pressure armor layers. Hence, any damage or crack in those layers (first or third one) should not propagate to the second layer –the fluid barrier in Figure 8.

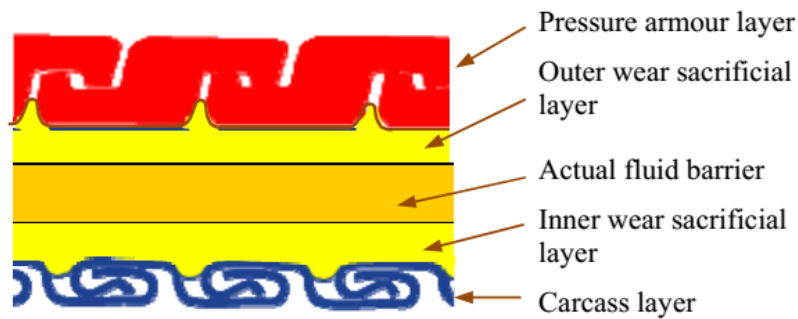


Figure 8. Triple layer barrier (FERNANDO *et al.*, 2013).

The design of the pressure sheath depends on the fluid composition (pH, temperature, pressure, and gases), polymer aging, loads and permeation characteristics. The materials typically used for pressure sheaths are HDPE, XLPE, PA-11, PVDF (AMERICAN PETROLEUM INDUSTRY, 2014).

2.4 PRESSURE ARMOR

Differently from the carcass, there are several different profiles of pressure armor. The most common one is the zeta profile (Figure 9; a). There are also others profiles, as presented in Figure 9. On the other hand, analogously to the carcass, the pressure armor has no resistance to tension, this layer only resist radial loads. It is usually composed of two profiled wires with a lay angle of, approximately, 90°.

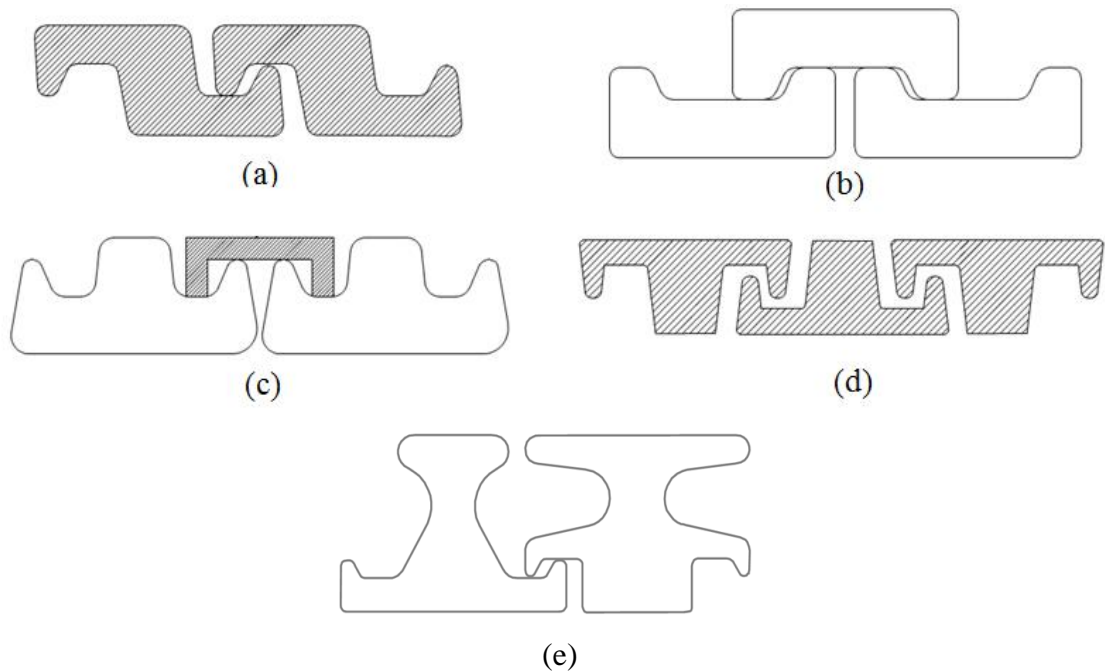


Figure 9. Pressure armor profiles: (a) Z-shape; (b) C-shape; (c) T-shape 1; (d) T-shape 2 – modified from (AMERICAN PETROLEUM INDUSTRY, 2014) – and (e) PSI (PAUMIER *et al.*, 2011).

The pressure armor main functions are resist:

- Internal pressure.
- Crushing loads during installation process.
- Collapse, when external pressure is applied on an outer sealed sheath.

The design of the pressure armor depends on the flexible pipe's annulus conditions (pH, temperature, corrosive gases) and on the loads imposed on this layer. It may be composed of one or two layers. The second layer may be a spiral (wire with circular cross section) that gives more resistance to radial loads. The typical material for the pressure armor is high carbon steel.

2.6 TENSILE ARMOR

In a flexible pipe, the tensile armor layer is the only layer that resists to tensile loads. Its profile is simpler than the carcass or the pressure armor profiles. It is a flat wire with curved edges. Depending on the flexible pipe manufacturer this profile may have slight changes on the shape. Depending on the load and application the lay angle may vary between 20° to 55°. It can be composed of two or four layers. The typical material for the tensile armor wires is carbon steel.

The tensile armoring machine (Figure 10) is used to position the tensile armor wires on the flexible pipe. Normally, two armoring machines lay the wires of each tensile armor layer in opposite directions.

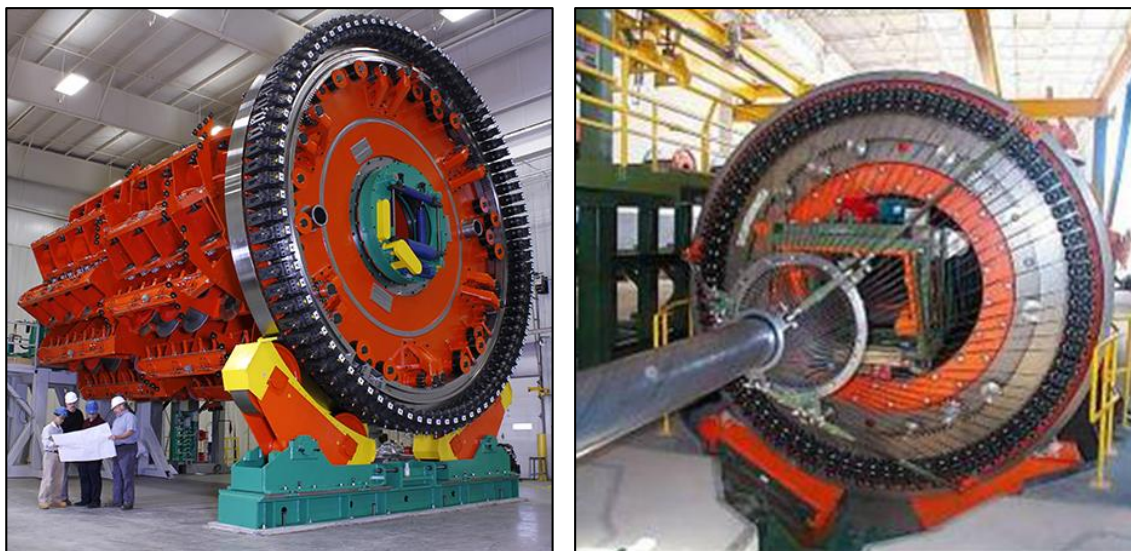


Figure 10. Tensile armoring machine (BARTELL, 2015).

Analogously to the pressure armor, the design of the tensile armor wires (and of the layers) depends on the flexible pipe's annulus conditions (pH, temperature, corrosive gases) and on the loads imposed on the pipe.

One of the main failure mode of this layer occurs inside the end-fitting. The tensile armor wire inside the end-fitting has presented failures during service life according to MARINHO *et al.*, (2007). This failure mode is the focus of this dissertation.

2.7 ANTI-WEAR TAPES, HIGH STRENGTH TAPES AND THERMAL INSULATION

Anti-wear tapes, high strength tapes and thermal insulation are made of polymeric materials. The anti-wear tapes have no structural function whereas high strength tapes sustain the radial displacements of the tensile armor layers therefore avoiding, for example, the failure mode known as ‘birdcage’ (Figure 11).



Figure 11. Flexible pipe with birdcage (BECTARTE *et al.*, 2004).

The anti-wear tapes design is based on the minimum thickness to avoid the contact between two metallic layers due to tensile loads, internal and external pressures etc.

If the fluid temperature inside the flexible pipe is to be maintained at a particular level, thermal insulation layers may be added to the flexible pipe. The insulating material to be used should be compatible with the annulus conditions. Sometimes the insulation layer annulus is flooded in order to reduce the pressure end cap effect.

2.9 OUTER AND PROTECTIVE SHEATHS

The outer sheath main function is to protect the flexible from seawater ingress, wear and mechanical damage during installation process or during the service life. It is sealed in the end-fitting and provides bending stiffness to the flexible pipe.

A protective sheath may also be placed above the outer sheath in order to have a redundancy and increase the protection from external mechanical loads. Different from the outer sheath, the protective sheath is not leak-proof, but it contributes to the bending stiffness of the flexible pipe.

2.10 END-FITTING (EF)

The EF is the structural interface between flexible pipes and/or between flexible pipe and bend stiffeners (for stiffener attached configuration) or bend restrictors with the support of the platform. The EF must sustain all axial loads from the flexible pipe. The loads are transferred from the tensile armor wires to the resin inside the EF only by contact and with a short anchoring system at the tip of the armor wires (examples in Figure 12 point '2' and Figure 13). At the EF rear region (see Figure 12 point '7'), the tensile armor wire is folded during the mounting process making this region a critical one due to the particular shape and high level of plastification and residual stress (see Figure 3).

The EF is designed as a reliable termination for all pipe layers such that leakage, structural deformation or pull-out of wires or extruded layers do not occur during the service life of the pipe. The end-fittings shall be designed for the thermal and pressure cycles defined for the service conditions of the particular dynamic or static application. The design shall take into account supporting loads from any ancillary components attached to the end-fitting, including bend stiffeners and shall ensure sealing of the internal pressure sheath and of the outer sheath. The crimping/sealing mechanism shall also ensure that the combined strain induced by the in-service pullout forces and installation of the end-fitting seal ring does not result in failure of the sheath over the service life. In addition, the axial movements of the carcass relative to the end-fitting shall be mechanically restrained (AMERICAN PETROLEUM INDUSTRY, 2009).

The typical material for the end-fitting components are AISI 4130 or alloyed stainless steel. (AMERICAN PETROLEUM INDUSTRY, 2014)

2.11 EF PARTS

Almost all EF parts are made of steel except for the epoxy resin, which fills the free space inside the EF.

Figure 12 is a typical EF composed of a front sealing system and a rear sealing system. The main EF parts are detailed next – the numbers in Figure 12 are associated with the subsequent items.

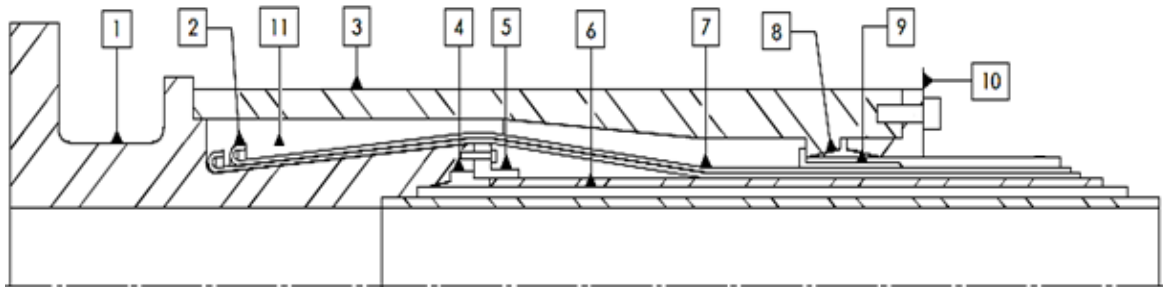


Figure 12. End-fitting illustration based on (BOUN *et al.*, 2005).

1 - Vault

The vault main functions are to receive the mechanical loads from the flexible pipe; interface with other connections (flange); hold the carcass and pressure armor tip; anchor the tensile armor wires (point 2 in Figure 12); and deform the front crimping ring (point 4 in Figure 12) in order to seal the pressure sheath.

2 - Anchoring system

The anchoring system is similar to the civil construction anchoring systems, as presented in Figure 13. Some anchoring geometries are patents of certain flexible pipe manufacturers. Its main function is to anchor the tensile armor wire inside the epoxy resin to avoid slip of the wire in the resin and helps in the capstan effect, which is the hold effort when an axial load is applied on a flexible line laid on a cylinder (more details about the capstan effect is available in item 3.1.3).

8 - Rear crimping ring

This piece is radially deformed and crushes the outer sheath ensuring the external sealing.

9 - Sleeve

The sleeve holds all compression effort from the rear-crimping.

10 - Rear flange

The rear flange is screwed to the cover and, therefore, the rear-crimping ring is deformed thus ensuring the external sealing.

11 - Epoxy resin

The epoxy resin fills the voids inside the EF.

2.12 END-FITTING MOUNTING PROCESS

Some points about the EF mounting process were mentioned in the previous item, but, hereafter, a typical EF mounting process is detailed step by step. Starting from the cutting of the polymeric layers and ending at the resin injection inside the EF.

Step 1 Cut all layers in order to access the innermost layers. Due to the high residual stresses in the metallic layers, they must be blocked with metallic tapes or welding. The arrows in Figure 14 point an example of (a) the tensile armor layer blocked with metallic tapes and (b) the pressure armor layer welded to avoid any movement.

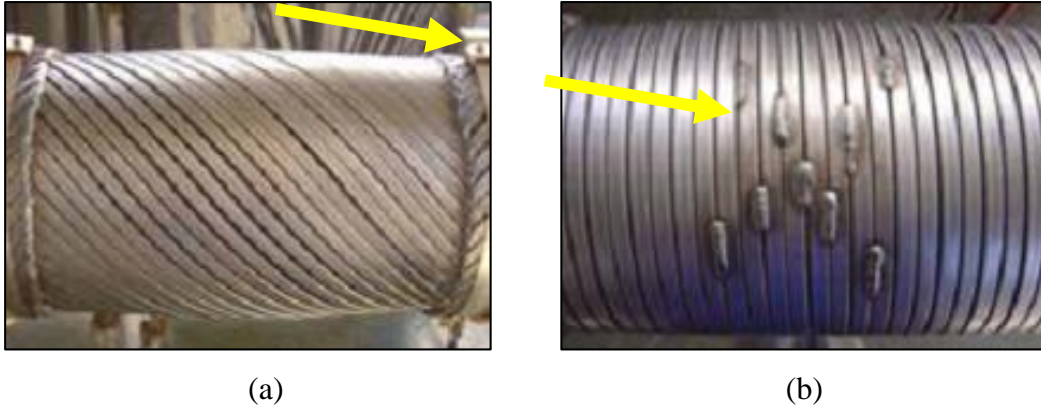


Figure 14. Metallic layers blocked to avoid movement – modified from (CAMPELLO, 2014).

Step 2 The rear flange, rear-crimping ring and the cover are the last pieces to be mounted, but they have to be positioned before the mounting start because of the radial interferences (rear-crimping ring, rear flange and cover internal diameters are, normally, smaller than the vault external diameter – see Figure 12).

Step 3 Insert the sleeve underneath the outer sheath (see Figure 12).

Step 4 Fold the tensile armor wires (Figure 15) in order to perform the machining of the pressure sheath and then the internal sealing. This step induces high plastic deformation in the tensile armor wires. A folding collar may be used in this step in order to control the folding radius and consequently control the maximum strain. Usually, the folding angle is the armoring lay angle.



Figure 15. End-fitting mounting - folding process (TECHNIP, 2015).

Step 5 In Figure 16, the weld to block any movement of the pressure armor is shown. After that, a fine cut is made in order to have a good clearance between the pressure armor and the vault.



Figure 16. Presusre armour (a) cut and (b) welding. (CAMPELLO, 2014)

Step 6 Positioning of the front flange on the pressure armor (Figure 17, (a)).

Step 7 In Figure 17, (a) positioning the front crimping ring; and (b) fastening the screws to the vault while the front-crimping ring is deformed to ensure the internal sealing.



(a)



(b)

Figure 17. (a) Front crimping ring and (b) vault positioning. (CAMPELLO, 2014)

Step 8 Figure 18 (a) shows the release of the tensile armor wires and Figure 18 (b) presents the wire unfold on the vault. Similar to step 4, this step also

induces high deformation. Normally, the tensile armor wires are unfolded following the armoring lay angle.



(a)

(b)

Figure 18. Tensile armor wires (a) release and (b) unfold (CAMPELLO, 2014).

Step 9 Make the anchoring system and alignment of the tensile armor wires (Figure 19).



Figure 19. Anchoring and alignment of the tensile armor wires inside the EF (DAFLON, 2010).

Step 10 Fastening the cover to the vault.

Step 11 Positioning of the rear-crimping ring behind the cover (Figure 20).

Step 12 Fastening the screws to the rear flange (red ellipse in Figure 20) in order to perform the external sealing and close the EF.



Figure 20. Fastening the rear flange of the EF (DAFLON, 2010).

Step 13 The last step is to inject the epoxy resin inside the EF and wait its cure. Figure 21 is an example of resin injected manually inside the EF. Usually, a machine is used to perform this task.



Figure 21. Resin injection after EF mounting (DAFLON, 2010).

CHAPTER 3

STATE OF THE ART

SHEN *et al.* (2008) presented the first study about the tensile armor wire behavior inside the end-fitting with a 3D finite element (FE) model based on the commercial software ANSYS® with non-linear materials; 3D finite elements were used to model the tensile armor wire and the resin, while the contact between them is ensured by 3D surface contact and target elements. Initially, the FE model was divided in fully bonded (close to the tensile armor anchoring system – regions 3 and 4 in Figure 22) and fully debonded regions (at EF rear region – regions 2 and 3 in Figure 22).

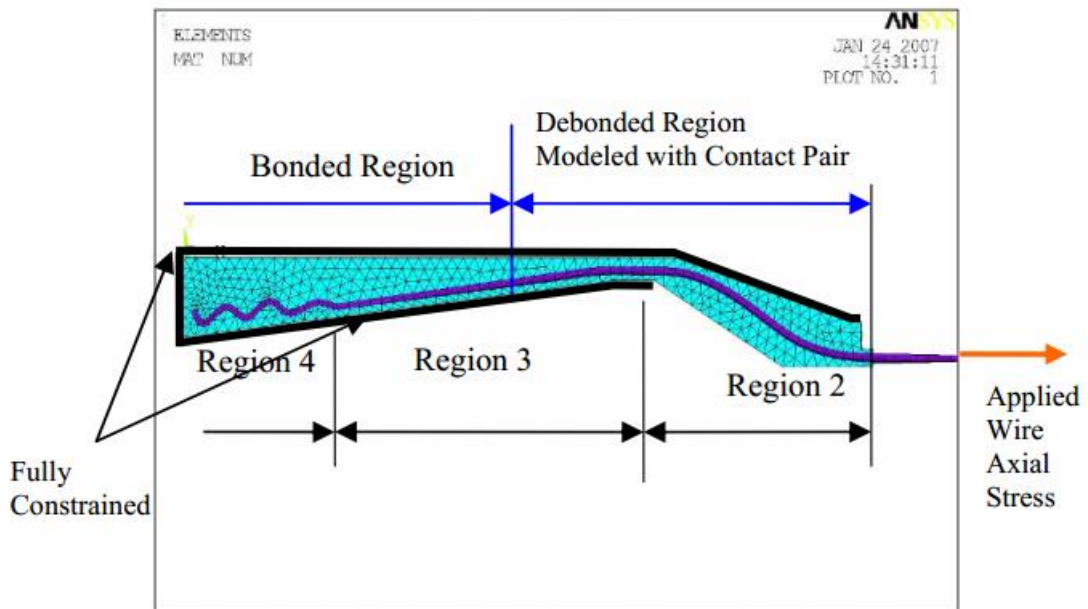


Figure 22. FEA model of EF tensile wire (SHEN, et al., 2008).

Sensitivity analyses showed that the stress decays quickly with a fully bonded model and with a fully unbonded model the stress decays slowly bearing the anchoring region. The folding/ unfolding process was also simulated and the results showed that folding angles between 70° and 110° do not change – significantly – the stresses along the tensile armor wire during both steps (folding and unfolding). At last, a fatigue small-scale test (same of the 2D FE model) was performed to compare with the 2D FE model results. No debonding was observed in the small-scale test until attain a fatigue damage

of '1'. For that reason, the boundary condition of the 2D FE model was defined as fully bonded and then the calculated damage was between '1.30' and '1.35'.

It is worth remarking that, even though 3D finite elements were used, the model proposed by SHEN *et al.* (2008) represents a projection of one tensile armor wire in a plane and, therefore, can be seen as an almost 2D FE model.

DAFLON (2009) studied the adhesion between resin and tensile armor wire without and with surface treatment. For the first case, no adhesion rupture was observed in the interface 'wire/ resin' and the shear stress for this case was approximately 2,5 MPa. For the second case, adhesion was observed and the shear stress was approximately 19 MPa. In the second part of the work, DAFLON (2009) studied the adhesion between resin and tensile armor wire in a complete EF with a short length of flexible pipe. The shear stress results for that case were between 7,5 and 14,8 MPa.

XAVIER (2009) analyzed three tensile armor anchoring models. Two of them had anchoring systems from different flexible pipe suppliers and the third one was a new anchoring system proposed in the work. Figure 23 presents the three configurations and the third one was the one proposed by XAVIER (2009).

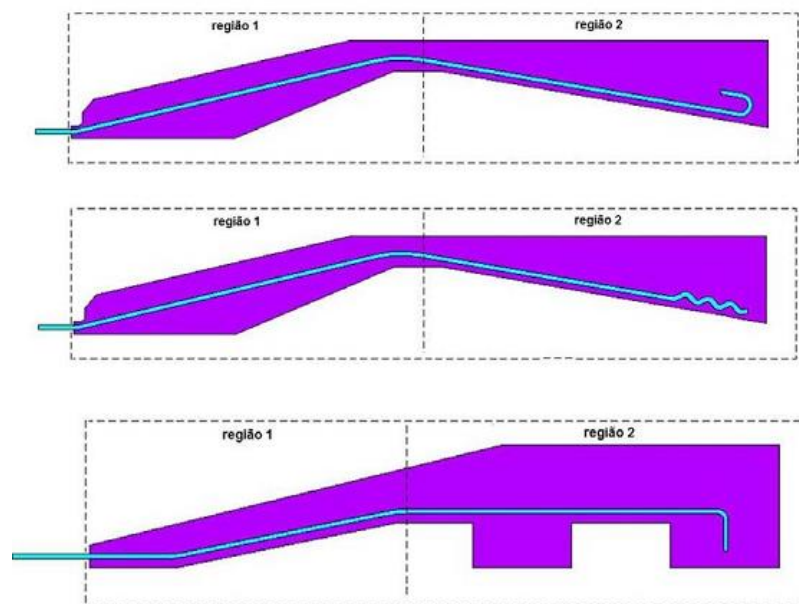


Figure 23. Three anchoring system models analysed by XAVIER (2009).

The study was based on a 2D FE model using the commercial software ANSYS® with quadratic 2D elements and was also validated by mid-scale and full-scale tests. Similar to SHEN *et al.* (2008), three different types of contact between the wire and the resin were considered: 1) Wire fully bonded to the resin; 2) Wire partially bonded to the resin (50% of the wire's length was unbonded); 3) Wire unbonded to the resin. In all these three configurations (1, 2 and 3), the new anchoring model presented reductions in the stress concentration factor (SCF) – except for the configuration 3 – and in the resin stress up to 19% and 72%, respectively. The difference between the 2D FE model and the mid-scale test was less than 3.7%. The full-scale test (prototype of the proposed anchoring model) presented no failures at the anchoring region.

BUENO (2010) completed the study of XAVIER (2009) by performing a 3D FE analysis of the full-scale test (prototype). The model was developed in the commercial software ANSYS® and it was modelled with 3D quadratic hexahedral and tetrahedral elements. For the contact, 3D contact and target elements were used. Several sensitivity analyses were performed in order to simplify the model, *i.e.*, transforming carcass, pressure armor and internal tensile armor layer into shell elements and reducing the number of external tensile armor wires. After the sensibility study the external layer was simplified and modeled with only 8 wires. This simplified 3D FE model was used to perform all subsequent analyses. The 3D FE model results were compared with FRAES (BATISTA *apud* BUENO (2010)) and results agreed quite well. The SCF predicted by the 3D FE model was comparable to the one presented by XAVIER (2009).

CAMPELLO *et al.* (2012) presented a new concept of foldless end-fitting with an innovative front sealing, where there was no need to fold or to unfold the tensile armor wires during the EF mounting process. In this work an analytical formulation of the anchoring mechanism was presented. In addition, the stress concentration factor (SCF) along the wire inside the end-fitting of the conventional and foldless EF were compared with a 2D FE model and mid-scale tests. This 2D FE model and the mid-scale test results were similar. Based on the results, the conventional EF presented a pronounced bending at the EF entrance due to its deformed geometry (residual curvature due to folding/unfolding process). Moreover, the SCF in the conventional EF was close to 2.4 and in the foldless EF was about 1.4. However, it should be remarked that, in a 2D FE model, 3D

effects, such as the capstan effect, are not accounted and this effect may contribute significantly on the resistance of the tensile armor wires.

SOUSA *et al.* (2013) proposed a 2D FE approach to estimate the stresses inside the EF due the folding/ unfolding process during the EF mounting and also due to pretests or operational loads imposed on the tensile armor wire inside the EF. Two FE models were developed, one for the folding/ unfolding process and one for the pretests or operational loads. Both FE models were implemented in a computational program named RESERCON, which generates the FE meshes to run in the commercial software ANSYS®. In this work, three aspects were investigated: the contact conditions between the resin and the wire (friction coefficient and adhesion); the stress relief levels resultant from the factory acceptance test (FAT) and/or from the offshore leak test (OLT); and the variation of resin elastic properties. This study pointed that the plasticized region (EF rear region) due the folding/ unfolding process is significantly affected by the friction coefficient, adhesion, stress relief and resin elastic properties. Moreover, adhesion values higher than 3,0 MPa, significantly decrease the SCF along the wire – mainly at the anchoring region. Different values of friction coefficient did not alter much the SCF at the EF rear region (folding/ unfolding region), but high values of friction coefficient decrease the stresses at the anchoring region. Both cases (adhesion and friction coefficient) have an important impact on the axial stiffness (AS). The stress relief of the wire after the folding/ unfolding process with a FAT or OLT was also analyzed and a significant impact on the SCF and AS after the stress relief was observed. High pressures in the FAT led to lower residual stress and higher AS. Finally, the resin Young modulus influence on the SFC and AS was studied, which had no much impact on the SCF, but a significant impact on the AS was observed, *i. e.*, higher values of Young modulus led to higher AS.

CAMPELLO (2014) validated the new concept of foldless EF with an innovative internal sealing, where there is no folding/ unfolding process of the tensile armor wires during the EF mounting process. Moreover, a complete study of the tensile armor wires inside the end-fitting during the EF mounting process was presented. In this study, an analytical methodology and a 2D FE model were formulated in order to evaluate the stresses during the EF mounting. The analytical formulation takes into account many effects that leads to an increase of the strain/stress in the tensile armor wire due to the

folding/ unfolding process. The point with maximum strain/ stress during the folding process was used as reference point to calculate all stresses during all EF mounting steps. One remark may be made about the premise of the residual curvature after unfold process, which is modeled after the spring back of the folding process. The residual curvature due to spring-back is higher than the one after the unfolding process, which leads to a higher stresses at the EF rear region. The 2D FE model was developed in the commercial software Abaqus® with non-linear material law for the tensile armor wire using quadratic elements. For the resin triangular and quadratic elements were used. This 2D FE model presented by CAMPELLO (2014) followed the EF mounting main steps as: folding the wire on the template (folding collar), unfolding the wire on the end-fitting vault and, finally, the resin cure. Different from SHEN *et al.* (2008) and XAVIER (2009), the interaction between the tensile armor wire and the resin is due to the resin contraction. The anchoring system in this model was substituted by an adhesion at the tip of the wire as illustrated in Figure 24.

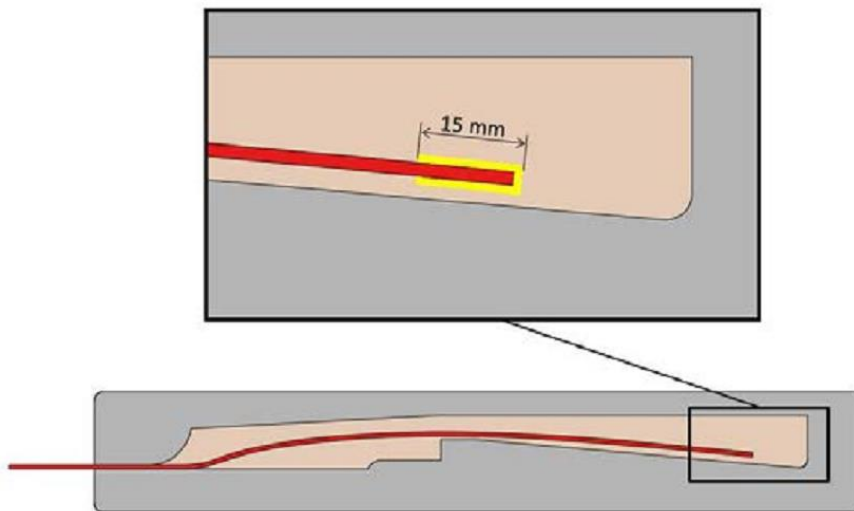


Figure 24. Tip of the tensile armor wire in the 2D FE model presented by CAMPELLO (2014).

The output of the FE model is one SCF for the alternate stress and another SCF for the mean stresses for fatigue calculation. Finally, the analytical and the 2D FE model were faced with experimental full-scale tests. The final results of the analytical and FE models had good agreement with the accumulated fatigue damage results from the experimental full-scale tests.

BENIRSCHKE (2014) proposed an analytical model and a 2D FE model to evaluate the stresses on the tensile armor wires inside the EF. Similar to CAMPELLO (2014), the proposed analytical model calculates the residual radius and residual stress (spring-back effect) in the EF rear region of the tensile armor wire after the folding process. In the parametric study with the analytical model, it was concluded that thinner tensile armor wires have lower residual stresses after the folding process. The same result was observed when materials with lower yield stresses were considered. For the 2D FE model, the commercial software ANSYS® was used. It was modelled with quadratic 2D elements. The main boundary conditions were similar to the one presented by SHEN (2008) and XAVIER (2009) with the tensile armor wire partially bonded to the resin. With this 2D FE model BENIRSCHKE (2014) simulated several collar radius ranging from 30 to 80 mm and one important conclusion of this study is that the folding collars radius of 70 mm and 80 mm did not show much difference on the stress level. At last, the SCF in the most severe condition with a folding collar radius of 30 mm was 1.3.

At this point, it is important to discuss some aspects of the analytical models, which is compared to the 3D FE based model proposed in this dissertation. Next, some remarks on analytical models available in the literature are presented.

3.1 REMARKS ON THE ANALYTICAL MODEL

The analytical model presented by CAMPELLO (2014) is very robust. Here some remarks are made on the collar radius (input of the analytical methodology presented by CAMPELLO (2014)) and on two formulations of stress decay inside the end-fitting.

3.1.1 FOLDING COLLAR RADIUS AND MAXIMUM STRAIN

Normally, the tensile armor wire folding process follows the armoring lay angle. When folding the wire in this condition, the folding collar projection may be used to calculate the maximum strain (see Figure 25, where the angle ' α ' corresponds to the armoring lay angle and the line 'B-B' is the folding collar projection 'section B-B').

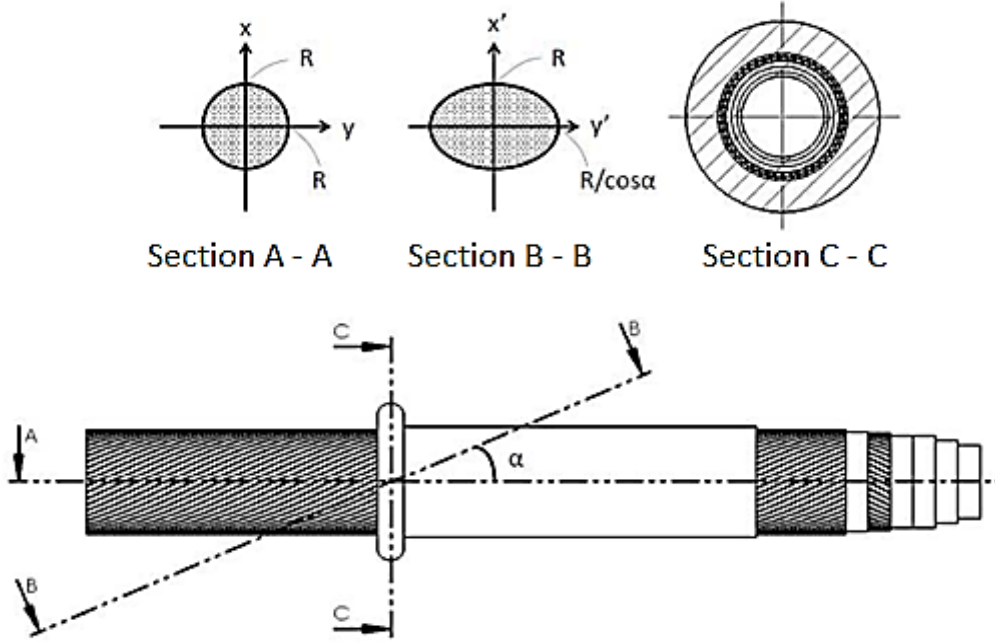


Figure 25. Collar and ellipse radius illustration (CAMPELLO, 2014).

With this approach, the ‘Section B-B’ – projection of the folding collar – corresponds to an ellipse (Equation (3.1)) and the collar projection radius can be calculated with the curvature radius Equation (3.2). The point with the minimum curvature radius (R_e) is the Equation (3.3).

$$v(t) = \begin{bmatrix} a \cdot \cos(t) \\ b \cdot \sin(t) \\ 0 \end{bmatrix} \quad (3.1)$$

$$R_e = \frac{|v(t)|^3}{\left| v(t) \times \frac{dv(t)}{dt} \right|} \quad (3.2)$$

$$R_e = \frac{b^2}{a} = \frac{R_g^2}{\frac{R_g}{\cos(\alpha)}} = R_g \cdot \cos(\alpha) \quad (3.3)$$

where ‘ α ’ is the armoring lay angle; ‘ a ’ is the R (see Figure 25); ‘ b ’ is equal to $R / \cos(\alpha)$ (see Figure 25); R_g is the folding collar radius and R_e is the Ellipse minor radius.

With the minimum radius, the maximum strain (ϵ) in step 1 (fold the tensile armor wire on the collar) can be calculated with Equation (3.4).

$$\varepsilon = -\frac{1}{2\frac{R_e}{t} + 1} \quad (3.4)$$

Where ‘ t ’ is the tensile armor wire thickness.

3.1.2 STRESS DECAY INSIDE THE END-FITTING

This item presents two approaches for the stress decay inside the end-fitting. The first formulation is the simplest capstan equation as presented by BROWN (1999) and the second formulation are the group of equations proposed by CAMPELLO (2014).

3.1.3 FIRST FORMULATION

The capstan equation relates the reaction force to a load when a flexible line is laid around a cylinder form. This formulation is based on the interaction of frictional forces and on the tension applied on a flexible line. This formulation is presented in Equation (3.5) and is independent of the cylinder radius.

The total contact angle ‘ θ ’ is the contact between the flexible line and the cylinder surface illustrated in Figure 26 and is denoted as ‘ $d\theta$ ’. For a tensile armor wire inside the end-fitting, the contact angle can be calculated with Equation (3.6).

$$F_{sd}(z) = F_0 \cdot e^{-\mu \cdot \theta} \quad (3.5)$$

$$\theta(z) = 2\pi \frac{z}{Pitch} \quad (3.6)$$

where F_{sd} is the final force due to stress decay inside the EF; F_0 is the axial force applied on one tensile armor wire in the tube region; μ is the friction coefficient; ‘ θ ’ is the total contact angle; R_g is the folding collar radius; R_e is the ellipse minor radius; z is the total length of wire inside the EF and ‘ $Pitch$ ’ is the armoring pitch.

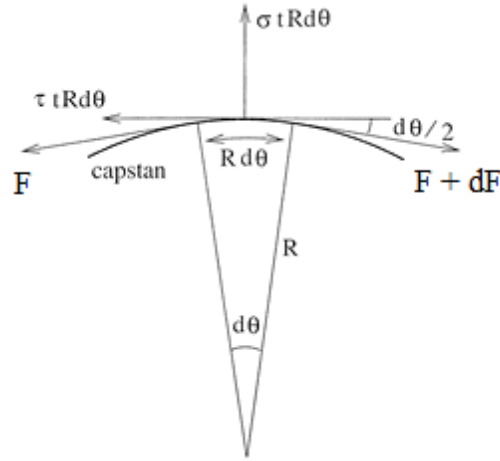


Figure 26. Illustration of a flexible line over a cylinder – modified from (BROWN, 1999).

The friction shear stress around the tensile armor wire due the resin contraction during the cure can be calculated with Equation (3.7) as presented by DAFLON (2010) and CAMPELLO (2014).

$$\tau(z) = \frac{F_0}{p \cdot z} ; \text{ for } z > 0 \quad (3.7)$$

where ‘ τ ’ is the shear stress inside the EF; and ‘ p ’ is the perimeter of the contact between the tensile armor wire and the resin.

By considering the friction shear stress calculated with experimental data, the stress decay in the wire inside the EF due to friction shear stress is presented in Equation (3.8).

$$F_{sd}(z) = \tau \cdot p \frac{z}{\cos(\alpha)} \quad (3.8)$$

And, finally, using Equations (3.5) and (3.8) the stress decay becomes the Equation (3.9).

$$\sigma_{sd1}(z) = \left[\frac{F_0 \cdot e^{-\mu \cdot \theta(z)} - \tau \cdot p \cdot z}{ff \cdot w \cdot t} \right] \cdot \sec(\alpha) \quad (3.9)$$

where ‘ ff ’ is the shape factor of the wire and ‘ w ’ is the tensile armor wire width.

3.1.4 SECOND FORMULATION

This formulation is proposed by CAMPELLO (2014). Equation (3.10) is similar to Equation (3.5). The difference is related to the angle where the flexible line is laid, which is substituted for ‘ η ’ and is dependent of the EF geometry. The parameter ‘ η ’ is presented in Equation (3.11) :

$$F(z) = F_0 \cdot e^{-\mu \cdot \eta(z)} \quad (3.10)$$

$$\eta(z) = \varphi^{-1} \left[\sqrt{1 + tg^2 \alpha \cdot \left(1 + \frac{\varphi}{r_0} z\right)^2} - \sec(\alpha) \right] \quad (3.11)$$

where ‘ φ ’ is the angle between the tensile armor wire internal diameter and the vault maximum external diameter and ‘ r_0 ’ is the tensile armor internal radius.

The stress decay deduction is similar to the first formulation. Equation (3.12) is the complete 2nd formulation. It is compared with the 1st formulation and with the 3D FE based approach results in the next chapters.

$$\sigma_{sdf2}(z) = \left[\frac{F_0 \cdot e^{-\mu \cdot \eta(z)} - 2 \cdot \tau \cdot (w + t) \cdot z}{ff \cdot w \cdot t} \right] \cdot \sec(\alpha) \quad (3.12)$$

CHAPTER 4

3D FINITE ELEMENT BASED APPROACH FOR LOCAL ANALYSIS INSIDE THE EF

4.1 INTRODUCTION

This chapter presents the main characteristics of the finite element approach developed to study the local mechanical response of one tensile armor wire inside the end-fitting of a flexible pipe. This nonlinear three-dimensional approach consists of two FE models. The first one simulates the folding and unfolding process during the EF mounting and the second model simulates the stress relief (after the FAT and/or OLT) and operational loads after EF mounting with the tensile armor wire surrounded by resin. Both models are developed in the commercial software ANSYS® version 14.5. Figure 27 presents an overview of the model. The next item describes the main characteristics of these models.

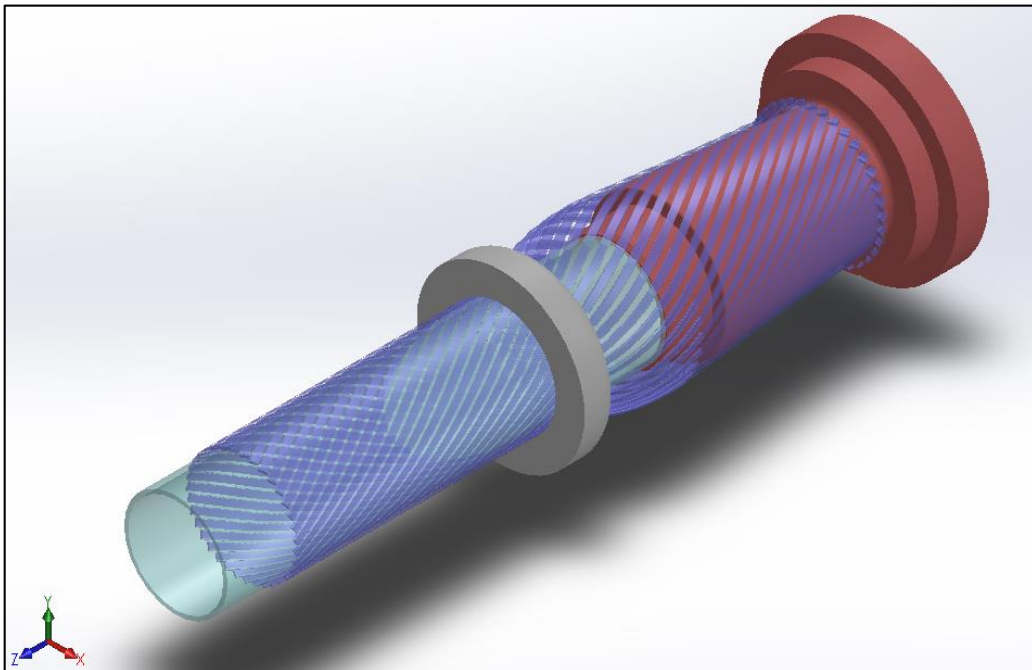


Figure 27. Complete 3D FE model overview.

4.2 SIMULATION OF THE FOLDING/UNFOLDING PROCESS

4.2.1 PREMISES

The end-fitting (EF) of a flexible pipe is a complex structure. In order to represent the EF mounting process and simplify the FE model for the further analysis, the following premises are adopted:

- a) Simplification of the flexible pipe structure:
 - i. Internal tube that corresponds to all layers underneath the second armor layer.
 - ii. Second armor layer is represented by only one wire.
 - iii. No anti-wear and neither high strength tape nor external sheath are modeled.

- b) Simplification of the EF:

Several parts of the EF were merged into one (*e. g.* front flange and vault). Moreover, the vault diameter includes the internal armor layer thickness.

- c) Internal tube, folding collar and vault are modeled as rigid bodies (no deformation and no displacement).

- d) No residual stresses from manufacturing process is considered in this 3D FE based approach.

4.2.2 GEOMETRY

Figure 28 is an overview of this first model which simulates the folding/ unfolding process. It is composed of one tensile armor wire, slice of the internal tube, slice of the folding collar and a slice of the EF's vault.

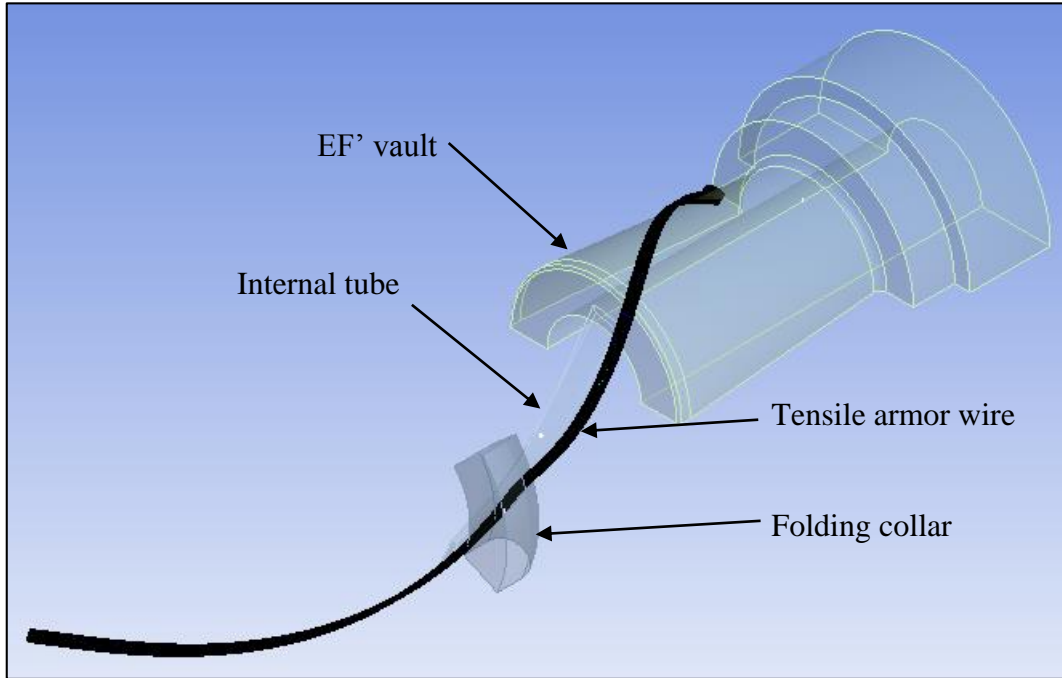


Figure 28. General overview of the FE model parts (step 3 – unfold process).

4.2.3 FE MESH CHARACTERISTICS

The tensile armor wire is modeled with a structured hexahedral using non-linear quadratic elements – SOLID186 (ANSYS, 2014). SOLID186, as shown in Figure 29, is a high order 3D element with 20 nodes. This finite element has quadratic displacement interpolation functions and supports plasticity, hyperelasticity, creep, stress stiffening, large deflections and large strains.

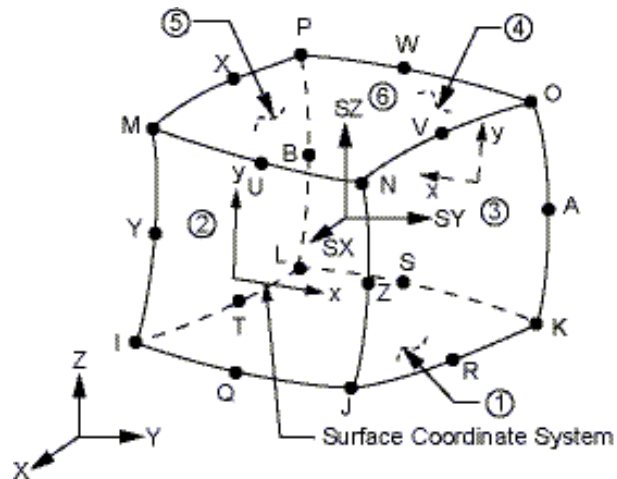


Figure 29. SOLID186 definition (ANSYS, 2014).

The simulation output is an important point for hexahedral mesh with SOLID186 elements. The element stress directions are parallel to the element coordinate system (see Figure 29), which makes the data processing easier with no need to align the global coordinate system to the helical shape of the tensile armor wire in order to assess the local stresses. SOLID186 is capable of considering initial stress states and temperatures.

Figure 30 shows a typical FE mesh used for simulating the folding/unfolding of a tensile armor wire. During the folding process the vault mesh in Figure 30 is deactivated and it is activated when the wire is positioned on the vault during the unfolding process. In Figure 30 (a) is an overview of the FE model mesh, (b) is the structured mesh of the vault and (c) is the tensile armor wire and internal tube slice meshes.

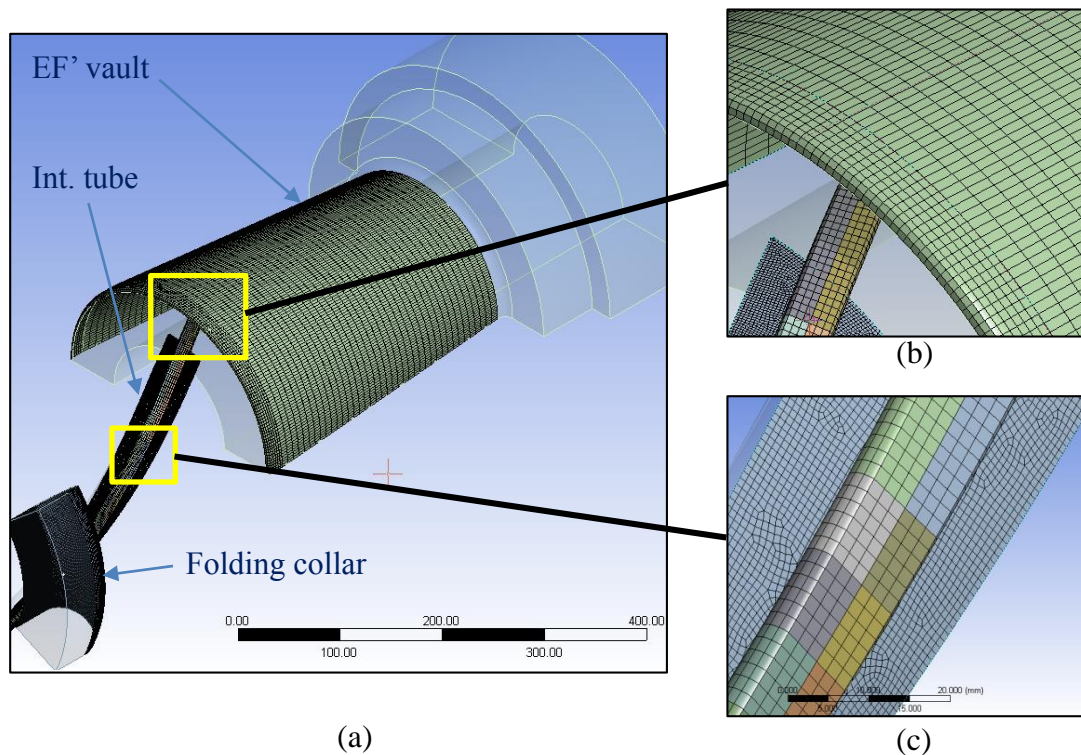


Figure 30. First model (folding/ unfolding) – mesh images.

Another important aspect of the model is the contact between layers. All contacts are modeled with CONTA174/TARGE170 contact and target elements, respectively (ANSYS, 2014). They are surface/surface 3D contact elements defined by 8 nodes. CONTA174 is used to represent contact and sliding between a 3D target surface and a deformable surface (TARGE170). These elements are located on the surface of 3D solid elements with mid-side nodes – *i.e.* SOLID186 and SOLID187 (ANSYS, 2014).

CONTA174 supports isotropic and orthotropic Coulomb friction, shear stress friction and user-defined friction. For isotropic friction, only one friction coefficient is needed. The default element coordinate system is noted by ‘R’ and ‘S’ in Figure 31. For orthotropic friction, two friction coefficients are used as input, the global coordinate system is the default x, y as per Figure 31 (ANSYS, 2014).

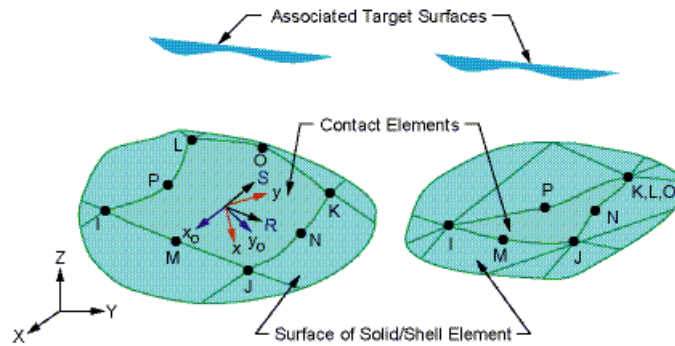


Figure 31. CONTA174 geometry (ANSYS, 2014).

For nonlinear solid body contact of faces, ‘Pure Penalty’ or ‘Augmented Lagrange’ formulations can be used. Both of these are penalty-based contact formulation – where the contact force is the product of a normal contact stiffness and penetration, as per Equation (4.1) and illustrated in Figure 32. The higher is the normal stiffness (k_{Normal}), the lower is the penetration (x_p) (ANSYS, 2014). This parameter has an important influence on the convergence of the model. Higher values of k_{Normal} difficult the model convergence while lower values may help on convergence but may give inconsistent results; in this case the simulation output shall be verified carefully.

$$F_{Normal} = k_{Normal} \cdot x_{Penetration} \quad (4.1)$$

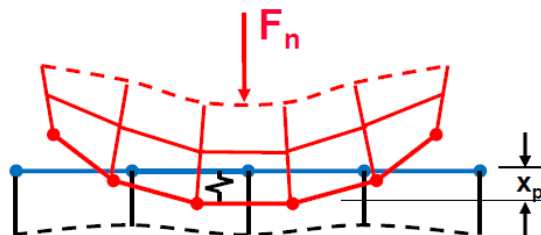


Figure 32. Penetration illustration between contact and target elements (ANSYS, 2014).

Friction between the components can also be considered. ANSYS® provides an exponential friction decay model. This is a reasonable model to allow a smooth transition between the static and dynamic friction along the simulation. For that reason, it is important to define the static (μ_s) and dynamic (μ_d) friction coefficients and the exponential decay coefficient (β) in Equation (4.2) – where ‘v’ is the slip rate at the contact point, which is calculated by the program. In Figure 33, it can be seen that small values of ‘ β ’ leads to a smoother transition from static to dynamic friction coefficient.

$$\mu = \mu_d + (\mu_s - \mu_d) \cdot e^{-\beta v} \quad (4.2)$$

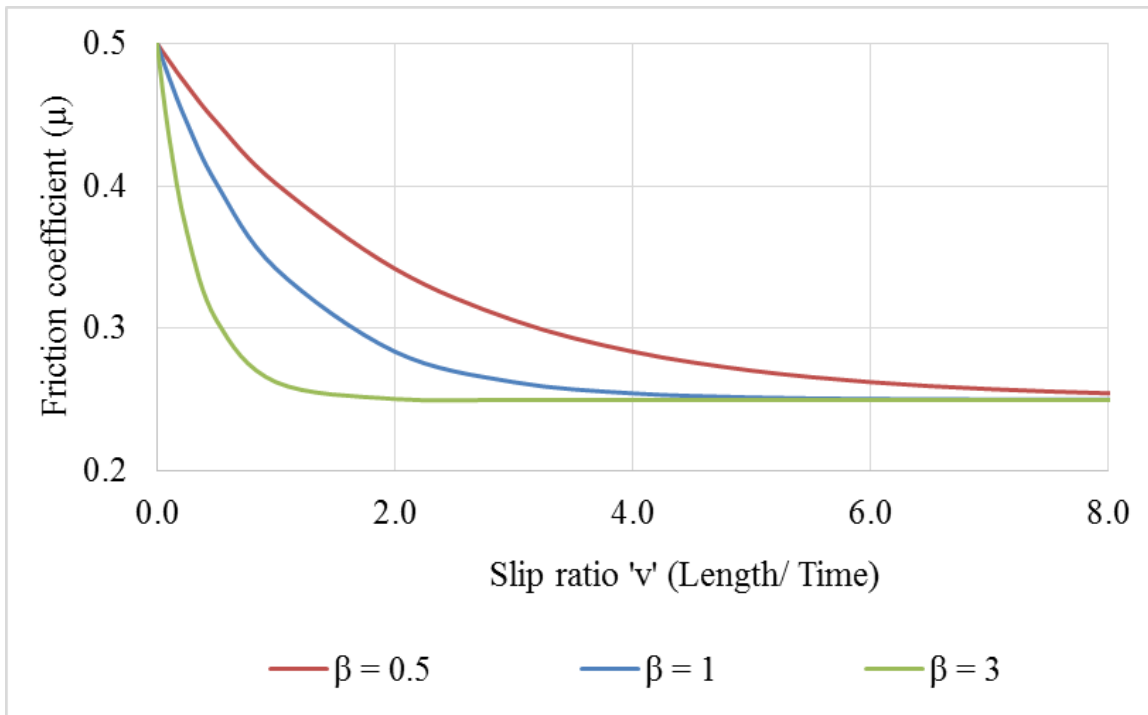


Figure 33. Friction decay illustration.

Finally, Table 2 presents the contact characteristics in the FE model surfaces. In steps 1 to 3, the isotropic friction model with only one friction coefficient is used.

Table 2. Contact among the surfaces of step 1 to 3.

Region	Contact details
Wire x Internal tube contact	Deformable/ deformable Type: surface /surface (CONTA 174 / TARGE170) Frictionless Formulation: Augmented Lagrangean
Wire x Folding collar contact	Deformable/ deformable Type: surface /surface (CONTA 174 / TARGE170) Frictional Formulation: Augmented Lagrangean
Wire x Vault contact	Deformable/ deformable Type: surface /surface (CONTA 174 / TARGE170) Frictional Formulation: Augmented Lagrangean Update stiffness: Each Iteration Time step control: Predict for Impact

For the ‘Wire x Vault’ contact, other features are implemented to facilitate the convergence. A friction coefficient of ‘1.0’ is used in order to avoid much slip of the wire with respect to the vault. Much slip may change abruptly the contact in some regions (contact to no-contact or vice-versa) leading to difficulties on convergence. The normal stiffness is updated at each converged iteration during step 3 in order to avoid too much penetration.

4.2.5 BOUNDARY CONDITIONS

The boundary conditions (BCs) applied on steps 1 to 3 aimed to represent a real EF mounting process. In order to represent the mounting process and simplify the model, some premises were established in item 4.2.1. Following those premises, the BCs for steps 1 to 3 are indicated in Figure 34 and explained hereafter:

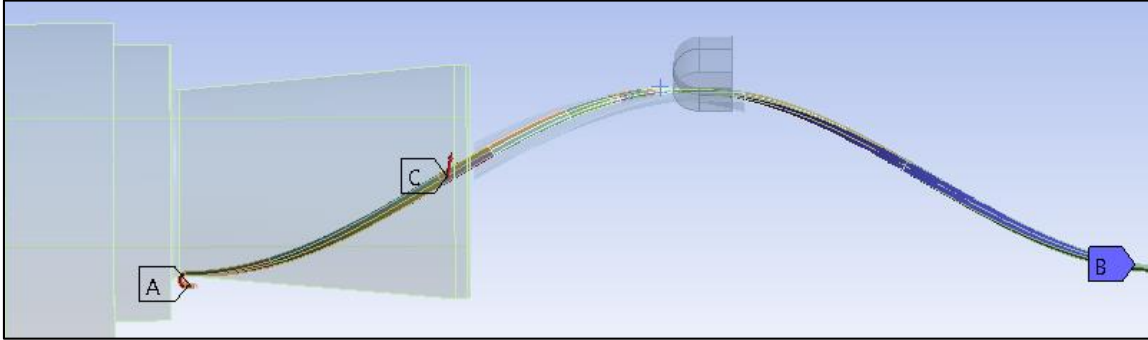


Figure 34. Boundary conditions of the steps 1 to 3 – folding/ unfolding FE model.

- a) BC-A – Force applied in the anchoring region during step 3 (unfold process). Here, the applied force aims to position the wire on the vault with the armoring lay angle.
- b) BC-B – A short length of the wire is fixed (blue region in Figure 34).
- c) BC-C – Force is imposed on the wire at mid-distance between the folding collar and the anchoring system during steps 1 and 3. In step 1, the force has a fixed direction in order to reproduce the manual EF mounting process and, in step 3, the force aims only to lay the wire on the vault.

Internal tube, folding collar and vault are modeled as rigid bodies with no deformation nor displacement.

4.2.7 METHODOLOGY

In order to simulate a real EF mounting process, this first FE model, which simulates the EF folding/unfolding process is divided in three steps.

Table 3 details the three steps and the main outputs of this proposed FE model. All these steps are sequentially described and illustrated hereafter (Figures 35 to 37). Snapshot sequences of steps 1 to 3 can be seen in appendix A.

Table 3. Simulation steps and outputs summary.

Simulation Steps		Outputs
Step 1	Fold the wire around the folding collar	Maximum strain Von Mises stress Local stress
Step 2	Free position of the wire with no loadings	Maximum strain
Step 3	Unfold the wire and lay down on the vault	Maximum strain Von Mises stress Local stress

Step 1 corresponds to the tensile armor wire folding process on the folding collar (see Figure 35). Here, a specific folding angle is imposed on the wire in order to evaluate the maximum strain, which is compared with the analytical model presented in Equation (3.4).

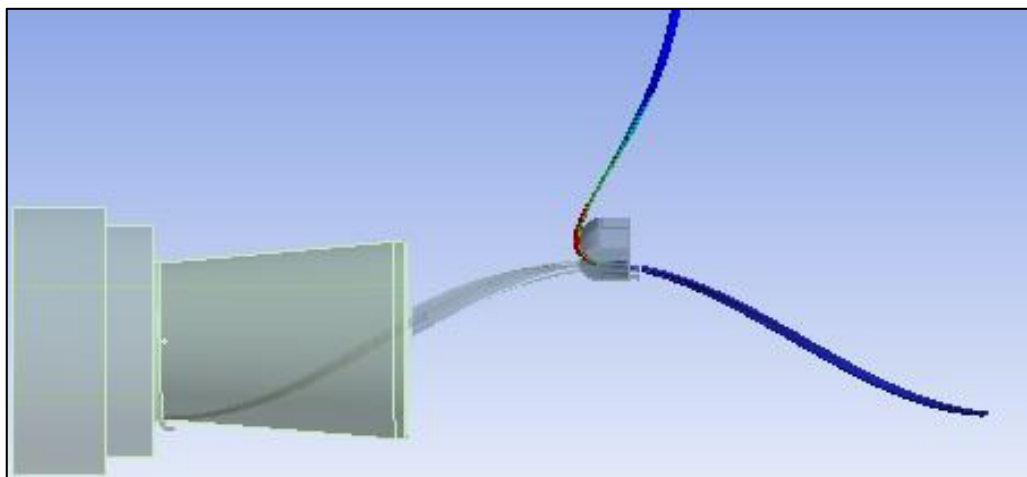


Figure 35. Step 1 illustration – folding process.

Step 2, no load is applied on the tensile armor wire (Figure 36). The wire is released and a small spring back effect is observed – the results of this step are compared with the analytical model presented by CAMPELLO (2014).

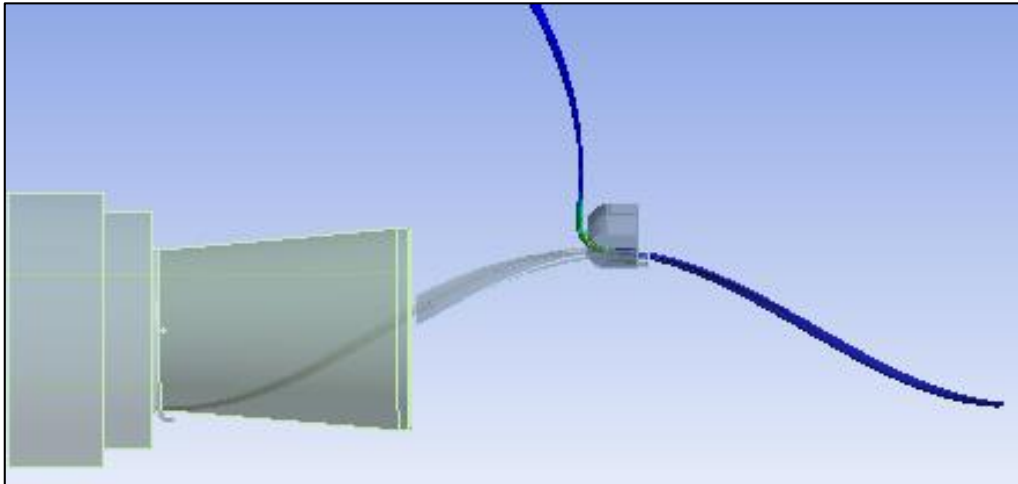


Figure 36. Step 2 illustration – free position.

In step 3, after releasing, the tensile armor wire is unfolded and positioned on the vault (Figure 37). This is the final position of the wire.

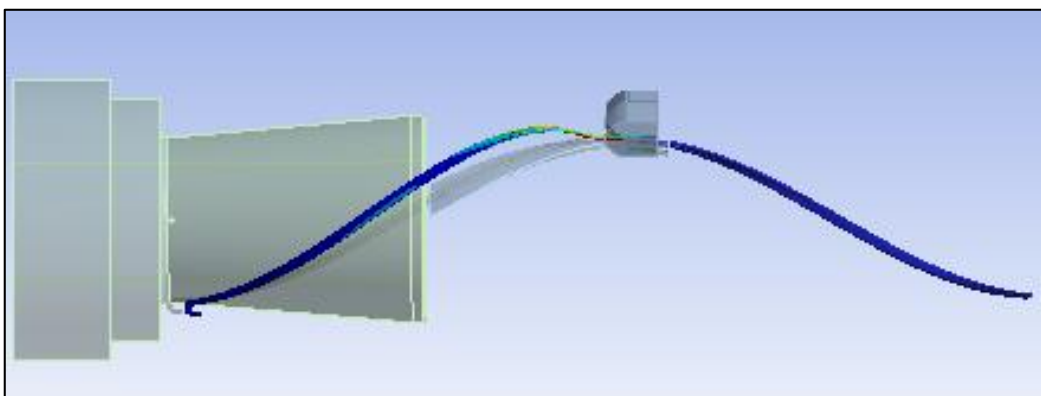


Figure 37. Step 3 illustration – unfolding process.

4.4 SIMULATION OF THE STRESS RELIEF AND THE APPLICATION OF TENSILE LOADS

4.4.1 GEOMETRY

Figure 38 gives an overview of this second model, which simulates the stress relief and tensile loads. It is modeled with one tensile armor wire (black) and with resin (blue) surrounding the wire.

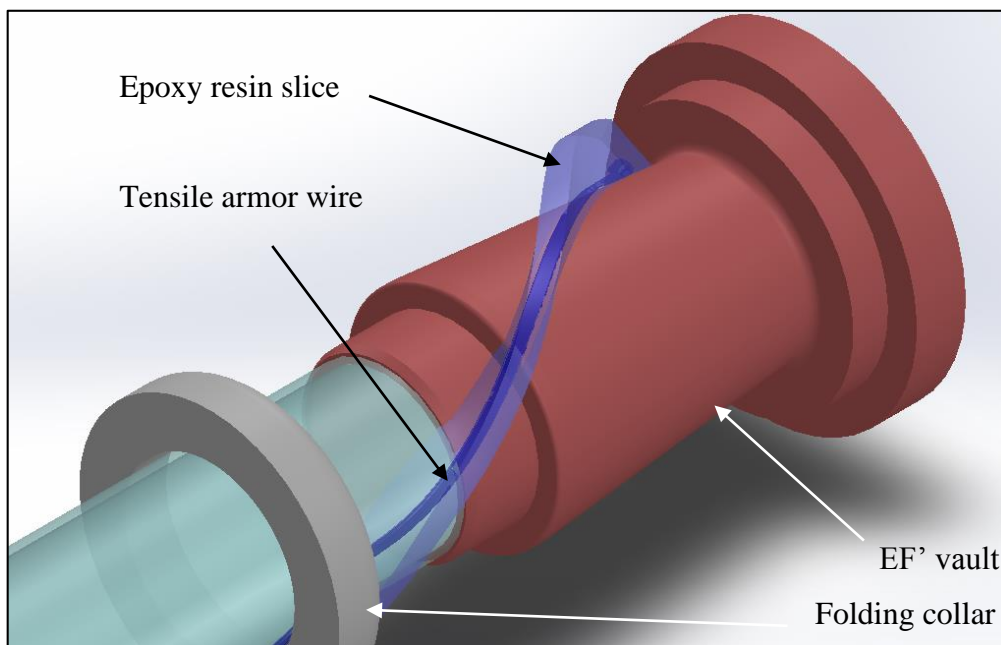


Figure 38. Second 3D FE model with only one tensile armor wire.

4.4.2 FE MESH CHARACTERISTICS

In this second FE model, the wire is represented with the same mesh of the first model. The resin is modeled with elements SOLID186 and SOLID187 (hexahedral and tetrahedral elements). SOLID187, Figure 39, is a high order 3D finite element with 10 nodes. This element has quadratic displacement interpolation functions and support plasticity, hyperelasticity, creep, stress stiffening, large deflections and large strains. SOLID187 is mainly used for irregular meshes (ANSYS, 2014).

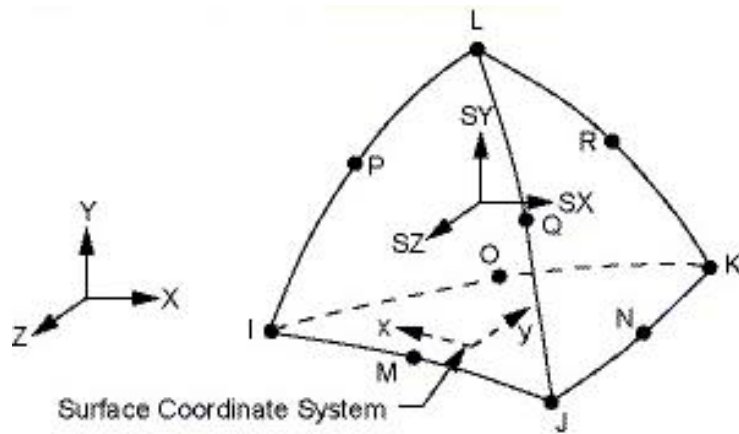


Figure 39. SOLID187 definition (ANSYS, 2014).

SOLID187, analogously to SOLID186, is capable of considering initial stress states and temperatures. This is important for this 3D FE based approach, as the stress state in the wire after the folding/unfolding process is used as an input to this model.

Moreover, the mesh size is based on the mid-scale model presented in the appendix C and a typical FE mesh of this model is presented in Figure 40 – the deformed tensile wire geometry after unfolding can be seen in Figure 28 and Figure 37.

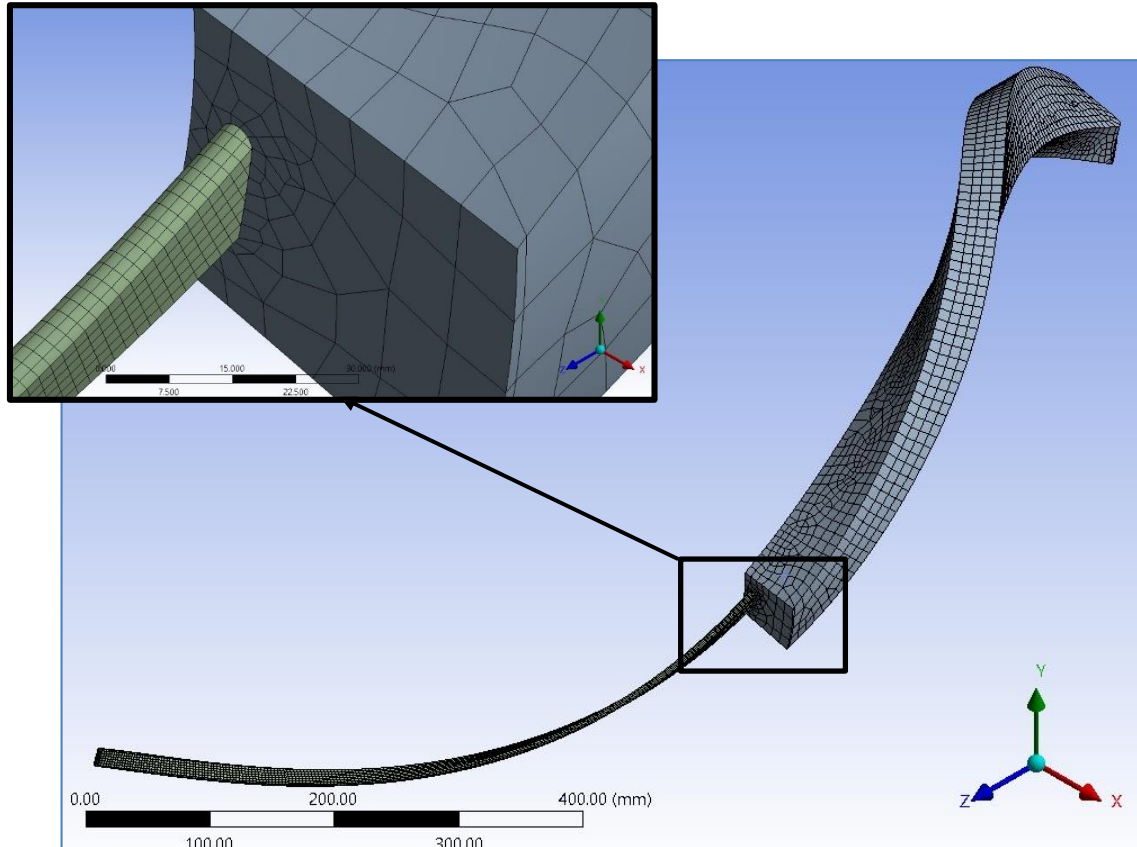


Figure 40. Second model (stress relief and loads) – mesh images.

The interaction between the components is also simulated with CONTA174/TARGE170 finite elements. In this model, the main contact interface is between the wire and the resin. The contact characteristics of this interface are defined after adjusting experimental data with a FE model representative of the experiment. In appendix C, the FE model and the experimental data are compared showing a good agreement.

The results from appendix C (static and dynamic friction coefficients and the friction coefficient decay) are inputs for the contact of the folding/ unfolding FE model. The contact characteristics between wire and resin are presented in Table 4.

Table 4. Contact between wire and resin - step 4.

Region	Contact details
Wire x Resin	Deformable/ deformable Type: surface /surface (CONTA 174 / TARGE170) Frictional Formulation: Augmented Lagrange

4.4.3 BOUNDARY CONDITIONS

In order to represent these tensile loads, some simplifications are considered in this FE model as the contact between the wire and resin, which does not consider adhesion, only friction, and possible contact pressure due to resin contraction during the resin cure. No contact is modeled between the tensile armor wire and the tube.

The BCs of step 4 are indicated in Figure 41 and explained hereafter:

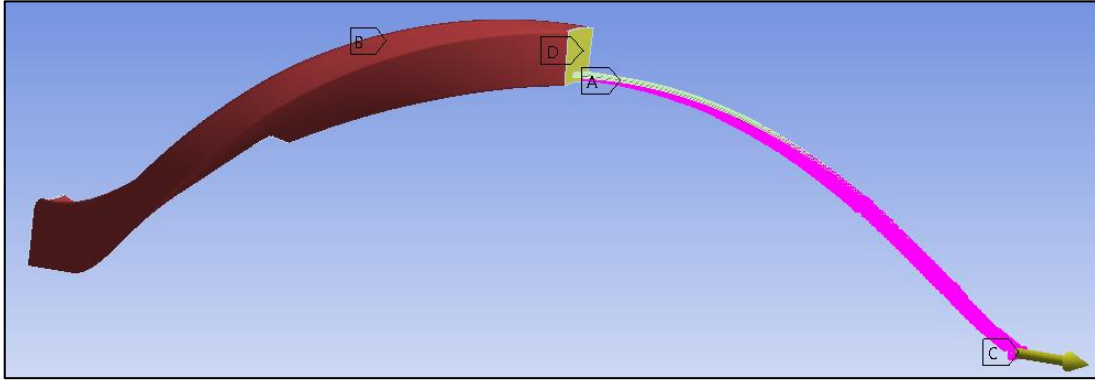


Figure 41. Boundary conditions of step 4 – folding/ unfolding model.

- a) There is no internal tube, neither folding collar nor vault.
- b) BC-A – There is no radial displacement of the tensile armor wire at the tube region (pink region in Figure 41). A discussion on the validity of this premise is presented in appendix B.
- c) BC-B – Resin external surfaces are fixed (red region in Figure 41).
- d) BC-C – Displacement in Z axis is applied at a pilot node linked to wire's surface (yellow arrow in Figure 41).
- e) BC-D – Resin face (yellow region in Figure 41) is free to move in the X and Y directions, but not in the axial direction (Z-axis).

4.4.4 METHODOLOGY

In this second model the stress state from the first simulation is used as an input. Moreover the tensile armor wire deformed shape is also an input in this model, which is also used to define the resin geometry. The deformed geometry is an output from the simulation in Ansys®. The X, Y and Z points of the deformed geometry is used in SolidWorks® to subtract the deformed wire volume from the resin slice.

After the EF mounting process, the flexible pipe is submitted to different loads such as those imposed during the factory acceptance tests (FAT) and offshore leak tests (OLT) and operational loads.

This second FE model is divided in two parts, the first one is the stress relief and the second one is the axial loads applied on the tensile armor wire.

The output data from the first FE model (folding/ unfolding) is used as input for this second model, *e. g.* the deformed tensile armor wire shape and the stress state along the wire.

Table 5 details the outputs of step 4.

Table 5. Simulation steps and outputs summary.

Simulation Step		Outputs
Step 4	Stress relief / tension the wire inside the resin	Maximum strain Von Mises stress Local stress Stress decay inside the EF Stress concentration factor (SCF)

This step 4 corresponds to the stress relief of the tensile armor wire surrounded by the epoxy resin. The aim of this step is to evaluate the residual stress after stress relief, stress ratio (SR) and stress concentration factor (SCF) (Figure 42).

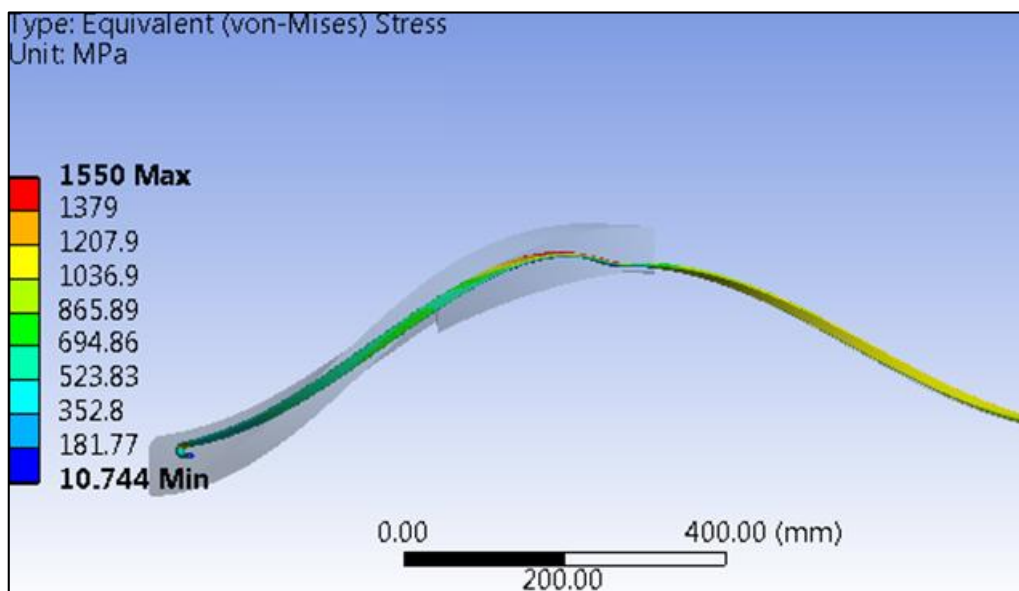


Figure 42. Step 4 illustration – stress relief.

4.5 FEATURES TO AID THE FE MODEL CONVERGENCE

Two features available in ANSYS® were used to aid in convergence – time step control and stiffness update.

Time step control is an automatic time stepping feature that predicts when the status of the contact will change abruptly and cuts the current time step back. It reviews the contact after each substep to determine whether excessive penetration or drastic changes in contact status have occurred. If there is penetration or changes in contact, the substep increment is bisected (divided by half). Moreover, the time step control predicts the minimal time increment needed to detect changes in the contact status along the model (ANSYS, 2014).

Update stiffness is a feature that allows the program to modify the stiffness based on the physics of the model by taking into account the element stresses and penetration. This feature allows better convergence with minimal penetration. In the FE models proposed in this dissertation, the stiffness was updated after each converged time step.

Finally, the time step control aids to converge the model by bisecting the time step; it is set active in order to better recognize the contact between the wire and vault during step 3 only.

CHAPTER 5

CASE STUDY

5.1 MATERIALS

The 3D FE based approach proposed in this dissertation considers the material properties presented in (CAMPELLO, 2014). The tensile armor wire is modeled as a non-linear isotropic material, while the epoxy resin is modeled as an elastic and isotropic material.

The tensile armor wire and the resin main characteristics are presented in Table 6.

Table 6. Carbon steel and epoxy resin characteristics (CAMPELLO, 2014).

Material	Young Modulus (MPa)	Yield stress (MPa)	Ultimate tensile stress (MPa)	Poisson coefficient
Carbon steel	200000	1332	1550	0.30
Epoxy resin	8991	-	-	0.33

The ‘stress vs strain’ curve of the carbon steel is presented in Figure 43 and assumes a linear behavior until the yield stress (YS = 1331.5 MPa).

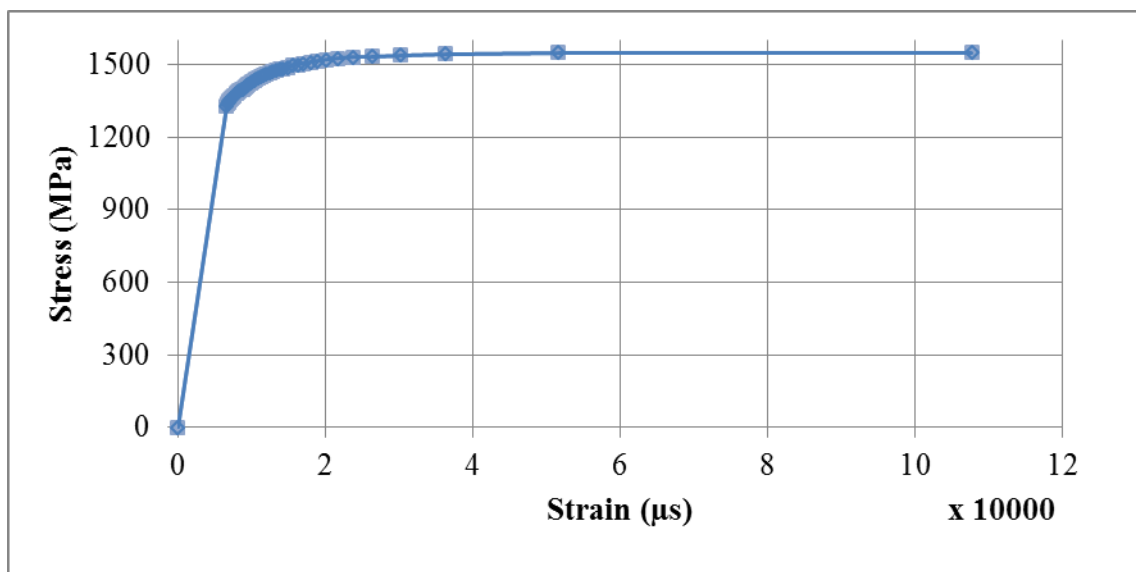


Figure 43. Carbon steel stress vs strain curve – modified from (CAMPELLO, 2014).

5.2 GEOMETRIES

5.2.1 END-FITTING (EF) AND MODEL ASSEMBLY

In order to simplify the model, the front flange and vault of the EF are merged. The EF dimensions are presented in Figure 44. The vault is modeled as a rigid body, in other words, only the external surface has a structured mesh with contact elements.

In Figure 44, the folding collar is located above the tensile armor wire and 672 mm from the vault.

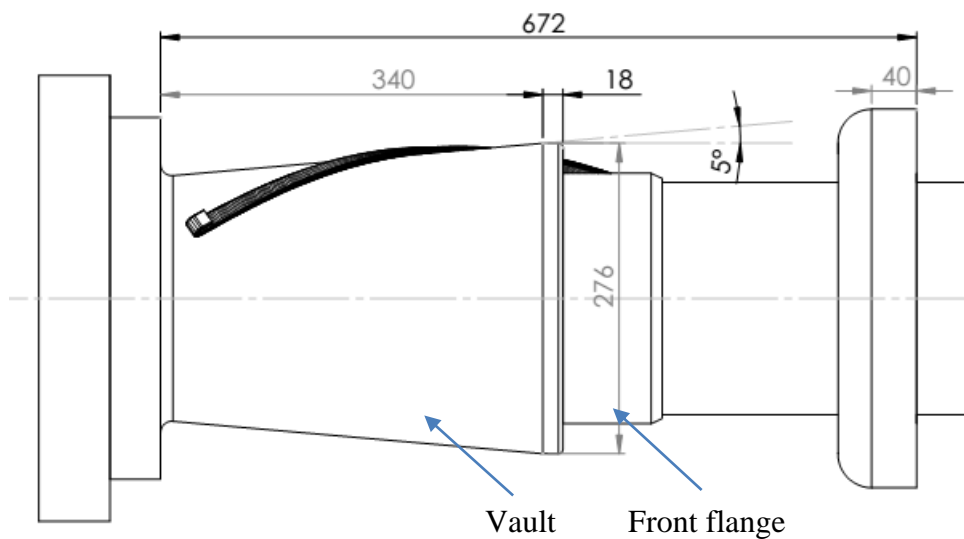


Figure 44. EF dimensions and model assembly (dimensions in mm).

5.2.2 INTERNAL TUBE AND TENSILE ARMOR WIRE

The internal tube is modeled as a rigid body with an external diameter of 209.6 mm. It accounts for all layers of the flexible pipe underneath the second tensile armor layer.

The armor wire cross-section is, approximately, rectangular and its main dimensions are presented in Figure 45. Armor wire's lay angle and mean diameter (parameters needed to generate the helical shape of the wire) are 30.1° and 212.1 mm, respectively.

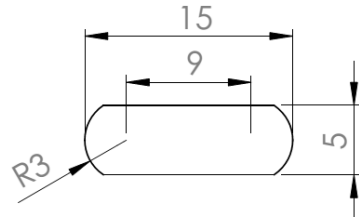


Figure 45. Armor wire dimensions (15x5) mm – simplified from (CAMPELLO, 2014).

5.2.3 RESIN

Figure 46 (a) is an illustration of the resin inside the EF and (b) the resin slice used in the simulations. The resin geometry depends on the tensile armor wire deformed shape after the EF mounting. In the analyses presented in this dissertation, the deformed mesh was treated using ‘FE Modeler’ (ANSYS® tool) and SolidWorks® in order to build the resin geometry. The region inside the resin had one slice subtracted from the deformed wire shape in order to model the contact between the wire and the resin as presented in Figure 46 (b).

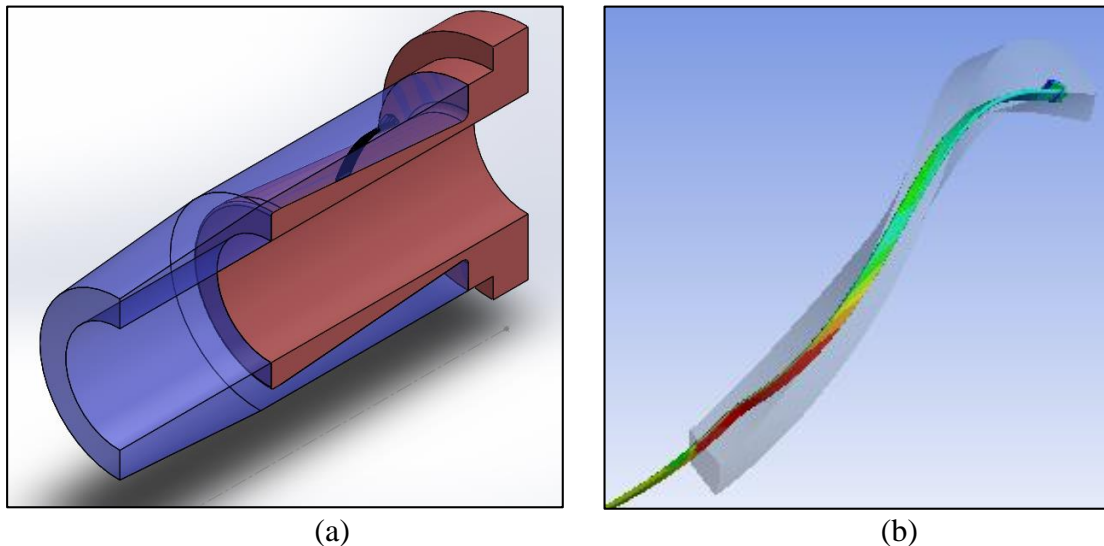


Figure 46. (a) Illustration of the resin inside the EF: vault (red) and resin (blue); (b) Resin slice used in the simulation (shaded).

5.2.5 FOLDING COLLAR

The folding collar is a rigid body and has a simple geometry. Only one slice of the folding collar is used in the simulations, *i. e.*, the location where there is contact between the wire and the collar. Its dimensions are presented in Figure 47, where: ‘R’ is equal to 60 mm.

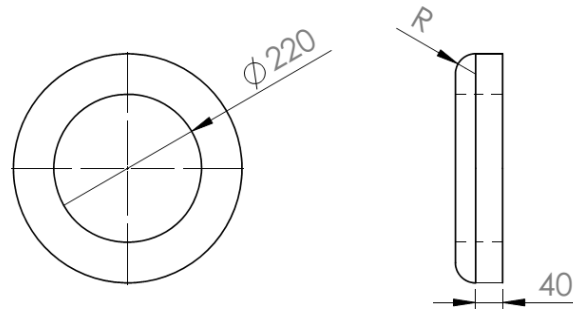


Figure 47. Folding collar dimensions (mm).

5.3 INTERACTION BETWEEN COMPONENTS

For the first model (steps 1 to 3), the friction coefficients between the pair tensile armor wire and folding collar is $\mu = 0.3$ and between wire and vault is $\mu = 1.0$ with a normal stiffness factor of 0.1 in order to facilitate the convergence of the model. For the second model (step 4) the frictional coefficient between the pair tensile armor wire and resin is $\mu_s = 0.50$ (static friction coefficient) and $\mu_d = 0.25$ (dynamic friction coefficient) with an exponential decay coefficient is $\beta = 0.8$ (these values are from the FE model presented in appendix C).

5.5 LOAD CASES

5.5.1 FOLDING/UNFOLDING SIMULATION

The load cases studied with this FE model in steps 1 to 3 are presented in Table 7. The load case R60A30 (in bold) is the base case. The folding angle (α') in Table 7 goes from the armoring lay angle $\alpha = 30^\circ$ (see Figure 25 for details) to the folding angle of 10° .

Table 7. Load cases for the first model – steps 1 to 3.

Collar Radius (Rg) (mm)	Folding angle (α') (degree)
30	10
	30
60	10
	20
	30
90	10
	30

5.5.2 STRESS RELIEF AND OPERATIONAL LOADS

In this second model, which simulates the stress relief and tensile loads, firstly the resin is heated. The initial temperature is 60°C and, then, the temperature is decreased to 20°C in order to represent the resin contraction during the resin cure.

The base case for this second model is the folding collar with 60 mm and folding angle of 30° (R60A30) where the stress decay, stress relief, residual stress and stress concentration factor (SCF) are studied. For the residual stress the models 'R30A30' and 'R90A30' are also analyzed.

5.7 FE MESH

The mesh has an important role in any FE model. The mesh size and type of elements have a significant impact on the processing time and on the outputs (results). For that reason, before launching a FE model, it is important to perform a mesh test to have a good compromise of processing time and accurate solution.

Table 8 presents the mesh parameters for the mesh test for this first model (R is the folding collar radius and A is the folding angle in step 1).

Table 8. Mesh characteristics – input for the mesh test.

Simulation	N° of nodes	N° of elements	Element face size (mm ²) (1)	Element face size (mm ²) (2)	Element type
R30A30_1	18133	2784	3x4	3x4	SOLID 186
R30A30_2	41645	7392	3x3	3x3	SOLID 186
R30A30_3	59229	11088	2x3	2x3	SOLID 186
R30A30_4	73565	13776	1.5x2	2x3	SOLID 186

(1) Folding region (approximated size)

(2) Region far from the folding region (approximated size)

The number of nodes and elements corresponds only to the tensile armor wire mesh, which has only hexahedral elements.

For the second model the tensile armor wire mesh size is still the same. In order to evaluate the best mesh size for this model, the same FE model employed in CAMPELLO (2014) was made. All results of this model are compared to the experimental data presented by CAMPELLO (2014), the results can be found in appendix C. The resin mesh size was based on this mid-scale model presented in the appendix C. The final resin mesh has approximately 45,000 elements and 130,000 nodes.

5.9 CONVENTIONS

Along this work, global and local conventions are used. Figure 48 presents an armor wire laid on a tube, where the global axis is defined as X, Y and Z and Z is the axial of the tube. The axis origin (0; 0; 0) is located at the vault of the EF. The local axis is defined as x, y and z where z is the axial axis of the tensile armor wire (see section 'A-A' in Figure 48).

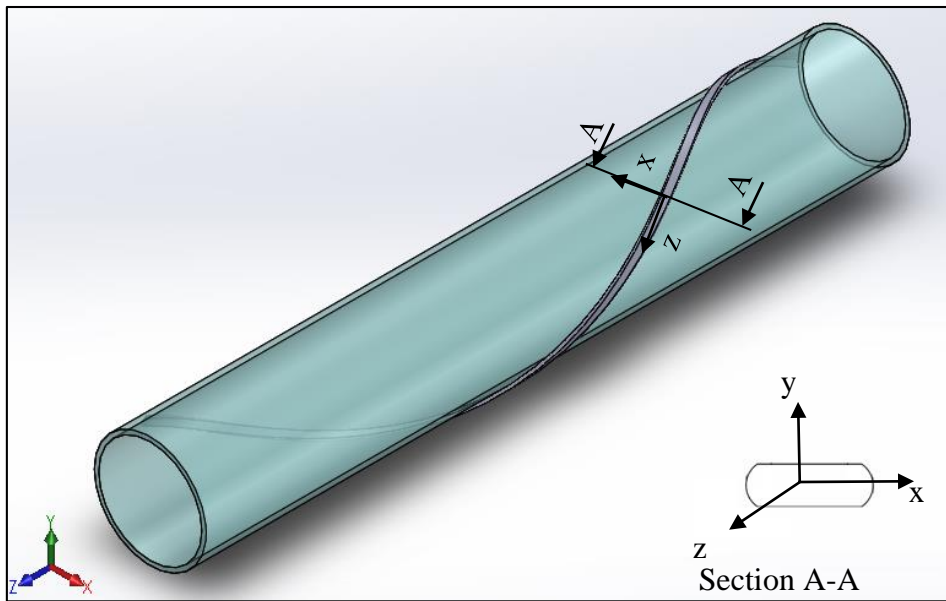


Figure 48. Global and local conventions.

The nomenclatures in Figure 49 and Figure 50 are used for further references about mesh test and local stress results.

Figure 49 presents the regions of the tensile armor wire section which are studied in this work.

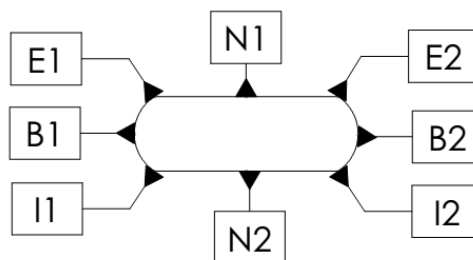


Figure 49. Reference points at the armor wire.

In Figure 50, the collar base is the region where the wire starts to be folded during step 1 (folding process, see chapter 4) and the folding collar highest curvature point (CHCP) is the region where the maximum strain occurs in step 1 in the tensile armor wire.

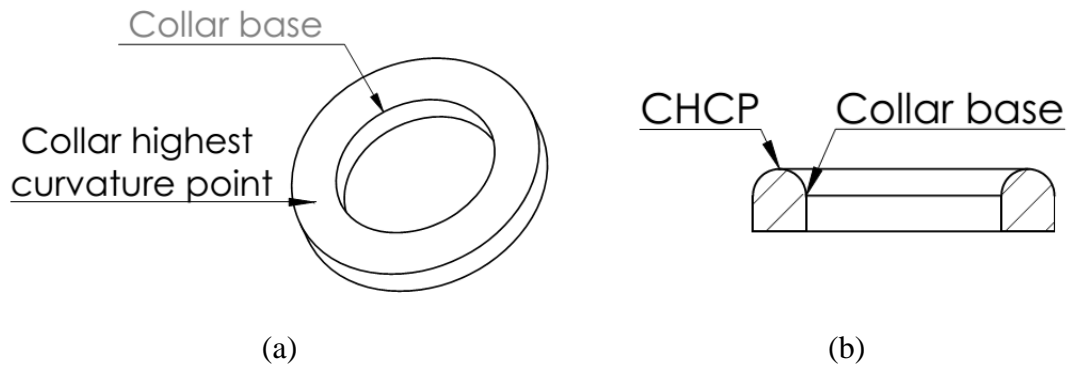


Figure 50. Reference points in the folding collar. (a) Isometric view and (b) section view.

5.10 RESULTS AND DISCUSSION

5.10.1 COLLAR RADIUS (R_g) X ELLIPSE RADIUS (R_e)

The Equation (3.4) gives the strain based on geometric parameters of the tensile armor wire considering a specific collar radius (R_g). As presented by VARDARO *apud* CAMPELLO (2014), the wire shape is representative of an ellipse during the folding process, as explained in item 3.1.1.

As can be observed in Table 9, when the folding angle α' decreases (approximate to zero with respect to the tube axis – see α in Figure 25), the maximum strain level of the wire in step 1 approximates to the collar radius (R_g) strain level. The simulation results presented along this work corroborates this approach. Moreover, for the analytical model proposed by CAMPELLO (2014) the 'R_g' is replaced by 'R_e' as input for the residual radius and for further calculations.

Table 9. Total plastic deformation – collar radius x ellipse minimum radius.

Collar Radius (Rg) (mm)	Folding angle (α) (degree)	Folding collar radius (mm)		Strain ratio (ϵ/ϵ_y)	
		Re	Rg	Re	Rg
30	10	29.5	30.0	11.7	11.6
	20	28.2		12.2	
	30	26.0		13.2	
60	10	59.1	60.0	6.1	6.0
	20	56.4		6.4	
	30	52.0		6.9	
90	10	88.6	90.0	4.1	4.1
	20	84.6		4.3	
	30	77.9		4.7	

Where ‘ ϵ ’ is represented by Equation (3.4) and ‘ ϵ_y ’ is the strain at yield – equal to 0.00666 [mm/ mm].

5.10.2 MESH TEST

In the mesh test, the total equivalent strain is analyzed. Step 1 is selected for the mesh test. The exact location in the mesh test was the point N1 at the tensile armor wire (extrados). The extrados sees the highest compression level in step 1.

Figure 51 presents the mesh test results. All results are very similar, except for the maximum total equivalent strain of the model G3R30A30_1, which has lower number of nodes.

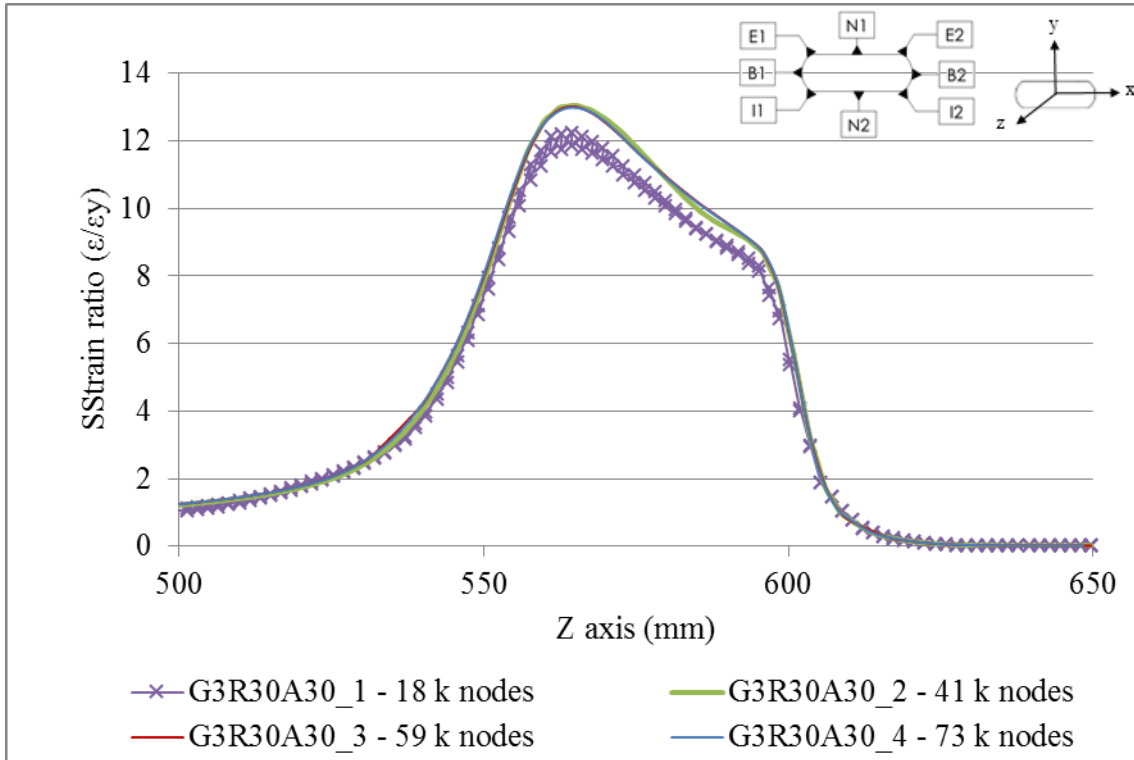


Figure 51. Mesh test results (point N1).

Figure 52 shows that the model with more than 41,000 nodes has results similar to those obtained with more refined meshes such as the mesh with 78,000 nodes.

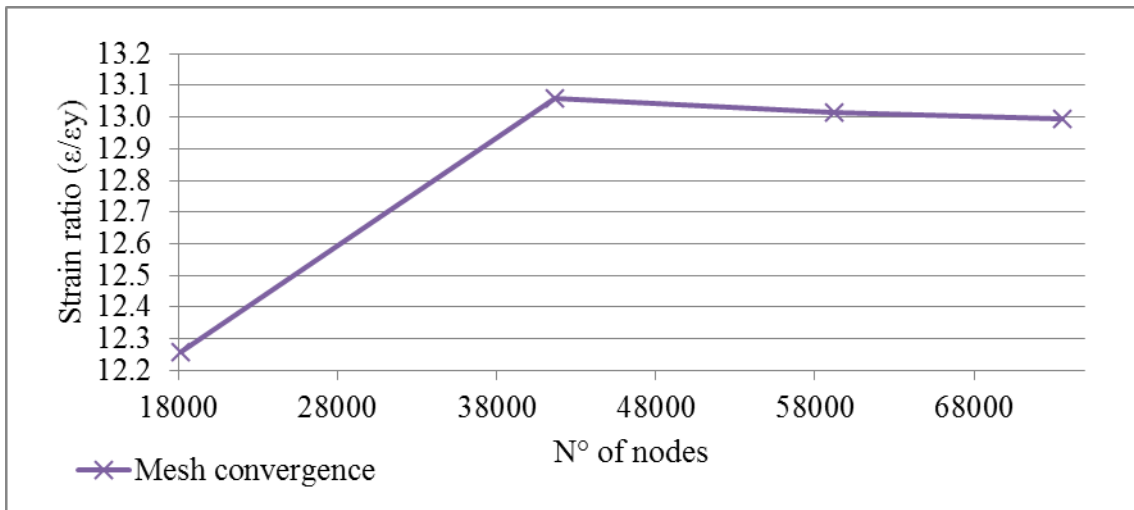


Figure 52. Strain ratio computed with different FE meshes.

Table 10 presents the maximum total equivalent strain and the relative deviation with respect to the analytical approach of simulations ‘G3R30A30_1’ to ‘G3R30A30_4’.

The last three simulations have a relative deviation of approximately 1% with respect to the analytical model.

Table 10. Mesh test results – total strain (point N1).

Simulation	N° of nodes	N° of elements	FE strain ratio (ϵ/ϵ_y) (1)	Analytical strain ratio (ϵ/ϵ_y) (2)	Relative deviation [1-(1)/(2)]
G3R30A30_1	18133	2784	12.26	13.18	7.0%
G3R30A30_2	41645	7392	13.06		0.9%
G3R30A30_3	59229	11088	13.01		1.3%
G3R30A30_4	73565	13776	12.99		1.4%

All these results indicate that a mesh with at least 41,000 nodes has a good compromise between processing time and robust results. The results obtained with this mesh are therefore representative of the folding/ unfolding process.

5.10.3 STEP 1 TO 3 (FOLD, FREE AND UNFOLD STEPS)

The total processing time of this first model (steps 1 to 3) is approximately 1 - 2 days, running on two cores of an Intel® quad core processor (3.6 GHz) and the minimum RAM required to run this model is 10 Gb.

Hereafter, the results from steps 1 to 3 (at point N1 in the tensile armor wire, see reference points in Figure 49) are compared with the analytical model presented by CAMPELLO (2014). The strain and stress levels presented are located in the folding region and also along the tensile armor wire. In addition, some points regarding the local stress along the tensile armor wire are presented and discussed.

5.10.3.2 STEP 1 - MAXIMUM STRAIN

Firstly, the highlighted image in Figure 53 is a general view of step 1.

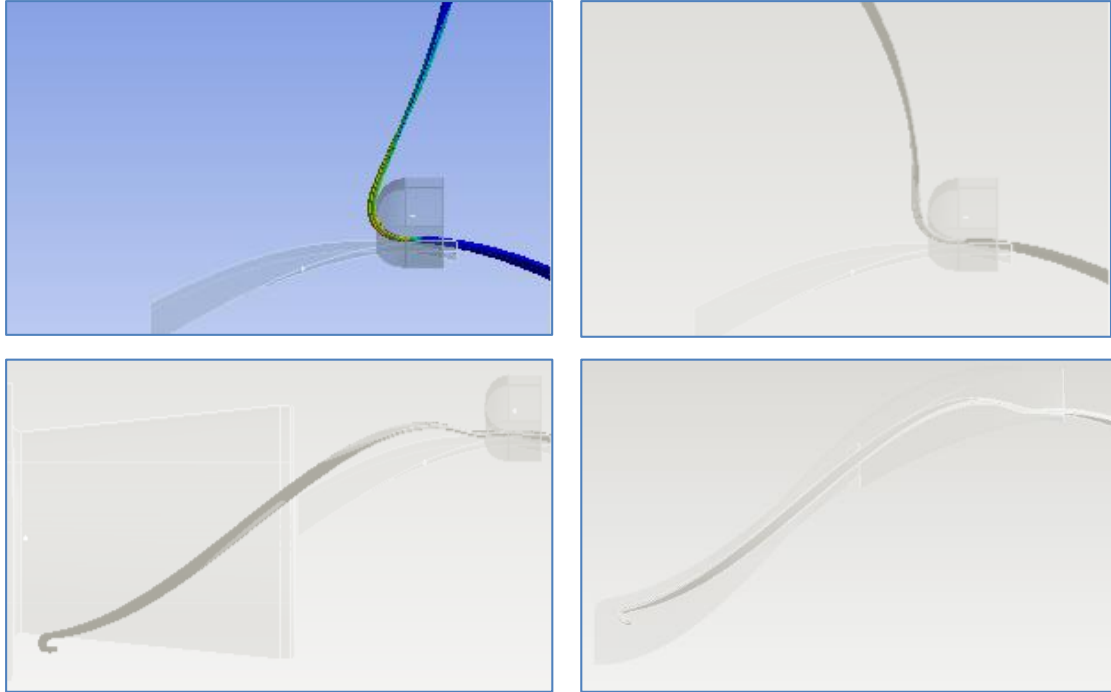


Figure 53. General overview of the simulation steps - Step 1.

In this step, the maximum strain is calculated using the ellipse radius. As can be depicted from Table 11, the results of this step are very similar to the analytical model with a maximum relative deviation of -8% for simulation ‘R90A10’. The results of the FE model corroborate the approach discussed in item 5.10.1, *i. e.*: ‘when the folding angle α ’ decreases (approximate to zero in relation to the tube axis – see ‘ α ’ in Figure 25) the maximum strain level of the wire at step 1 approximates to the collar radius (R_g) strain level’.

Table 11. Strain results of step 1 – point N1.

Simulation	Step 1 - Fold		
	FE strain ratio (ϵ/ϵ_y) (1)	Analytical strain ratio (ϵ/ϵ_y) (2)	Relative deviation [1-(1)/(2)]
R30A10	12.0	11.7	-2%
R30A30	13.3	13.2	-1%
R60A10	6.4	6.1	-5%
R60A20	6.6	6.4	-3%
R60A30	6.8	6.9	2%
R90A10	4.4	4.1	-8%
R90A30	4.7	4.7	-1%

In Figure 54, the folding collar radius and the folding angle results from Table 11 are plotted in order to better visualize the influence of each parameter (folding angle and folding radius) of step 1. One can observe that the folding collar radius has more influence on the maximum strain than the folding angle. In addition, it can be remarked that collar radii higher than 80 mm do not affect much the total maximum strain. But according to Equation (3.4) – page 29 – the thickness is one parameter for the strain calculation and then for others wire sizes the best collar size may be different from 80 mm.

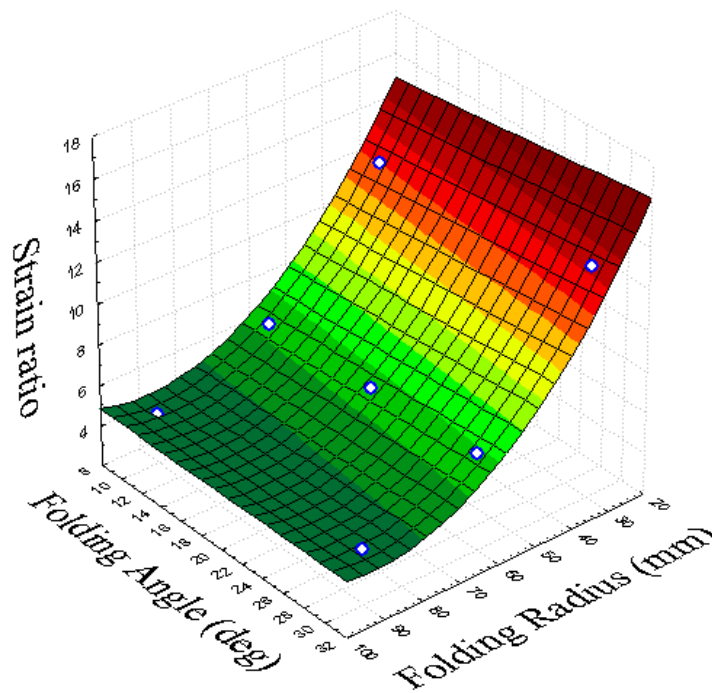


Figure 54. Collar folding radius and folding angle results – Step 1 (maximum strain).

5.10.3.3 STEP 2 – RESIDUAL RADIUS AND RESIDUAL STRESS

The highlighted image in Figure 53 is a general view of step 2.

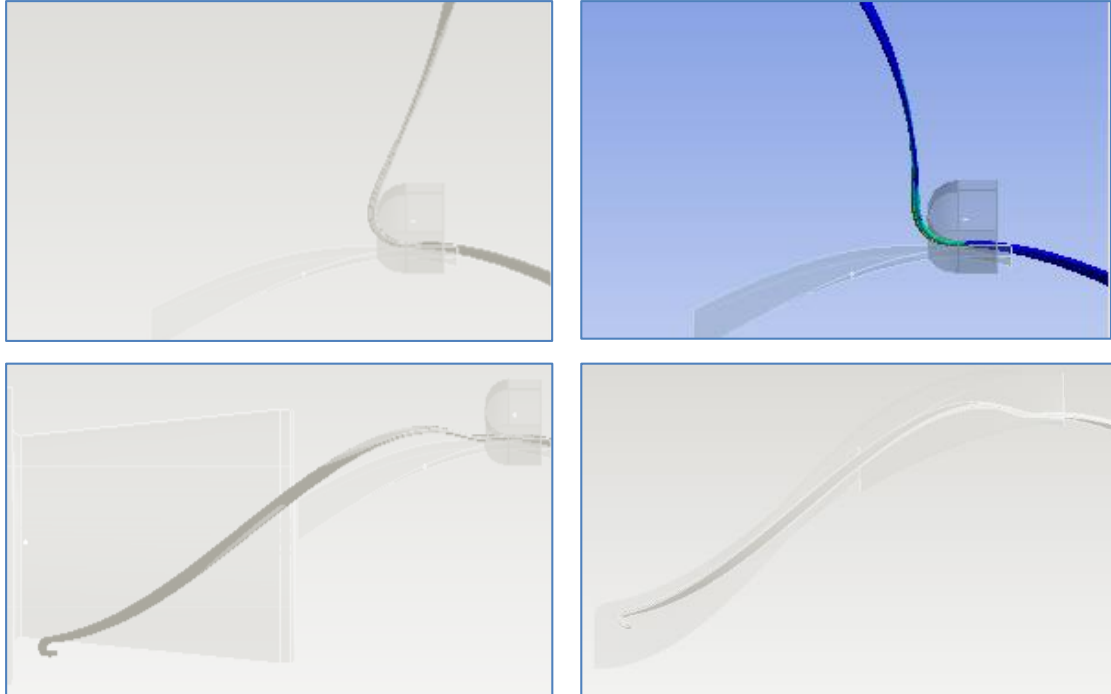


Figure 55. General overview of the simulation steps - Step 2.

In step 2, the nodes with the maximum strain in step 1 have their residual stress and the residual radius (R_r) results presented in Table 12, which also includes the values predicted by the analytical model. As can be observed in Table 12, the FE model and the analytical ' R_r ' results have good agreement, with a maximum relative deviation of 7% for simulation 'R60A30' and 'R90A10'.

In Table 12, the residual stress of the FE and analytical models are similar for folding radii higher than 60 mm, but for load cases 'R30A30' and 'R30A10' the relative deviation bears 30%. This difference could be due to the material law considered in the FE model, which differs from the one considered in the analytical model (perfectly plastic model). Therefore, in order to verify this argument, a FE analysis considering a perfectly plastic material (bilinear model) and the R30A30 condition was carried out and the relative deviation dropped from 30% to 13%.

Table 12. Residual radius and stress results of step 2 – point N1.

Simulation	Step 2 - Free					
	FE Residual radius (mm) (1)	Analytical Residual radius (mm) (2)	Relative deviation [1-(1)/(2)]	FE Residual stress SR (3)	Analytical Residual stress SR (4)	Relative deviation [1-(3)/(4)]
R30A10	31	33	6%	0.61	0.50	-24%
R30A30	29	29	2%	0.65/ 0.56	0.50	-30%/ -13%
R60A10	77	77	0%	0.51	0.49	-4%
R60A20	74	73	-2%	0.52	0.49	-6%
R60A30	61	66	7%	0.52	0.49	-6%
R90A10	127	136	7%	0.43	0.47	8%
R90A30	116	112	-3%	0.44	0.48	8%

(2) Residual radius equation from CAMPELLO (2014): $R_R = \left(4 \frac{\varepsilon_y^3 \cdot R_e^2}{3} - 3 \frac{\varepsilon_y}{t} + \frac{1}{R_g}\right)$.

(4) Residual stress equation from CAMPELLO (2014): $\sigma_{res} = (1 - UF_{Relax})E \left[\frac{t}{2R_e} - \frac{t}{2R_R} - (\varepsilon_y) \right]$

For the residual stress, the tendency of the FE and the analytical models are similar. When increasing the collar radius, the residual stress decreases, whereas increasing the folding angle, the residual stress increases as can be seen in Figure 56.

While the maximum strain in step 1 has an exponential decay when increasing the folding radius (Figure 54), the residual radius and stress in step 2 present an almost linear behavior, as can be seen in Figure 56 and in Figure 57.

Other important point is that there is no much influence of the folding angle on the residual radius and on the residual stress in step 2 as per Figure 56 and Figure 57.

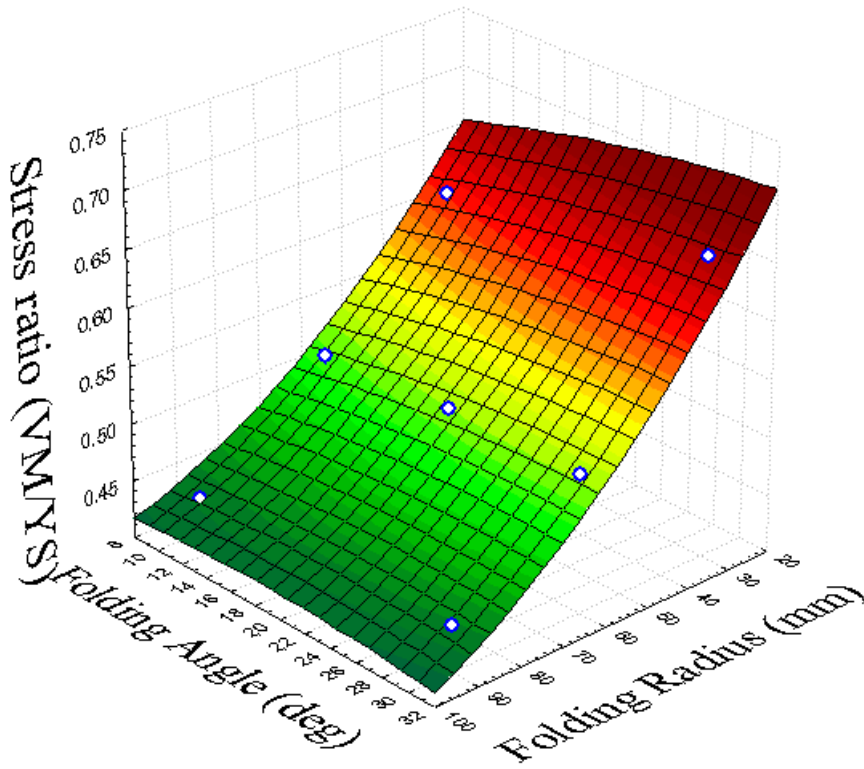


Figure 56. Collar folding radius and folding angle results – Step 2 (residual stress).

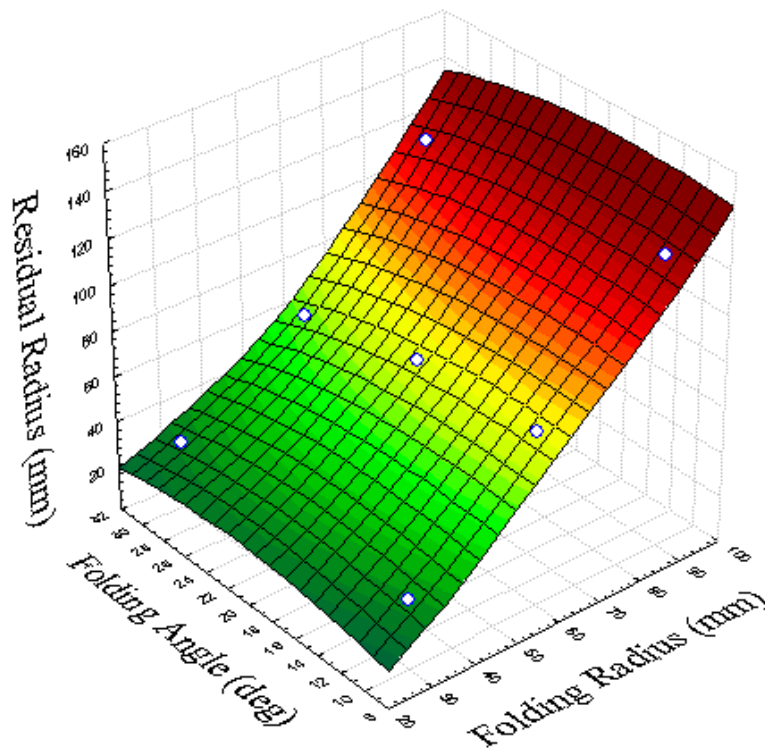


Figure 57. Collar folding radius and folding angle results – Step 2 (residual radius).

5.10.3.4 STEP 3 – RESIDUAL STRESS AND RESIDUAL RADIUS

The highlighted image in Figure 53 is a general view of step 3.

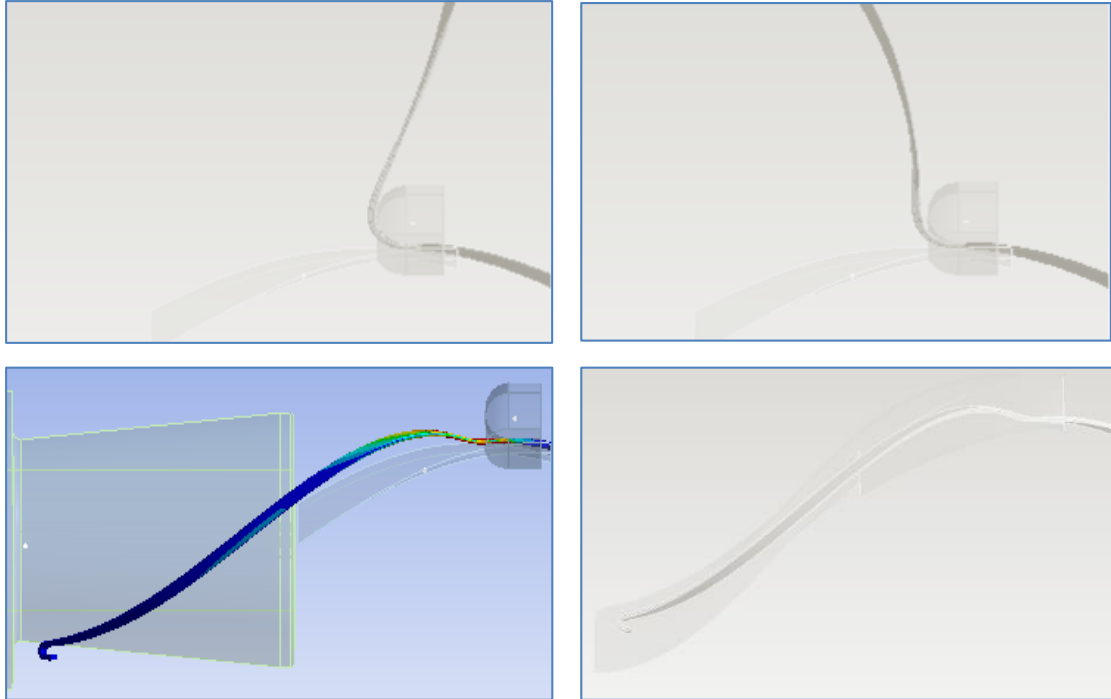


Figure 58. General overview of the simulation steps - Step 3.

Analogously to step 2, the nodes with the maximum strain in step 1 have their residual stress and residual radius measured in step 3. The final VM bears the UTS of the material, as can be seen in Table 13 and, moreover, the residual radii in this step are higher than the residual radii of step 2 (Table 11).

The slightly differences of radius (R_e) when increasing the folding angle in step 1 are not relevant for the final residual radius in step 3. On the other hand, it is relevant for the maximum strain reached in the folding process as presented in item 5.10.1, Table 9 where the ratio of maximum strain between a folding angle of 0° and 30° is 13%.

Table 13. Residual stress results for step 3 – point N1.

Simulation	Step 3 - Unfold	
	FEM VM Stress (MPa)	FEM Residual radius (mm)
R30A10	1550	78
R30A30	1550	69
R60A10	1550	124
R60A20	1550	108
R60A30	1550	113
R90A10	1539	199
R90A30	1540	200

Similar to step 2 (Figure 56), the residual radius in step 3 (Figure 59) has an almost linear behavior when increasing the folding radius and also an approximately constant response when increasing the folding angle.

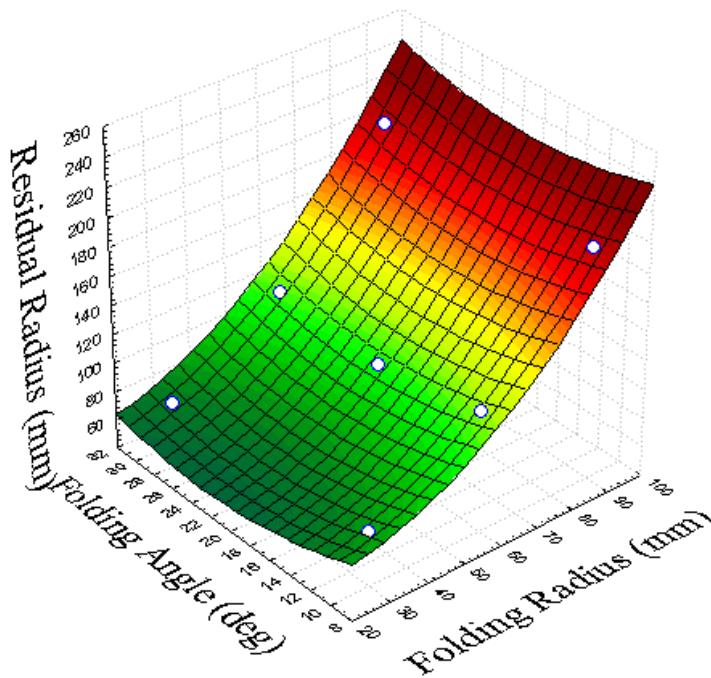


Figure 59. Collar folding radius and folding angle results – Step 3 (residual radius).

5.10.3.6 LOCAL STRESS ALONG THE TENSILE ARMOR WIRE

In this topic, only the case 'R60A30' is studied (steps 1 and 3). The aim here is to evaluate if the EF mounting process could be modeled with a simplified 2D FE model.

Figure 60 presents the stresses along the armor wire at point N1 during steps 1 and 3 (fold and unfold process). Figure 61 shows two pictures of the stress field in the tensile armor wire, where dark blue means zero von Mises stress and red means 1550 MPa.

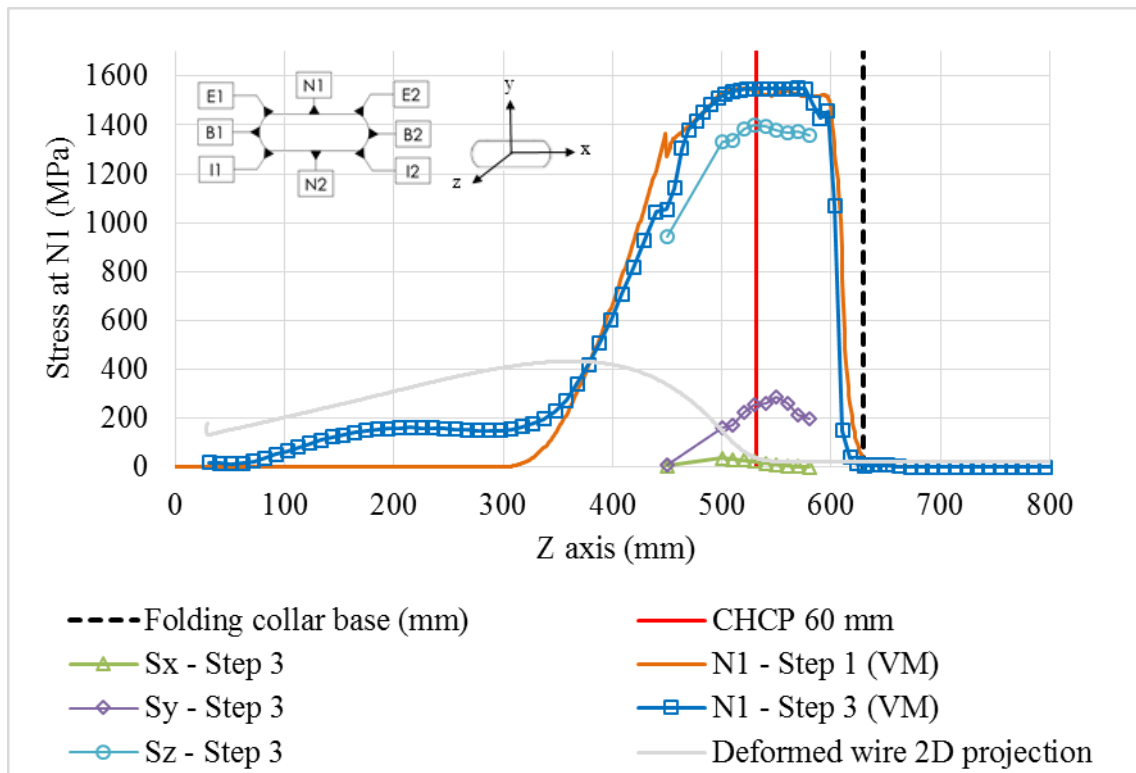


Figure 60. Von Mises stress along the wire's extrados (fold and unfold positions) – simulation R60A30.

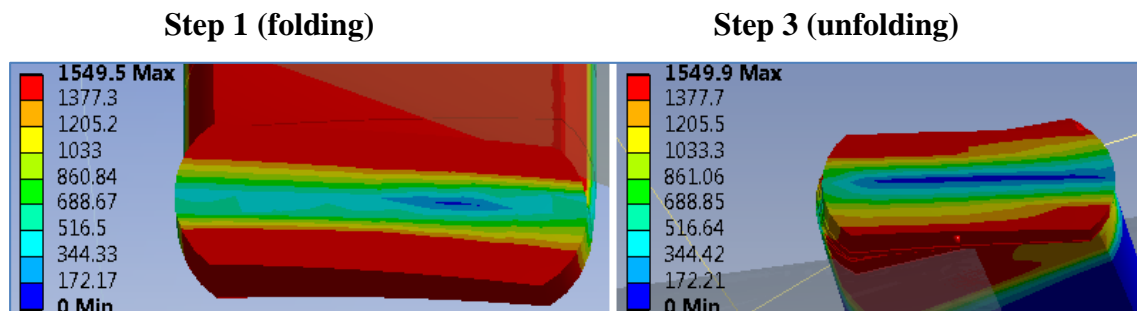


Figure 61. Folding/ unfolding process VM stress.

The higher von Mises stresses in Figure 60 starts at the collar base (where the wire starts to be folded, see Figure 50) and goes until the collar highest curvature point (CHCP, see Figure 50). Figure 60 also presents the local stresses in step 3 (S_x , S_y , S_z). The value of S_z is predominant followed by the S_y whereas S_x is nearly zero. This result already indicates that this folding/ unfolding process could be approximated as a 2D phenomenon as FE models presented by SHEN et al. (2008), XAVIER (2010), SOUSA et al., (2013), CAMPELLO (2014) and BENIRSCHKE (2014).

Figure 62 shows the local stress ‘ S_z ’ along the wire in steps 1 and 3 (folding and unfolding process). The points N1 and N2 have opposite values in the both steps. In step 1 ‘N1’ sees compressive stress and in step 3 tensile stress, the opposite occurs with N2. More details about the local stresses are presented hereafter in Table 14 and Table 15.

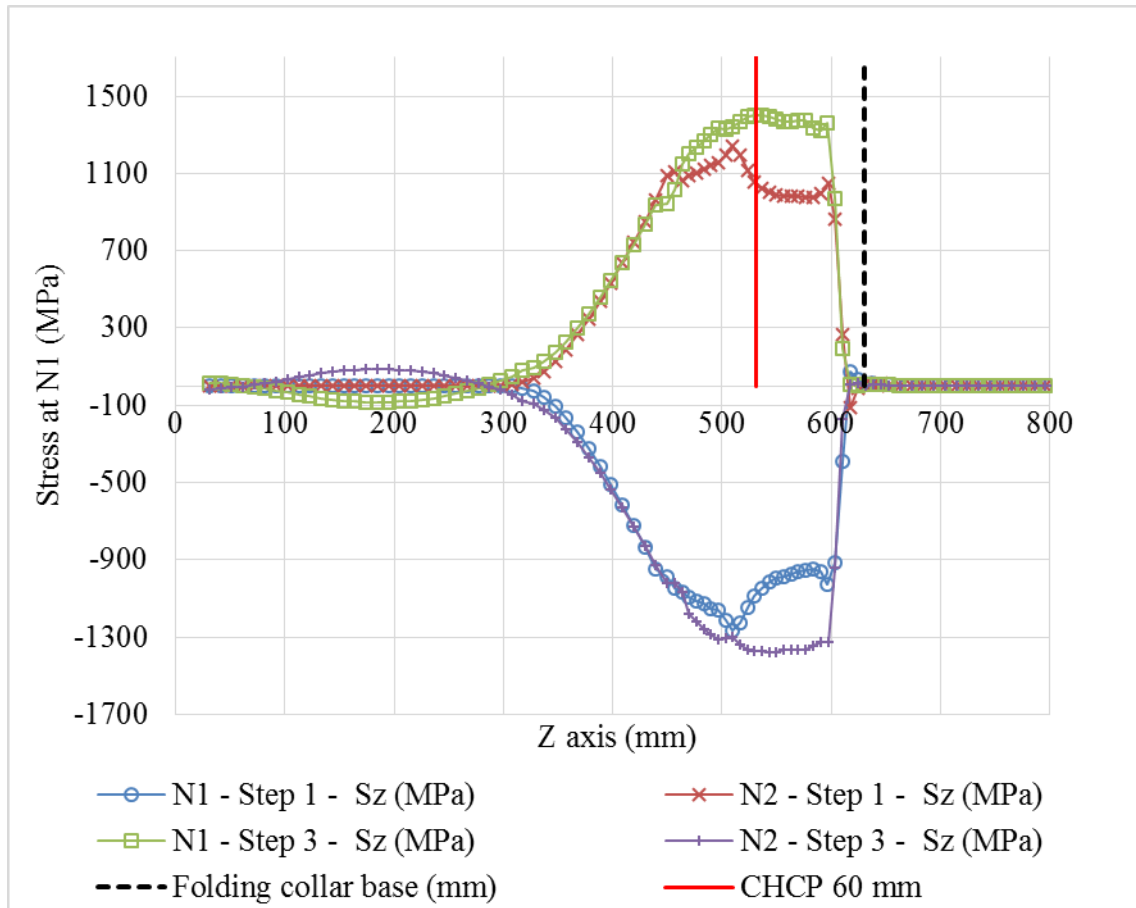


Figure 62. Local stress along the wire’s extrados (fold and unfold positions) – simulation R60A30.

The regions located near the CHCP (Figure 60) are the most stressed in the folding and unfolding process of steps 1 and 3. For this reason, the local stresses in this region

are compared with the von Mises stress (VM) in Table 14 and Table 15 – where the percentage is the ratio between the local stress and VM. As can be seen in both tables, at the points N1 and N2, the axial stress (Sz) has the major influence on VM followed by Sy whereas Sx is nearly zero – same result is presented in Figure 60.

Table 14. Local stresses at the element nodes in step 1 – simulation R60A30.

Step 1 - Fold (MPa)													
Point	VM	Sx		Sy		Sz		Sxy		Syz		Sxz	
N1	1540	-50	3%	-446	29%	-1085	70%	135	9%	676	44%	-207	13%
N2	1544	28	2%	443	29%	1057	68%	-123	8%	-689	45%	192	12%
E1	1533	-28	2%	-547	36%	-956	62%	108	7%	731	48%	-144	9%
E2	1546	-44	3%	-263	17%	-1273	82%	95	6%	563	36%	-202	13%
I1	1533	45	3%	488	32%	963	63%	-156	10%	-703	46%	231	15%
I2	1550	52	3%	250	16%	1247	81%	-116	7%	-557	36%	258	17%
B1	450	-12	3%	-125	28%	-237	53%	-56	12%	201	45%	108	24%
B2	570	18	3%	81	14%	393	69%	-98	17%	-193	34%	147	26%

Table 15. Local stresses at the element nodes in step 3 – simulation R60A30.

Step 3- Unfold (MPa)													
Point	VM	Sx		Sy		Sz		Sxy		Syz		Sxz	
N1	1549	22	1%	255	16%	1400	90%	-70	5%	-483	31%	136	9%
N2	1549	-18	1%	-221	14%	-1375	89%	68	4%	489	32%	-144	9%
E1	1547	22	1%	227	15%	1345	87%	-65	4%	-506	33%	175	11%
E2	1540	65	4%	337	22%	1247	81%	-145	9%	-585	38%	210	14%
I1	1543	-11	1%	-234	15%	-1325	86%	41	3%	541	35%	-70	5%
I2	1548	-51	3%	-293	19%	-1261	82%	118	8%	552	36%	-263	17%
B1	620	100	16%	-103	17%	88	14%	-154	25%	66	11%	295	48%
B2	200	-31	16%	-23	11%	-118	59%	44	22%	58	29%	-73	36%

In Table 14, the stresses at points B1 and B2 are not zero meaning that the neutral axis position has changed during step 1. This phenomenon is explained by DIETIER (1998): for bending below the elastic limit the strain passes through zero halfway – in the neutral axis. While beyond the elastic limit (plastic), the neutral axis moves to the

compressive region (extrados of the tensile armor wire) and, therefore, a point at the mid-thickness of the tensile armor wire is stretched – resulting in a positive stress.

The difference of stress levels between B1 and B2 in step 2 may be explained by the load applied in the model that aimed to represent a real EF mounting process and may lead to a short bending in the folding region (CHCP).

In Table 14 and Table 15, for the base case (R60A30) the shear stress in the plane ‘Sxy’ is negligible whereas the plane ‘Syz’ is the most predominant, except for point B1 in Table 15, where the shear stress in Sxy and Sxz are more significant. The shear stress in planes ‘Sxy’ and ‘Sxz’ are negligible when compared to the stress level in ‘Sz’ and ‘Syz, again, except for point B1 in Table 15. Those results indicates that the folding/unfolding process could be approximately modeled as a 2D phenomenon. The results of all others simulations have same behavior of this studied simulation (R60A30).

5.10.4 STEP 4 (TENSILE LOAD)

The total processing time of this second model (step 4) is approximately 1 - 2 days, running on two cores of an Intel® quad core processor (3.6 GHz) and the minimum RAM required to run this model is 10 Gb. Including all steps to run the both complete models (time processing of steps 1 to 3; resin geometry and mesh generation; and step 4 model generation and time processing) the total time spent is 4 – 5 days for both models.

In this item, the main results of step 4 are presented and compared with the analytical formulations. This step corresponds to the highlighted one in Figure 63.

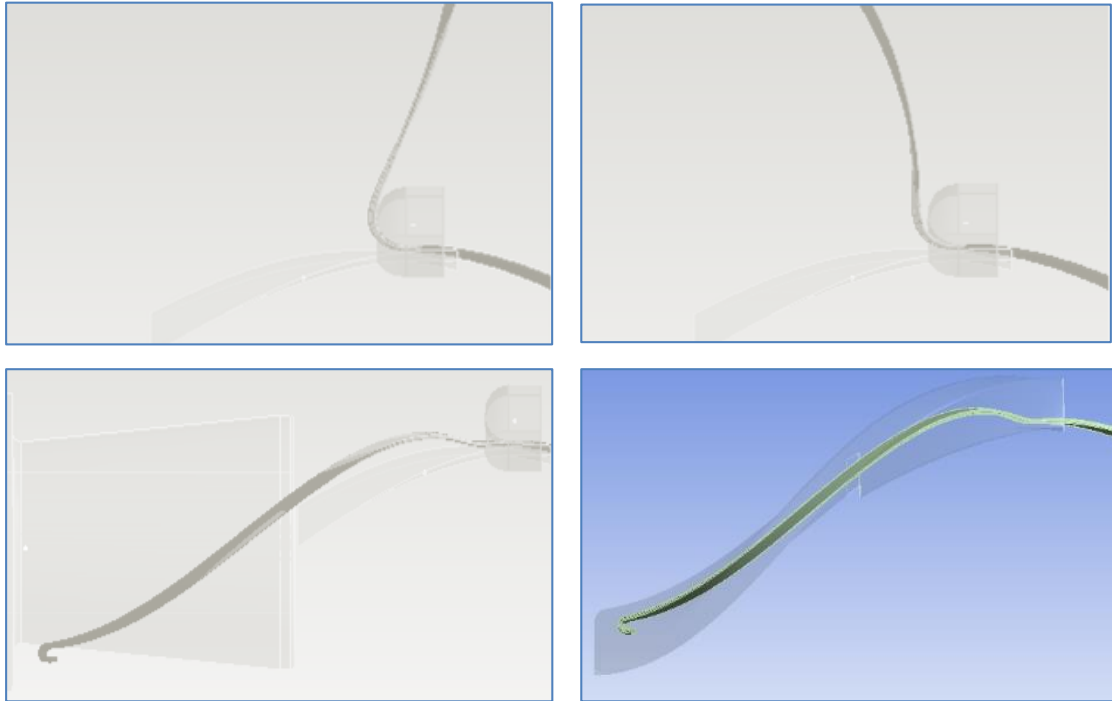


Figure 63. General overview of the simulation steps - Step 4.

The simulation R60A30 is used as base case for step 4. The results of stress decrease inside the EF (capstan effect), the stress relief at CHCP (EF rear area) and residual stress around the CHCP are presented and discussed. For those last two points, the results from simulations R90A30 and R30A30 are presented.

Moreover, some results on the local stress and some points on the alternate and mean stress along the wire are presented for the base case R60A30.

5.10.4.1 STRESS DECAY AND CAPSTAN EFFECT – STUDY WITHOUT RESIDUAL STRESS

For the stress decay and capstan effect analyses, no residual stress was input (R60A30) aiming at studying only the stress decay due to the interaction of the resin and tensile armor wire.

Three levels of loads (UF equal to 0.19, 0.38, 0.64 and 1.00) are studied at point ‘N1’ along the tensile armor wire. Two aspects are studied here: the comparison of the 1st

and 2nd formulations of stress decay inside the EF (presented in items 3.1.3 and 3.1.4) and the comparison of the analytical formulations with the FE model results.

For the 2nd formulation the total length of the wire considered was adjusted in order to have the same total length of the proposed 3D FE based approach.

The first point analyzed is the capstan formulation. The stress decay inside the EF of the 1st and 2nd formulations is plotted in Figure 64. Both formulations have the same magnitude and tendency, considering ' $\tau = 0$ MPa' and ' $\mu = 0.25$ '.

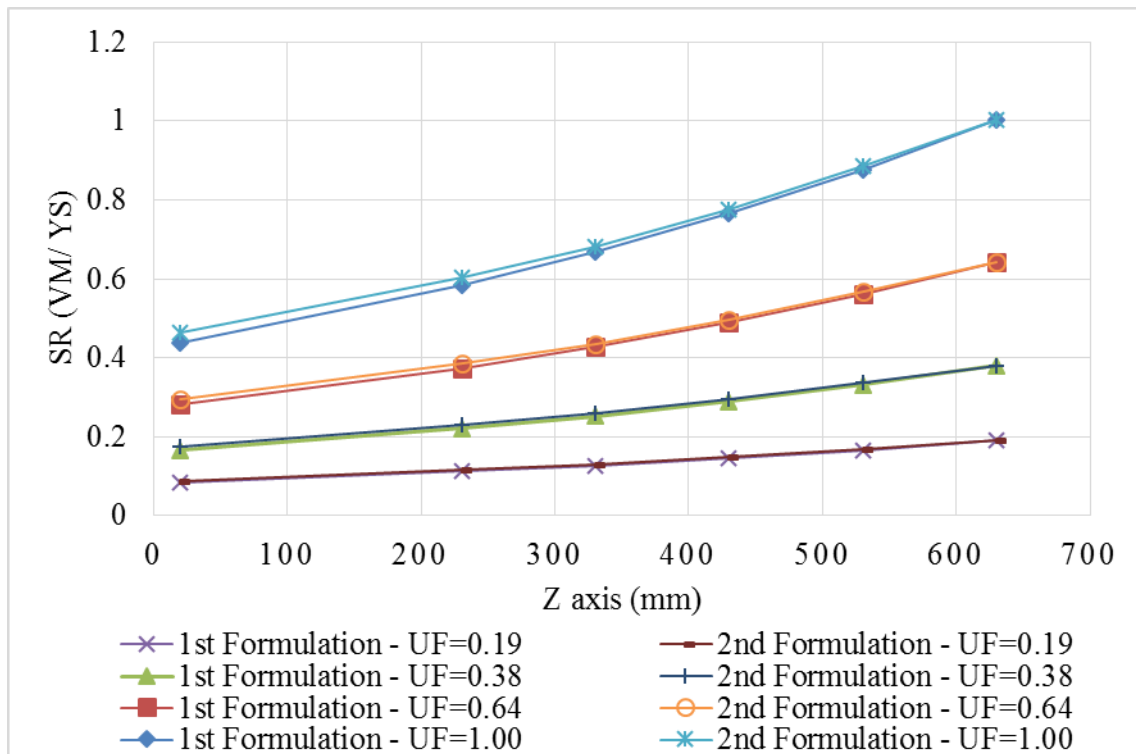


Figure 64. First and second stress decay formulations results for $\tau = 0$ MPa – at point N1 and without residual stress.

The second point is to compare the capstan formulation with the FE model results. In Figure 65, the tendency and magnitude of analytical and FE model results are very similar for the three load cases simulated. The only difference is observed close to the folding region 'CHCP (R=60mm)', where an increase of stress is observed due to deformed geometry in this region.

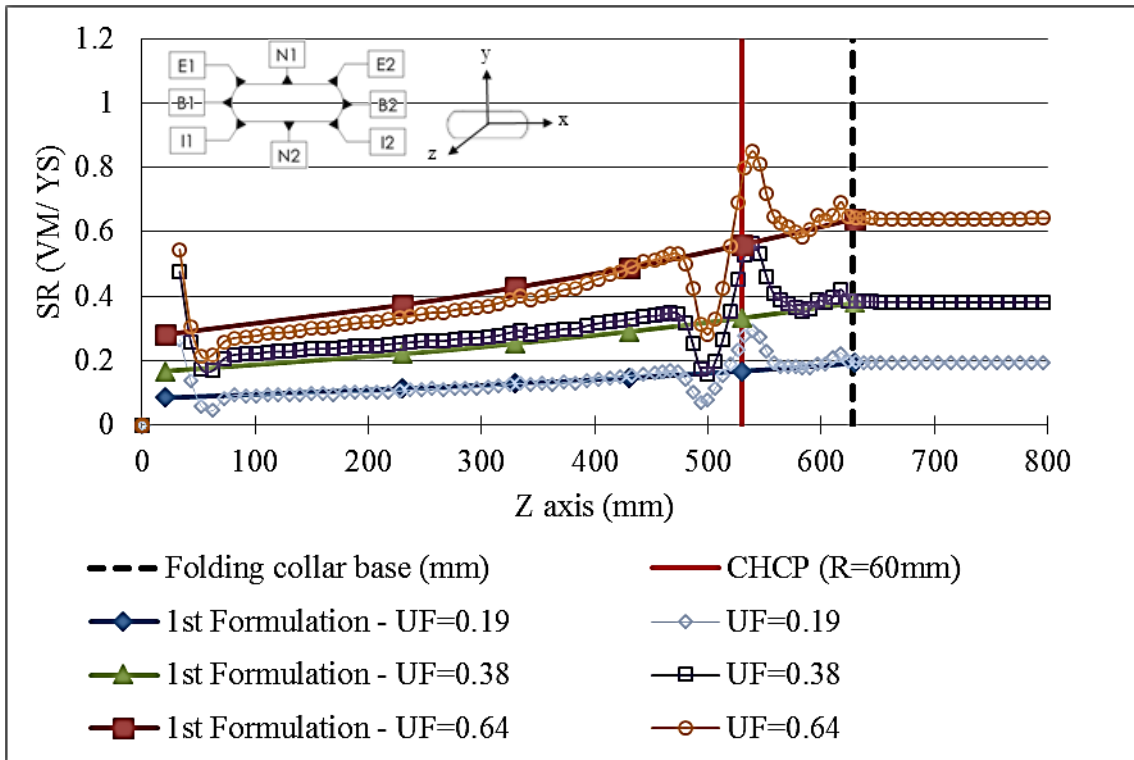


Figure 65. Stress decay or capstan effect results – at point N1 and without residual stress.

Analyzing the analytical and FE model results, the capstan effect has an important decay along the tensile armor wire inside the EF. Similar stress decay inside the EF, when applying several load cases, were also presented by SOUSA *et al.*, (2013) and by CAMPELLO (2014).

5.10.4.1.1 LOCAL STRESS

Locally, at 530 mm – peak stress in Figure 65, ‘CHCP (R=60mm)’– the stresses are probably due to bending at CHCP and the associated deformed geometry in this region. The results presented in Table 16 corroborate this approach, where S_z , S_y and S_{yz} are the predominant stresses, indicating only bending stress at this region.

Table 16. Local stress at 530 mm (UF=0.64) – stress decay analysis without residual stress.

Stress decay analysis without residual stress (MPa)													
Point	VM	Sx		Sy		Sz		Sxy		Syz		Sxz	
N1	1064	6	1%	326	31%	798	75%	-24	2%	-466	44%	26	2%
N2	547	-2	0%	108	20%	370	68%	-2	0%	-251	46%	18	3%
E1	1147	-69	6%	260	23%	769	67%	6	1%	-510	44%	-25	2%
E2	847	-70	8%	201	24%	519	61%	29	3%	-387	46%	-41	5%
I1	547	-1	0%	155	28%	391	71%	-6	1%	-246	45%	11	2%
I2	689	0	0%	180	26%	508	74%	6	1%	-303	44%	-12	2%
B1	848	-3	0%	228	27%	616	73%	-18	2%	-375	44%	24	3%
B2	766	-4	1%	205	27%	560	73%	-26	3%	-334	44%	45	6%

It is important to remark the difference between the VM at points ‘1’ and ‘2’ in Table 16 and in Table 17. The values of N1 and N2 indicates that there is high stress due to normal curvature variation, but low stress due to binormal curvature variation (B1 and B2).

Table 17 also presents the VM local stresses for the three load cases. The VM at peak stress region (CHCP) increases linearly with the applied load. And Table 18 is presented the stress concentration factor (SCF) of the stress decay analysis without residual stress – for the maximum stress found along the tensile armor wire. In the three load cases the maximum SCF is 1.5.

Table 17. VM at 530 mm – stress decay analysis without residual stress.

Step 4 - VM (MPa) (530 mm)			
Point	UF = 0.19	UF = 0.38	UF=0.64
N1	283	556	901
N2	256	503	831
E1	224	447	739
E2	298	581	943
I1	260	499	814
I2	278	544	890
B1	241	479	786
B2	0	0	0

Table 18. SCF of the stress decay analysis (no residual stress).

SCF	UF = 0.19	UF = 0.38	UF=0.64
Sz	1.4	1.4	1.3
VM	1.5	1.5	1.3

5.10.5 STRESS RELIEF AND RESIDUAL STRESS

Table 19 presents the stress relief and residual stress at CHCP. This table shows that the higher is the stress relief (tensile load applied in the tube region, ‘UF’), the lower is the residual stress. The results from this 3D FE based approach and the analytical model from CAMPELLO (2014) had different results of residual stress. The level of stress ratio (SR) of this 3D FE based approach is higher than the one of the analytical model. The two main reasons for that difference are the material law, as discussed before, and the premises of the analytical model that takes the residual stress after the spring-back (step 2) multiplied by a factor for stress relief $(1 - UF_{RELAX})$ – see complete equation in Table 19.

Table 19. Stress relief and residual stress results – step 4 of the model R60A30.

Model	Stress relief (MPa) (1)	Residual stress (MPa) (2)	Analytical (MPa) (3)	UF (1)/YS	SR (2)/YS	SR (3)/YS
R60A30	578	1033	375	43%	0.78	0.28
	658	919	335	49%	0.69	0.25
	755	782	287	57%	0.59	0.22
	892	643	218	67%	0.48	0.16
	1089	346	121	82%	0.26	0.09

$$(3) \sigma_{res} = (1 - UF_{RELAX}) \cdot \left[\frac{t}{2R_g} - \frac{t}{2} \cdot \left(4 \cdot \frac{\varepsilon_y^3 R_g^2}{t^3} - 3 \cdot \frac{\varepsilon_y}{t} + \frac{1}{R_g} \right) - \varepsilon_y \right] \cdot E$$

After stress relief, a new stress field along the wire is observed, as shown in Figure 66, where the stress field from step 3 (unfold) is compared with the residual stresses for three different levels of stress reliefs.

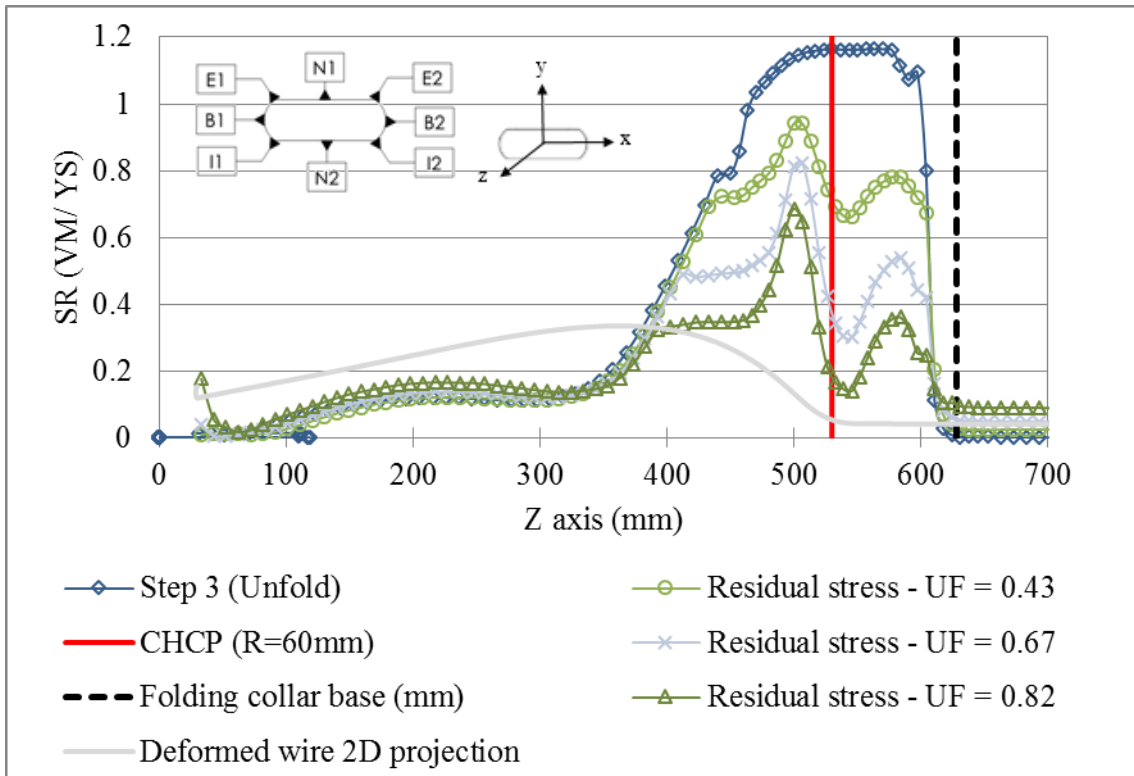


Figure 66. Residual stress results – step 4 of model R60A30.

As expected for all load cases, the curves have the same tendency, but the level of stresses around the CHCP (red curve) are higher than at the CHCP. SOUSA *et al.*, (2013) and CAMPELLO (2014) presented similar results after the stress relief with similar stress field around the folding region (CHCP) of the tensile armor wire.

The lower residual stress at the CHCP might be explained by the over bending in the folding region, as explained in item 5.10.4.1. In Figure 67, for similar load cases, the residual stress (UF = 0.67) and stress decay (UF = 0.64 – without residual stress) curves are plotted. It can be observed that the region at 530 mm (CHCP – red curve), with higher stress during the stress relief, has lower residual stress. The opposite occurs for the region at 500 mm, which sees lower stresses during the stress relief and then higher residual stresses. The differences among the regions close to CHCP are very significant.

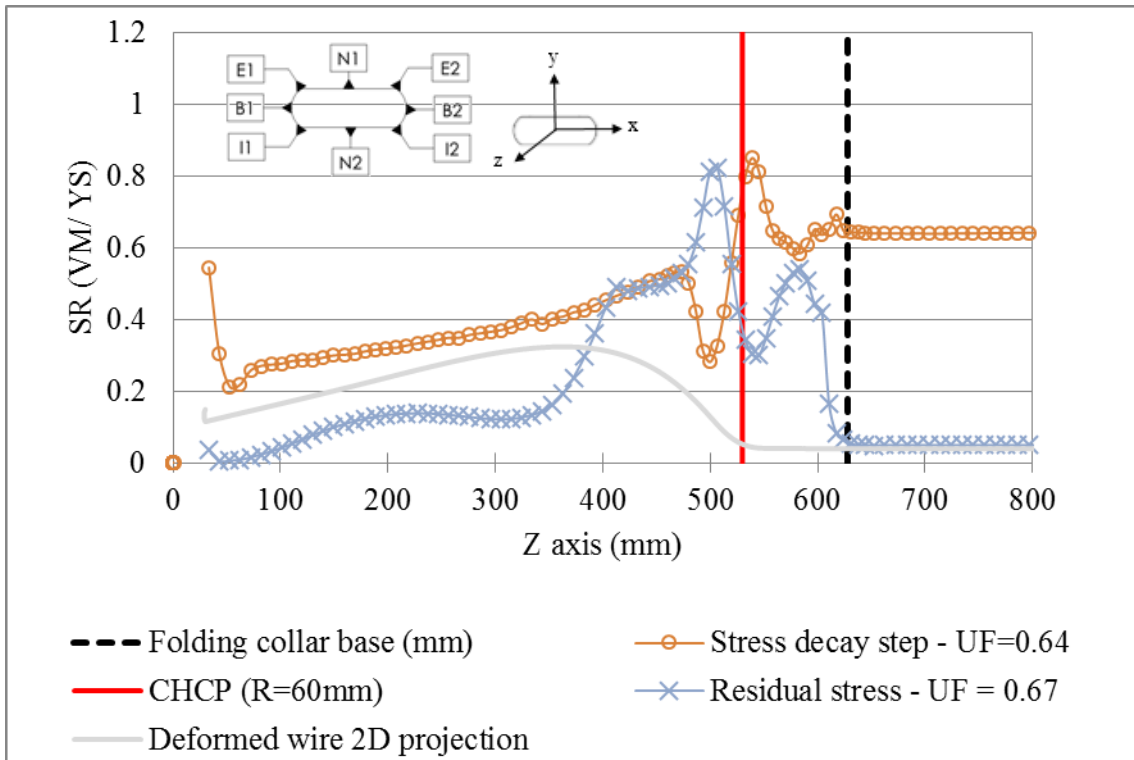


Figure 67. Residual stress and stress decay curves comparison – step 4 of model R60A30.

One important point is the region with the minimum residual stress, which may be one of the most important regions for fatigue analysis. It may have the highest alternate stress due to the high curvature variation as presented in Figure 67.

In Figure 68, the residual stress level after the tensile load at CHCP and the maximum and minimum residual stresses beside this region are similar in tendency, but different in magnitude.

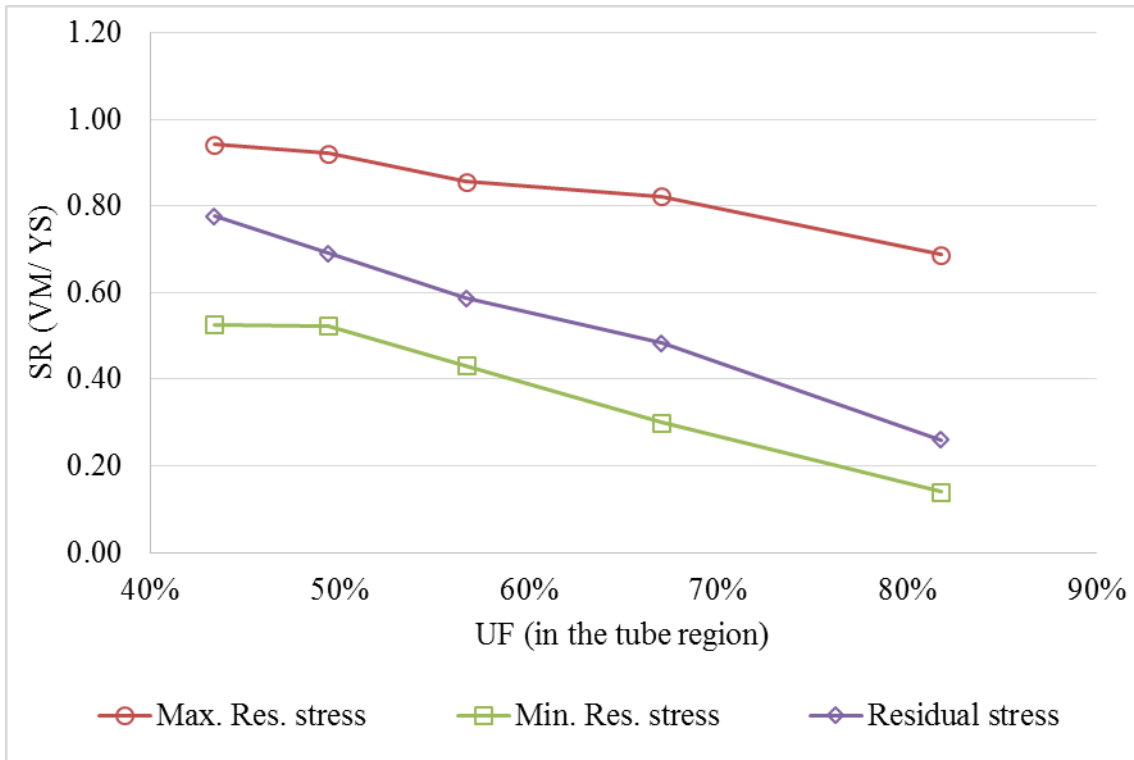


Figure 68. Residual stresses along the tensile armor wire – step 4 of model R60A30.

5.10.5.1 LOCAL STRESS

The local stresses at CHCP are compared with the von Mises equivalent stress (VM) in Table 20 and Table 21, where the percentage is the ratio between the local stress and VM. As can be seen in these tables, at the points N1 and N2, the axial stress (S_z) has the major influence on VM followed by S_y , while S_x is negligible. These results are similar to the ones presented in steps 1 and 3 (Table 14 and Table 15).

Table 20. Stress relief – local stresses at the element nodes at CHCP (step 4, UF = 0.67) – simulation R60A30.

Step 4 - Stress relief (MPa)													
Point	VM	Sx		Sy		Sz		Sxy		Syz		Sxz	
N1	1550	-4	0%	396	26%	1273	82%	-24	2%	-611	39%	10	1%
N2	471	0	0%	-2	0%	-449	95%	-4	1%	81	17%	15	3%
E1	1550	-41	3%	328	21%	1200	77%	-16	1%	-628	41%	20	1%
E2	1550	-37	2%	426	27%	1126	73%	8	1%	-674	43%	-61	4%
I1	498	-3	1%	20	4%	-442	89%	-28	6%	103	21%	59	12%
I2	450	2	0%	-94	21%	-393	87%	-6	1%	158	35%	4	1%
B1	1336	35	3%	241	18%	989	74%	-132	10%	-524	39%	226	17%
B2	1180	2	0%	316	27%	861	73%	12	1%	-525	44%	6	1%

Table 21. Residual stress – local stresses at the element nodes at CHCP (step 4, UF = 0.67) – simulation R60A30.

Step 4 - Residual stress (MPa)													
Point	VM	Sx		Sy		Sz		Sxy		Syz		Sxz	
N1	457	2	0%	66	14%	445	97%	0	0%	-109	24%	-17	4%
N2	1097	1	0%	-157	14%	-943	86%	4	0%	382	35%	-4	0%
E1	403	1	0%	25	6%	371	92%	-3	1%	-106	26%	15	4%
E2	637	5	1%	171	27%	509	80%	-2	0%	-260	41%	-41	6%
I1	1116	-2	0%	-163	15%	-934	84%	-22	2%	405	36%	48	4%
I2	1254	2	0%	-300	24%	-994	79%	-12	1%	513	41%	15	1%
B1	544	40	7%	-14	2%	309	57%	-119	22%	-109	20%	207	38%
B2	323	7	2%	83	26%	221	68%	42	13%	-140	43%	-42	13%

The small value of Sx indicates no significant binormal stress in the CHCP, except for point B1 and B2. It is important to remark that in table Table 16 (stress decay analysis without residual stress) there was no significant in binormal stress in B1 and B2 and no significant shear stress in Sxy and Sxz. Nevertheless, after the step 3 (unfold – see Table 15) there is a significant shear stress in Sxy and Sxz. For that reason one can conclude that the shear stress Sxy and Sxz are more consequence from the folding and unfolding process than from the tensile load applied in the wire.

Other interesting point is the local stress at intrados (I1 and I2), where the stresses (S_z) is still negative even during stress relief or tensile load (Table 20). This may be an evidence for low probability of failures at intrados of the tensile armor wire.

In the stress relief (Table 21), a difference between the stresses at points '1' and '2' is observed. Opposing evidence is presented in item 5.10.4.1.1 (stress decay analysis), where the stress at '1' is higher than '2'. This means that, during the stress relief, the stresses at '1' are higher than '2' providing a lower residual stress for point '1' after unloading. Two important points must be mentioned here: the higher is the load, the higher is the stress relief at each point (1 or 2); the second point is the local bending stress due to the deformed shape of the tensile armor wire at CHCP, which leads to a higher stress relief and consequently lower residual stress.

5.10.6 STRESS CONCENTRATION FACTOR, ALTERNATE AND MEAN STRESS

In this item, the base case studied is the simulation R60A30 after stress relief of $UF = 82\%$.

Figure 69 presents the stress field at point N1 under different load cases. As can be seen in Figure 69, the level of bending stress is more important at CHCP than in regions near it. As discussed before, this difference of stress level may lead to a more important alternate stress at this region (CHCP). This aspect is discussed hereafter.

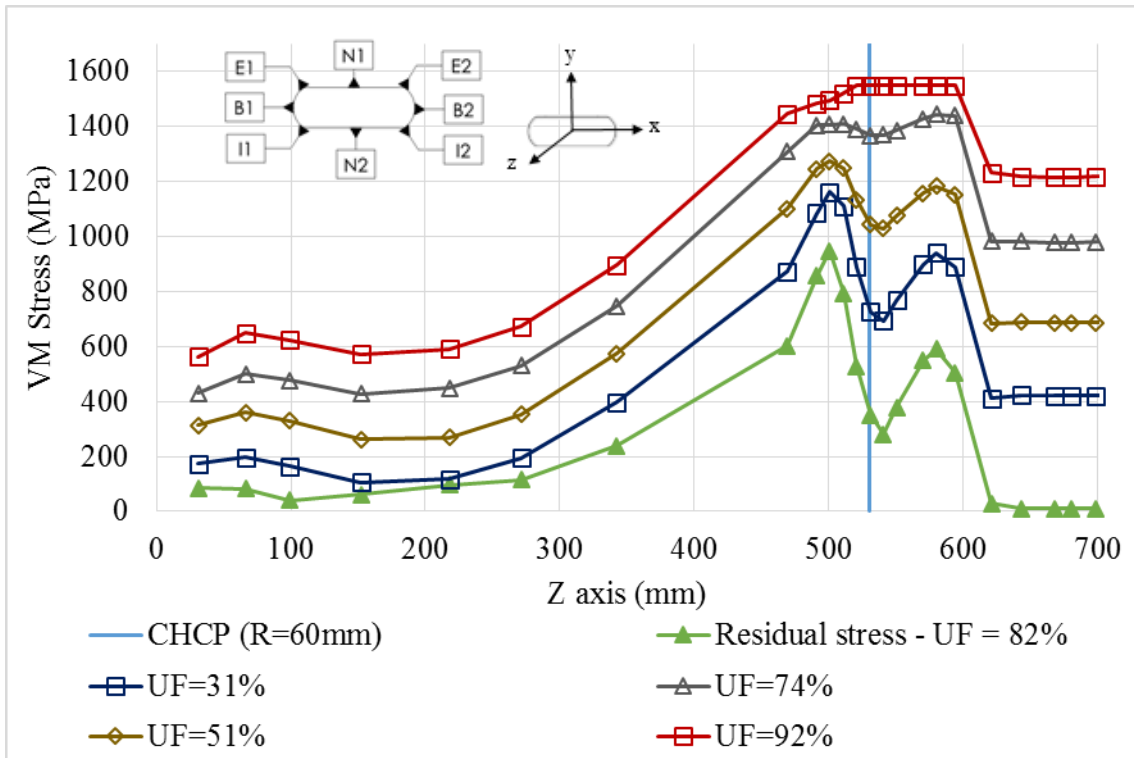


Figure 69. Stress level under different loads after stress relief (UF=82%) – point N1.

The stress concentration factor (SCF) directly depends on the load applied in the stress relief. Figure 70 shows the SCF for the VM and Figure 71 shows the SCF for the local stress ‘Sz’. In both figures the level of SCF is higher for lower loads, as UF = 31% and 51%. Low tensile load levels presented a SCF between 1.5 and 3.0. This result is similar to the one presented by XAVIER (2009) (load case with partially bonded wire and load case with no adhesion between resin and tensile armor wire) and SOUSA *et al.*, (2013).

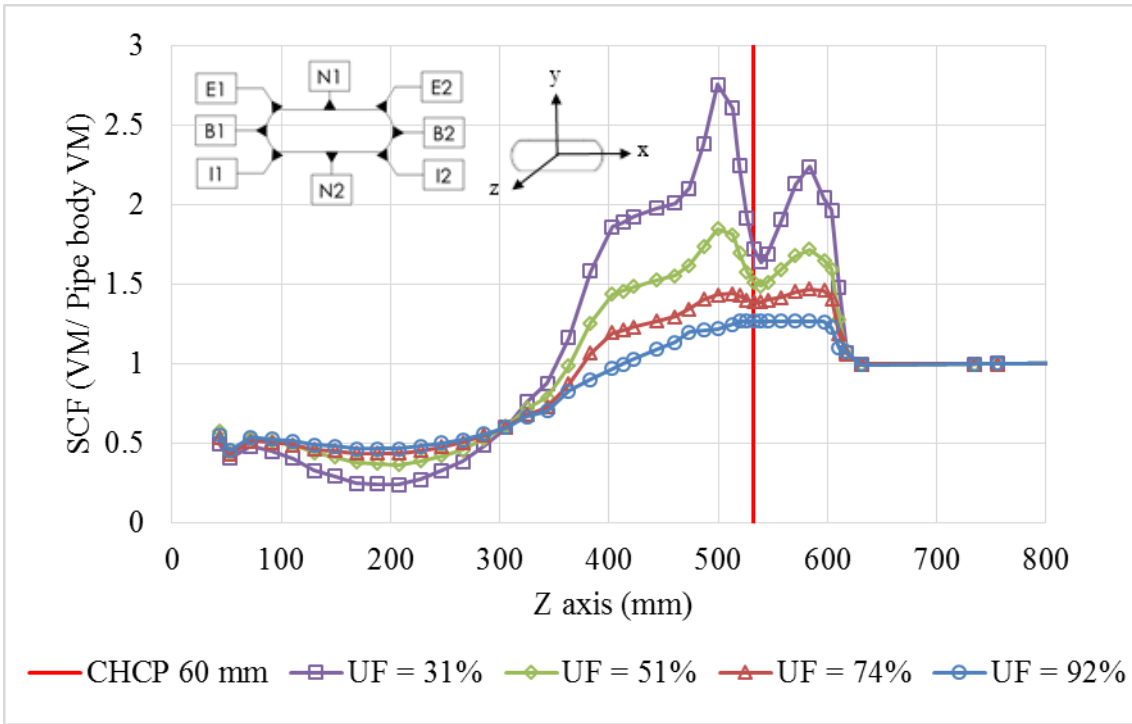


Figure 70. Von Mises (VM) stress concentration factor of R60A30 (stress relief of UF=82%) – point N1.

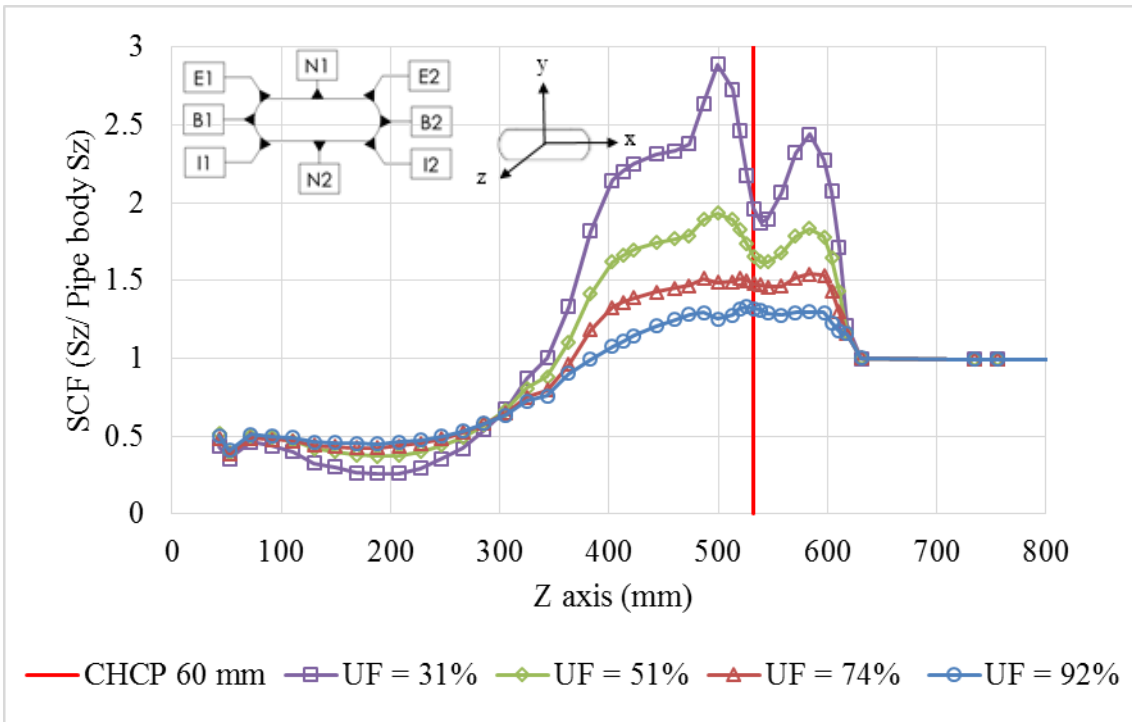


Figure 71. Local (Sz) stress concentration factor of R60A30 (stress relief of UF=82%) – point N1.

For the alternate and mean stress analyses, the considered minimum stress was the curve UF=31% and the considered maximum stresses were UF=51%; 74% and 92% from Figure 69.

As discussed before, there is an important effect of the bending stress at the CHCP. This is evident in Figure 72, where the mean stresses and the alternate stresses are plotted.

To sum up, CHCP have the lowest mean stress but the highest alternate stress whereas the regions around CHCP have the highest mean stress and the lowest alternate stress. For this reason, the region at CHCP and regions around CHCP may be evaluated for fatigue analyses.

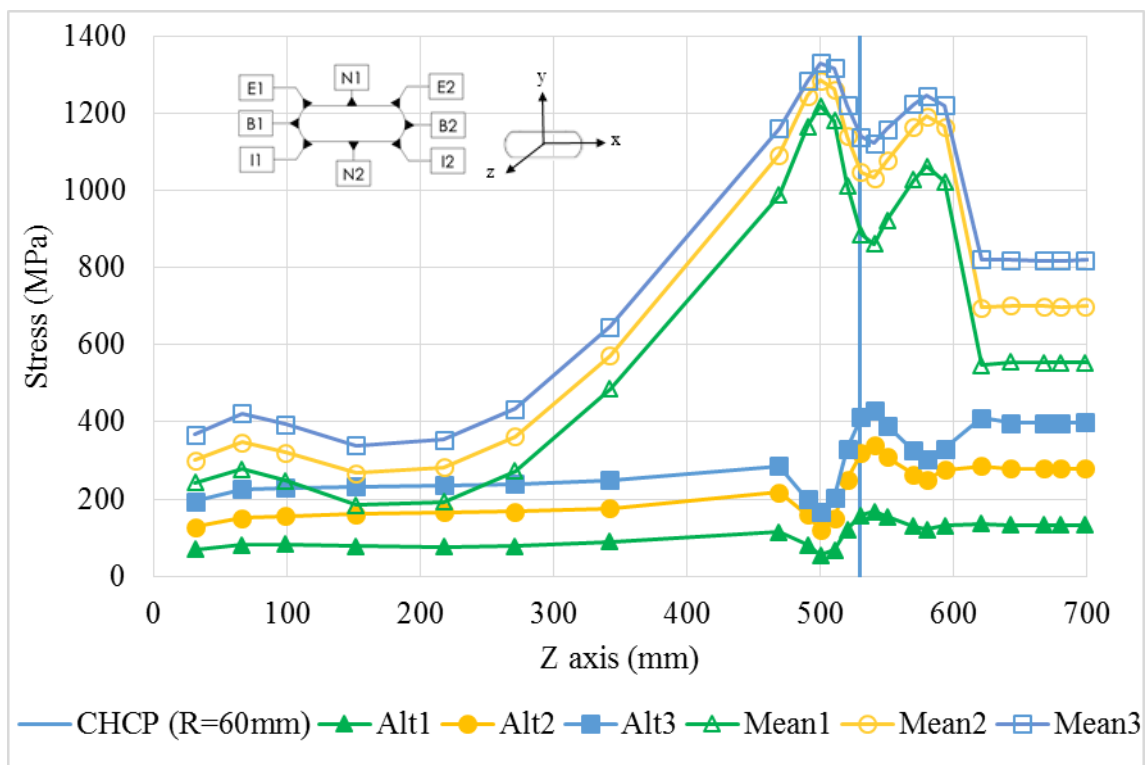


Figure 72. Alternate and mean stress of R60A30 – point N1.

Figure 73 and Figure 74 presents the stress concentration factor (SCF) at point N1 of the pairs: maximum alternate stress with the minimum mean stress and minimum alternate stress with the maximum mean stress presented in Figure 72.

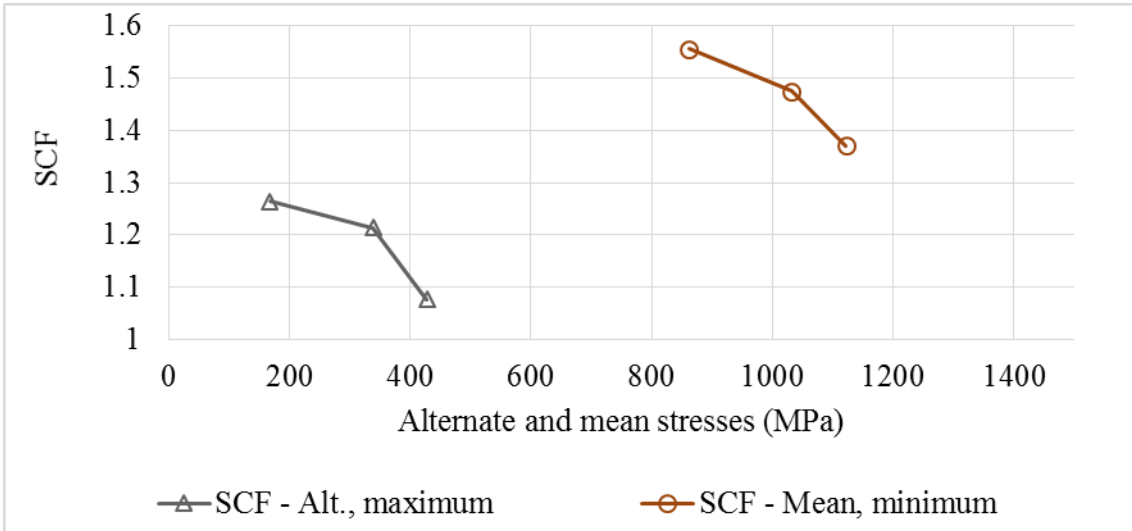


Figure 73. SCF of the pair maximum alternate stress with the minimum mean stress – point N1.

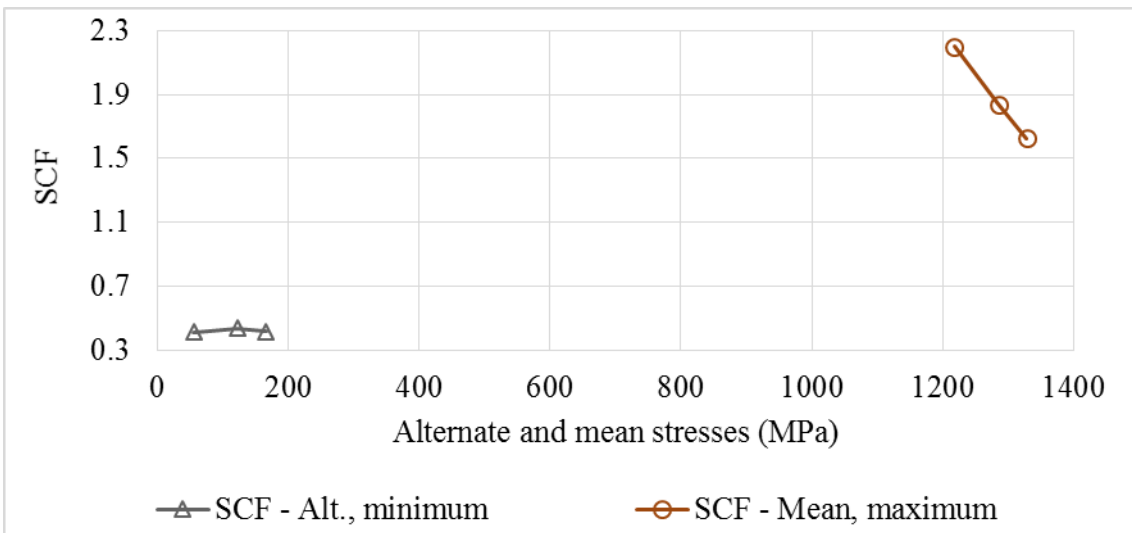


Figure 74. SCF of the pair minimum alternate stress with the maximum mean stress – point N1.

5.10.7 RESIDUAL STRESS IN R30A30, R60A30 AND R90A30 SIMULATIONS

Figure 75 presents the residual stress of the proposed models at CHCP after stress relief for several load cases (UFs).

As expected, the results show that the residual stress decreases when increasing the folding collar radius (R_g) and when increasing the tensile load in the tube (UF). Other important point is the linearity of the residual stresses results at CHCP.

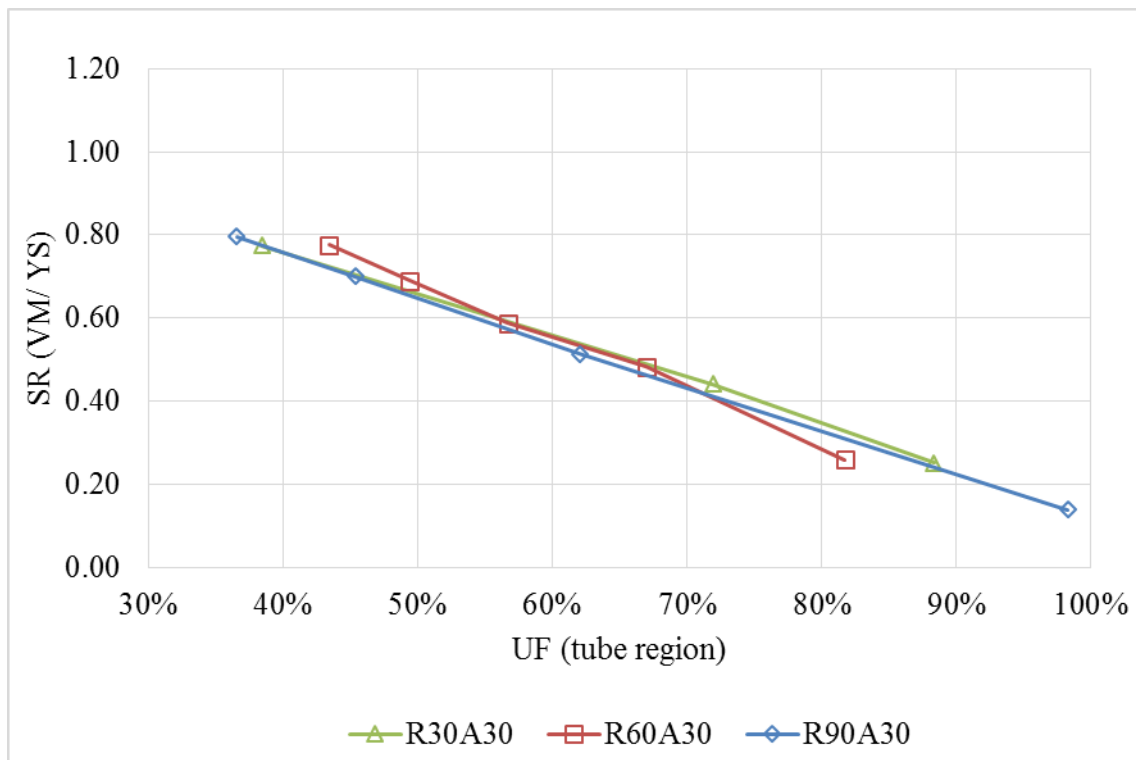


Figure 75. Residual stress with different collar folding radius at CHCP.

Nevertheless, the level of minimum and maximum stresses around the CHCP are not as similar as the one presented in Figure 75.

The minimum stress around the CHCP is lower for smaller folding radius (Figure 76). This is due to the level of bending stress that tends to be higher for smaller ' R_g ' providing high level of stress relief.

The maximum stress around the CHCP is lower for larger folding radius (Figure 77). This is expected because of the level of stress presented in step 3 that was lower for larger ' R_g '.

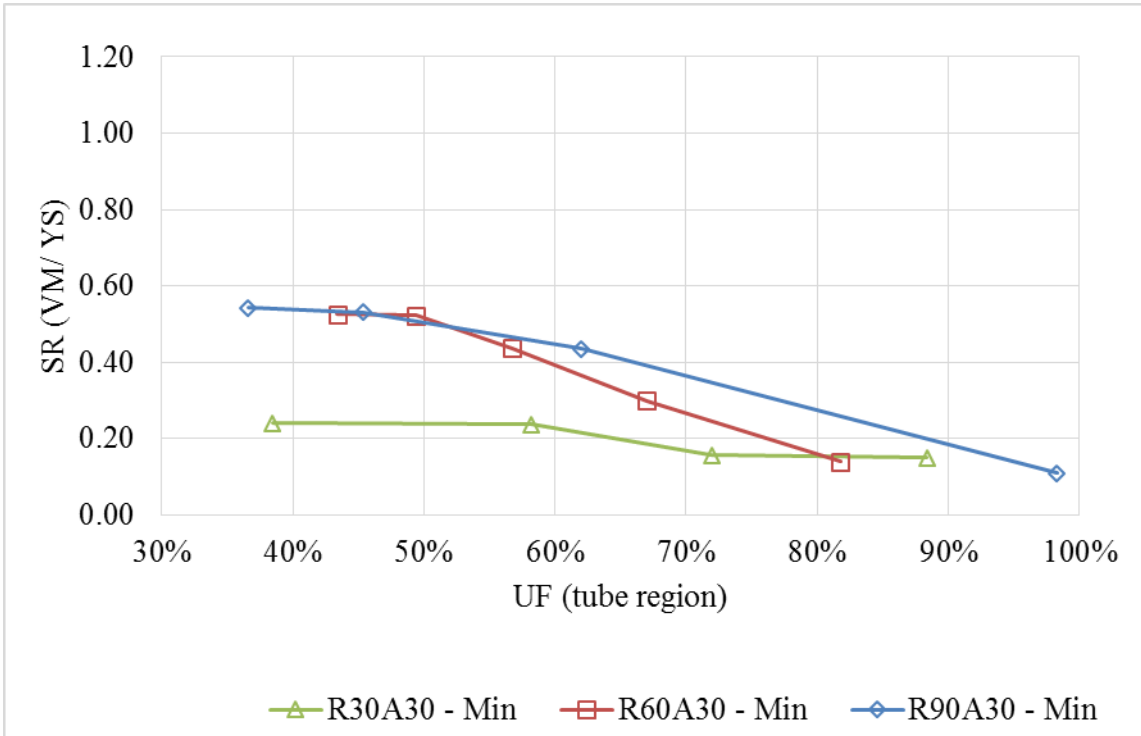


Figure 76. Minimum residual stress with different collar folding radius around CHCP.

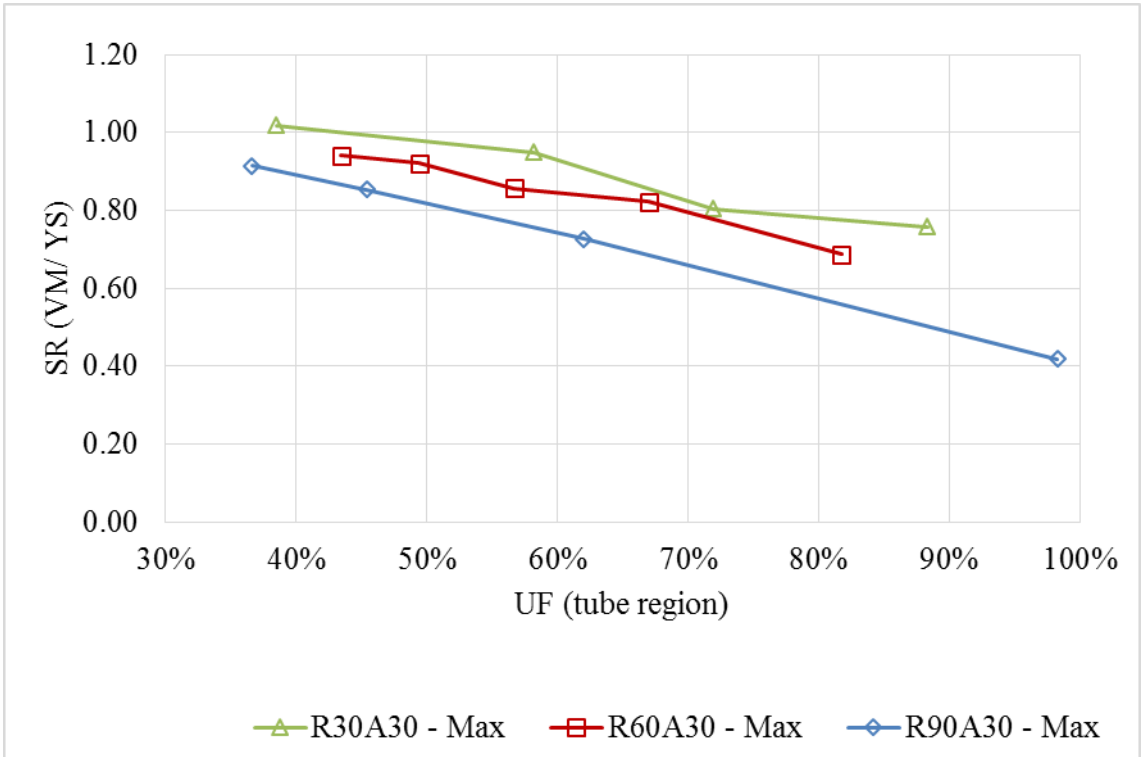


Figure 77. Maximum residual stress with different collar folding radius around CHCP.

CHAPTER 6

CONCLUSIONS AND FUTURE WORKS

6.1 CONCLUSIONS

This work had the objective to study the stress distribution along one tensile armor of a flexible pipe during the end-fitting mounting process and after, during operational loads. In order to perform this analysis, a 3D FE based approach was developed based on two FE models. The results had good agreement with analytical models available in the literature.

The conclusions of this work presented here below may be useful in the formulation of analytical models for fatigue analyses or to be implemented in simpler FE models:

- The folding collar radius (R_g) to be considered in the analytical methodology or in a 2D FE model is dependent on the folding angle – usually, the folding angle is the armoring angle. The collar projection gives an ellipse shape, which is smaller than R_g .
- When the folding angle α' decreases (approximate to zero in relation to the tube axis – see ' α' ' in Figure 25) the maximum strain level of the wire at step 1 approximates to the collar radius (R_g) strain level.
- In step 1 (folding process), large R_g results in lower maximum strain. However, R_g higher than 80 mm does not lead to significant decrease on the maximum strain or in the residual radius after the spring back effect (step 2) for the studied wire geometry with 5 mm of thickness.
- The decrease of the folding angle in step 1 decreases the maximum strain, but has no much influence on the residual radius in steps 2 and 3 but it can – locally in the folding region – induce different shear stress.

- The residual radius and the residual stress in steps 2 and 3 (Figure 59) have a linear behavior when increasing the R_g .
- The residual radius in step 3 is higher than the one of step 2 (spring-back effect), which is approximately 1.5 times higher for $R_g = 60$ mm and 90 mm; and approximately 2.5 times higher for the $R_g = 30$ mm.
- In step 1, the extrados of the tensile armor wire sees compressive stress and in step 3 sees tensile stress, the inverse occurs in the intrados of the wire. Moreover, in steps 1 and 3 the stress level reaches approximately the UTS of the material.
- The stress decay inside the EF has good agreement with the 1st formulation and the 2nd one proposed by CAMPELLO (2014). It must be remarked that, for a full EF, the stress decay has the influence of the internal armor layer. For this case, the 1st and 2nd formulations could be adapted to include that contribution on the stress decay.
- The local stress at intrados (I1 and I2) is still negative because of the compressive residual stresses even during the tensile load. That may be one evidence for low probability of failures at intrados of the tensile armor wire in the field.
- Due to the high bending stress in the folding region (CHCP), the stress relief in that area was higher. It has an important impact on the alternate and mean stresses.
- The results presented here indicates that this folding/ unfolding process could be approximately modelled as a 2D phenomenon.
- CHCP region have the lowest mean stress but the highest alternate stress whereas the regions around CHCP have the highest mean stress and the lowest alternate stress. For this reason, the region at CHCP and regions around CHCP may be evaluated for fatigue analyses.

- A linear model could be implemented for residual stress at the point with the maximum deformation in the folding process (step 1). At that point the level of SCF was the same for R_g of 30mm, 60mm and 90 mm for this specific studied geometry. But the level of SCF around this point have not the same magnitude. Larger R_g leads to lower maximum SCF and higher minimum SCF, less severe condition.
- Some points regarding the residual radius and the residual stresses were raised here and these points must be worked out in the analytical model for fatigue analysis. In order to access the final residual radius and improve an analytical methodology for several combinations of EF geometries, this 3D FE based approach could be used.

6.2 FUTURE WORKS

Some studies to complement this work are suggested:

- Study the adhesion and the friction coefficient of the pair tensile armor wire and resin under different levels of contact pressures. Experimental tests taking into account the phenomena that occurs inside the EF are required.
- Evaluate the mechanical properties of the epoxy resin in confined environments – representative of the resin inside the EF.
- Develop a 2D FE model to compare with the results presented in this work.
- Use this 3D FE based approach to simulate several tensile armor wire and EF geometries and try to find a global curve for residual radius, residual stress, SCFs for the alternate and mean stress etc.
- Run a complete FE model with all tensile armor layers to compare with the stress decay formulations and also evaluate the influence of binormal

stress due to the proximity of the wires and possible changes of stiffness around the wire due to the interaction among the wires and the resin.

- Perform a full-scale test to validate the stress decay of this 3D FE based approach and analytical formulations.

BIBLIOGRAPHY

AMERICAN PETROLEUM INDUSTRY, *Recommended Practice for Flexible Pipe*, 17B, 5th ed., USA, 2014.

AMERICAN PETROLEUM INDUSTRY, *Specification for Unbonded Flexible Pipe*, 17J, 3rd ed., USA, 2009.

ANSYS, 2014, *Reference Manual (version 14.5)*, ANSYS Inc.

BARTELL, *Carcass Machines*, 2015. Available in:

http://www.bartellmachinery.com/carcass-machines?page_id=55. Accessed in: 11 March 2015.

BARTELL, *Tensile Armouring Machines*, 2015. Available in:

<http://www.bartellmachinery.com/tensile-armouring-machines>. Accessed in: 11 March 2015.

BECTARTE, F., COUTAREL, A., “Instability of Tensile Armour Layers of Flexible Pipes under External Pressure”. *23rd International Conference on Ocean, Offshore and Arctic Engineering*, 51352, Vancouver, Canada, 20-25 June 2004.

BENIRSCHKE, C., 2014, *Análise de Tensões em Conectores de Linhas Flexíveis*, Dissertação* de M.Sc., COPPE/UFRJ, Rio de Janeiro, RJ, Brazil.

BOUN, E., AIGNAN M., S., BERTON, H., APPLECROSS, 2005, *End-fitting for flexible pipe*, US6923477B2, 16 May 2002, 2 August 2005, United States Patent, USA.

BROWN, I. F., BURGOYNE, C. J., “The Friction and Wear of Kevlar 49 Sliding Against Aluminum at Low Velocity under high Contact Pressures”, *Journal of Wear*, v. 236, pp. 315-327, July 1999.

BUENO, A. F. B., 2010, *Avaliação das Armaduras de Tração de Riser Flexível Durante Ensaio Axiais de Tração e Fadiga*. Dissertação* de M.Sc., Universidade Federal do Rio Grande do Sul, Porto Alegre, RS, Brazil.

CAMPELLO, G. C., BERTONI, F., SOUSA, J. R. M., CAPIGIANI, M. A., VARDARO, E., MUDRY, G., “A Novel Concept of Flexible Pipe End Fitting: Tensile Armor Foldless Assembly”, *31st International Conference on Ocean, Offshore and Arctic Engineering*, 83511, Rio de Janeiro, RJ, Brazil, 1-6 July 2012.

CAMPELLO, G. C., 2014, *Metodologia de Projeto para o Sistema de Ancoragem de Conectores de Dutos Flexíveis e Proposição de Nova Tecnologia*. Tese* de D.Sc., COPPE /UFRJ, Rio de Janeiro, RJ, Brazil.

DAFLON, M. B., 2010, *Estudo de Aderência de Arames de Armadura de Tração em Conectores de Dutos Flexíveis*, Dissertação* de M.Sc., Universidade do Estado do Rio de Janeiro, Nova Friburgo, RJ, Brazil.

DIETIER, E. G., 1998, *Mechanical Metallurgy*, 2nd ed. London, McGraw-Hill.

FERET, J. J., BOURNAZEL, C. L., “Calculation of Stresses and Slip in Structural Layers of Unbonded Flexible Pipes”, *Journal of Offshore Mechanics and Arctic Engineering*, v. 109, pp. 263-269.

FERNANDO, U. S., DAVIDSON, M., SHELDRAKE, T., “Critical Assessment of PVDF Multilayer Barriers in Unbonded Flexible Risers: Applications and Benefits”, *32nd International Conference on Ocean, Offshore and Arctic Engineering*, 11237, Nantes, France, 9-14 June 2013.

INTERNATIONAL ENERGY AGENCY, *World Energy Investment Outlook*, 2014. Available in:
<http://www.iea.org/publications/freepublications/publication/weio2014.pdf>. Accessed in: 08 March 2015.

LAMBERT, A., FELIX-HENRY, A., GILBERT, P., GAINVILLE, M., “Experimental and Numerical Study of a Multi-layer Flexible Pipe Depressurization”, *31st International Conference on Ocean, Offshore and Arctic Engineering*, 83127, Rio de Janeiro, RJ, Brazil, 1-6 July 2012.

MARINHO, M. G., CAMERINI, C. S., DOS SANTOS, J. M., PIRES, G. P., “Surface Monitoring Techniques for a Continuous Flexible Riser Integrity Assessment”, *Offshore Technology Conference*, 18946, Houston, Texas, USA, 30 April-3 May 2007.

MERINO, H. E. M., SOUSA, J. R. M., MAGLUTA, C., ROITMAN, N., “On the Coupled Extensional-Torsional Response of Flexible Pipes”, *28th International Conference on Ocean, Offshore and Arctic Engineering*, 79468, Honolulu, Hawaii, USA, 31 May-5 June 2009.

PAUMIER, L., MESNAGE, O., “PSI Armour Wire for High Collapse Performance of Flexible Pipe”, *30th International Conference on Ocean, Offshore and Arctic Engineering*, 49257, Rotterdam, The Netherlands, 19-24 June 2011.

PETROBRAS, *Sustainability Report*, 2015. Available in:

<http://www.petrobras.com.br/en/society-and-environment/sustainability-report/>.

Accessed in: - 08 March 2015.

SHEN, Y., MA, F., TAN, Z., SHELDRAKE, T., “Development of the End Fitting Tensile Wires Fatigue Analysis Sample Tests and Validation in an Unbonded Flexible Pipe”, *Offshore Technology Conference*, 19197, Houston, Texas, USA, 5-8 May 2008.

SOUSA, J. R. M., CAMPELLO, G. C., BERTONI, F., ELLWANGER, G. B., “A FE Model to Predict the Stress Concentration Factors in the Tensile Armor Wires of Flexible Pipes Inside End Fittings”, *32nd International Conference on Ocean, Offshore and Arctic Engineering*, 10995, Nantes, France, 9-14 June 2013.

TECHNIP, *Coflexip® Product Division - Engineering Solutions for the Petrochemical and Refining Industry*, 2013. Available in:
http://www.technip.com/sites/default/files/technip/page/attachments/Refining_Draps_July%202013_Web.pdf . Accessed in: 10 March 2015.

TECHNIP, *User's Guide Coflexip® Flexible Pipe for Drilling and Service Applications*, 2013. Available in:
http://www.technip.com/sites/default/files/technip/field_activity/attachments/drilling_users_guide_august_2013_web.pdf . Accessed in: 01 March 2015.

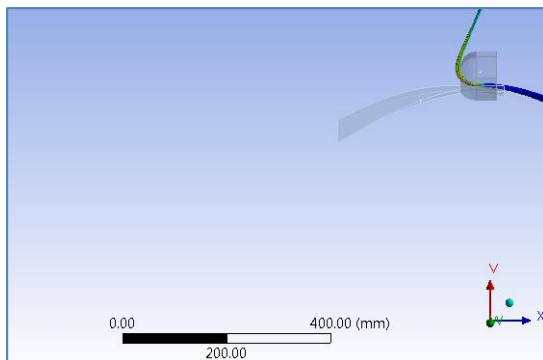
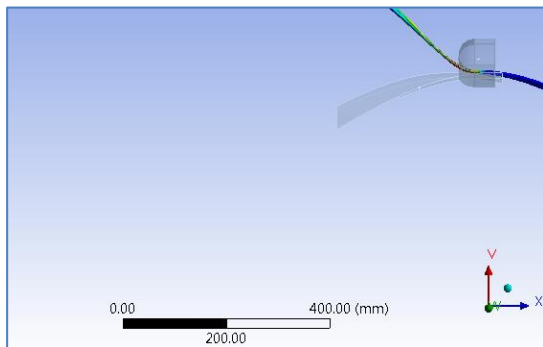
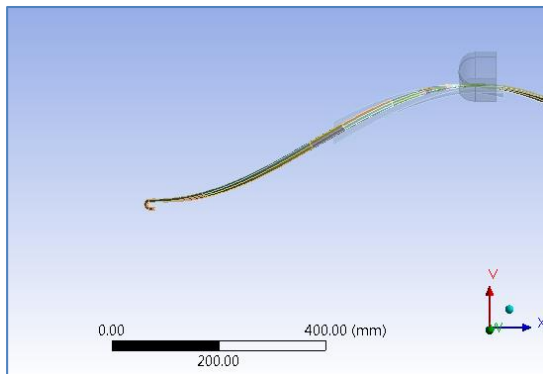
XAVIER, F., 2009, *Avaliação da Vida em Fadiga de um Novo Modelo de Terminal Conector para Dutos Flexíveis*. Tese* de D.Sc., Universidade Federal do Rio Grande do Sul, Porto Alegre, RS, Brazil.

APPENDIX A

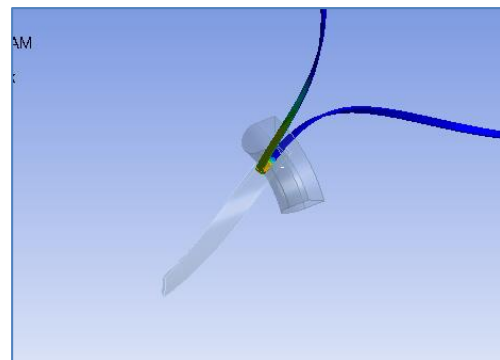
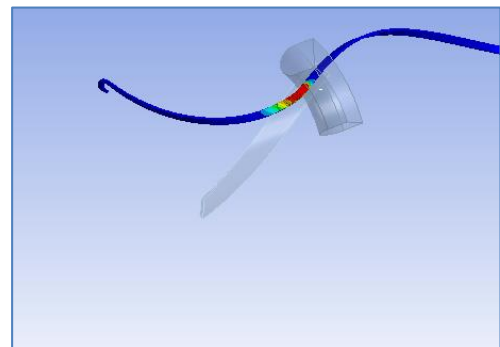
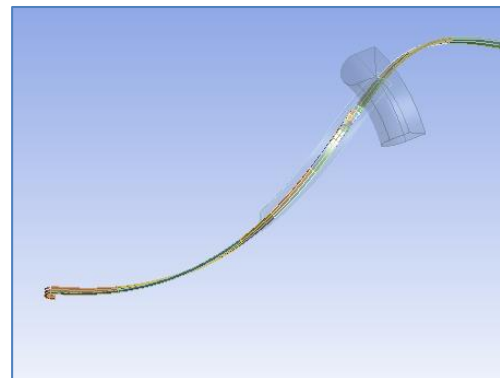
SNAPSHOTS OF EACH STEP (1 TO 3) OF THE FOLDING/ UNFOLDING 3D FE MODEL

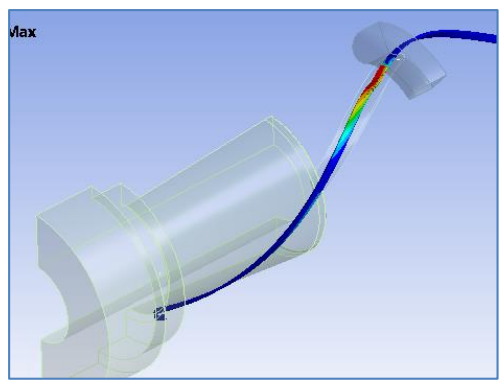
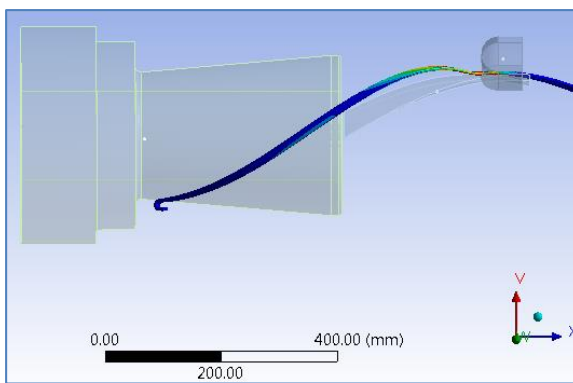
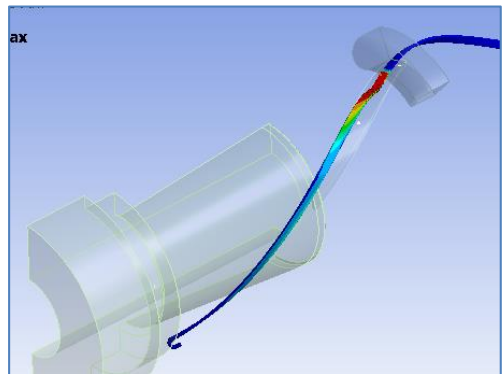
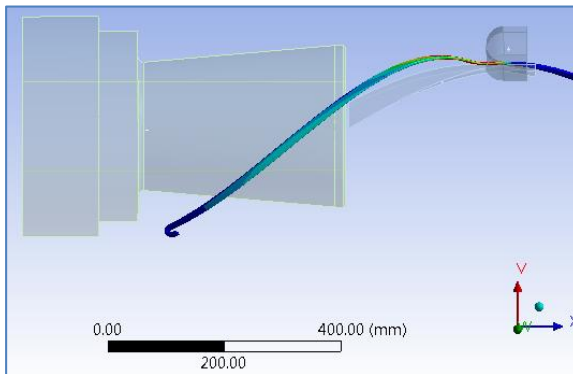
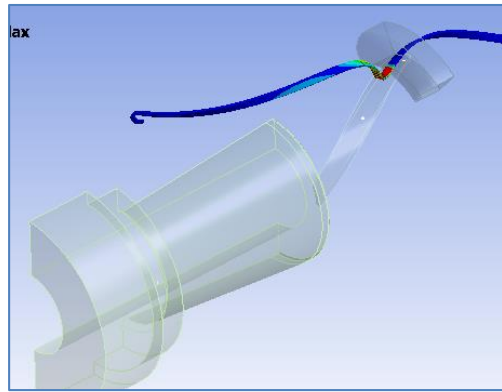
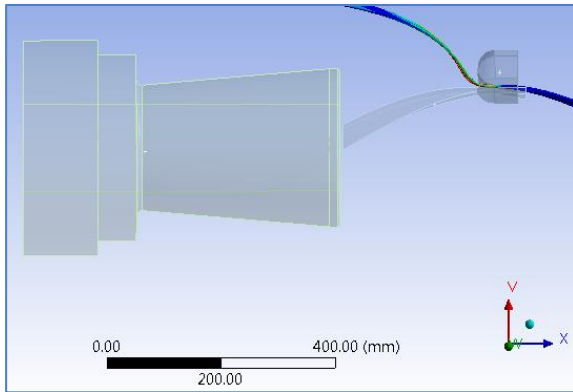
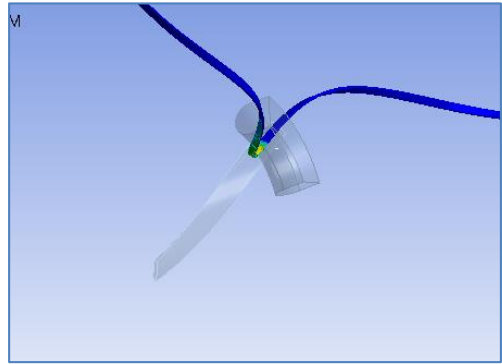
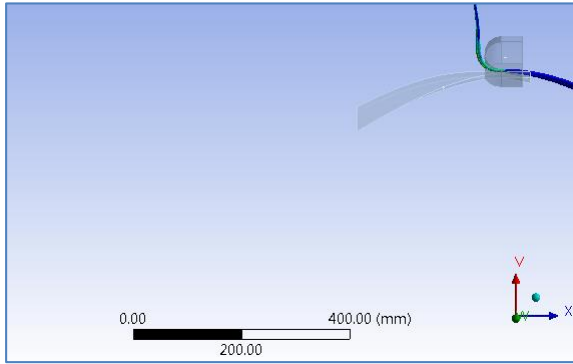
A.1. STEP 1 TO 3

XY PLANE VIEW



ISOMETRIC VIEW





APPENDIX B

ONE WIRE AXISYMMETRIC VALIDATION – FE MODEL

B.1. FE X ANALYTICAL MODEL

This simplified FE based model aims to validate the boundary condition (BC) applied on step 4 of the folding/unfolding model of this work.

This simplified FE model has one tensile armor wire with its radial displacement restricted. One side of the wire is fixed and in the other side a tensile load is applied with an imposed displacement. The results of this FE model are compared those obtained with the traditional analytical model proposed by FERET *et al.* (1987).

The tensile armor wire section of this FE model is the same presented in 5.2.2 with a total length of 850 mm. The FE model premises (item 4.4.3) and boundary conditions (BCs) are the same applied on step 4 of the folding/ unfolding FE model. The BCs applied on this model are shown in Figure 78, and explained hereafter:

- a) BC-A – no radial displacement at internal face of the wire (intrados – red face).
- b) BC-B – axial displacement imposed to the wire's section in the Z axis.
- c) BC-C – fixed remote point linked to wire's face.

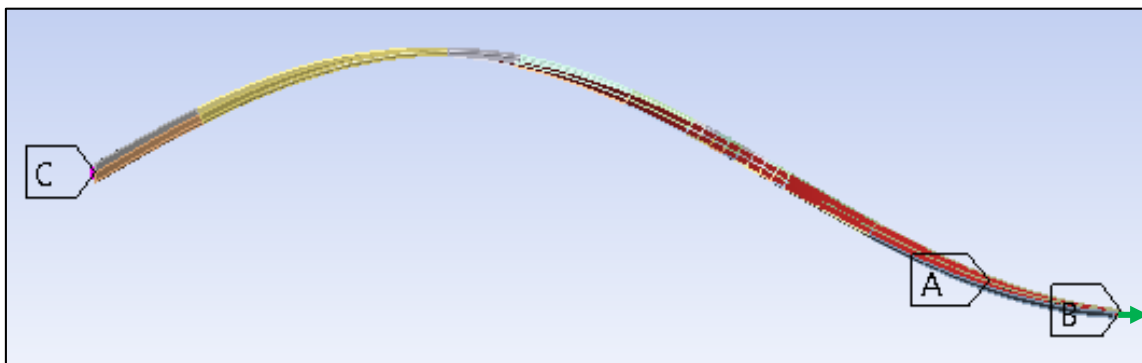


Figure 78. Boundary conditions of the axisymmetric model.

The mesh is similar to the one used on the folding/ unfolding FE model and its characteristics are presented in Table 22.

Table 22. Mesh characteristics – axisymmetric FE model.

N° of nodes	N° of elements	Size (mm ²)	Element type
81129	15616	3 x 3	SOLID 186

B.2. RESULTS AND CONCLUSIONS

Figure 79 shows the region with bending stress due to the boundary conditions (BC-C – fixed point). The difference of ‘VM’ at the intrados corners reaches almost 200 MPa (VM far from that region is approximately 700 MPa – see Figure 79 and Figure 80). It is an expected result in this FE model and may happen in the folding/ unfolding model due to the constraint at the resin entrance (EF rear region is similar to a fixed point).

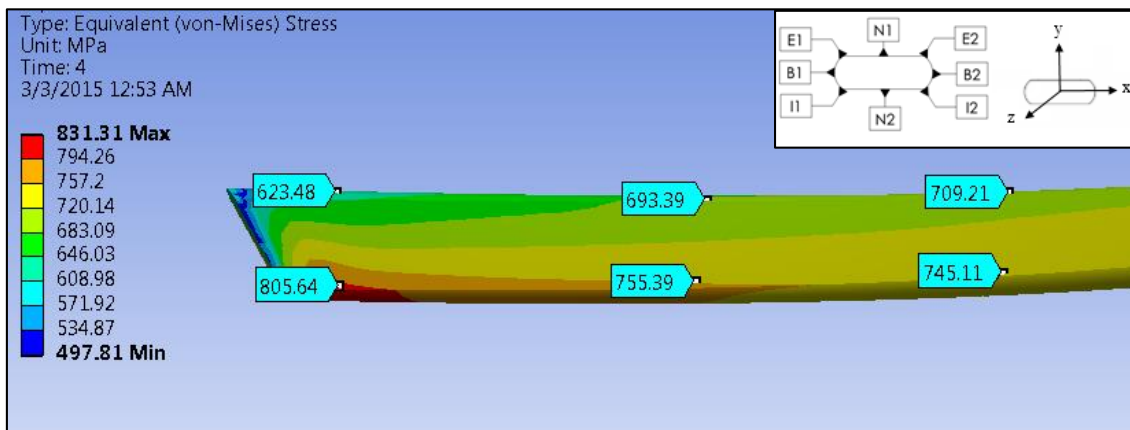


Figure 79. Armor wire’s intrados (points I1 and I2) at the fixed point (BC-C) – axisymmetric FE model.

In order to evaluate the bending effect on the wire due to the BCs of the model, the stresses along the wire on both corners of the extrados are plotted in Figure 80. As can be seen in Figure 80, the bending effect drops quickly and no major influence occurs after 200 mm from the fixed point.

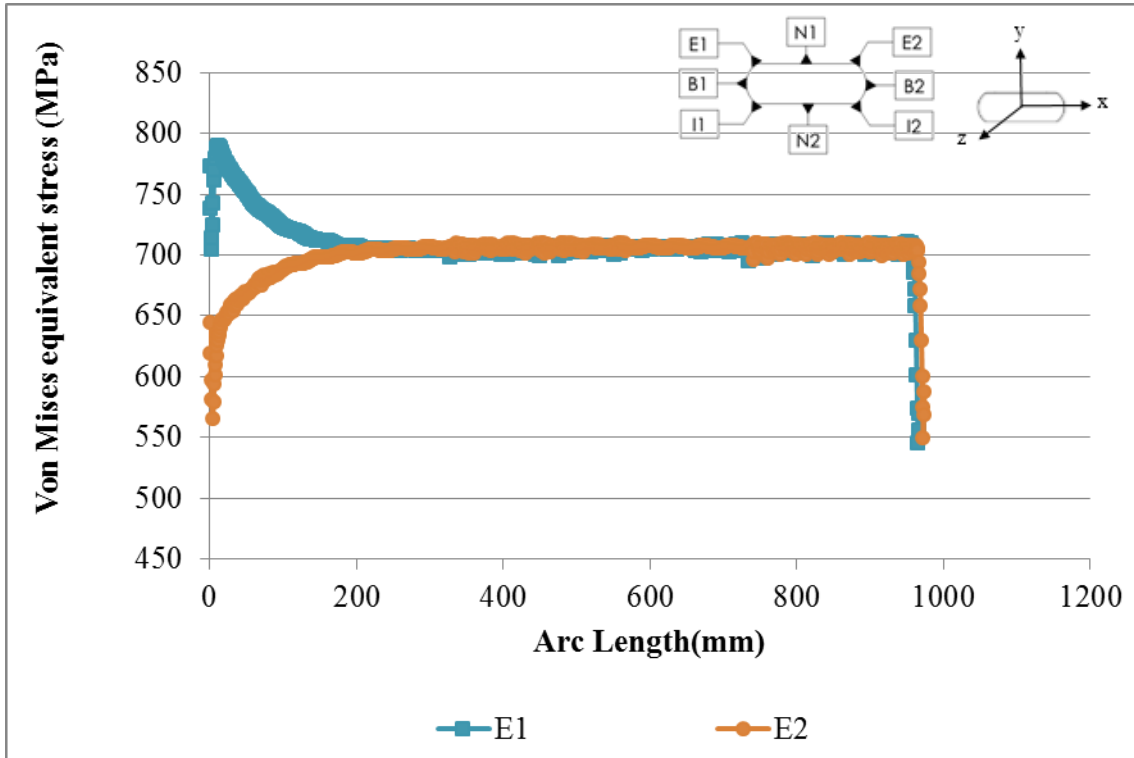


Figure 80. Bending stress due to wire's constraint at face 1 (points E1 and E2).

Finally, the results of the FE are compared to analytical values in Figure 81. The analytical model result is the average of the internal and external armor layers stresses and the FE model result is the average of the stresses at points N1 and N2 in the tensile armor wire. The results presented in Figure 81 are very similar in magnitude and tendency. In the same figure, linear regression curves are fitted to the FE and analytical points showing a good correlation between the two models.

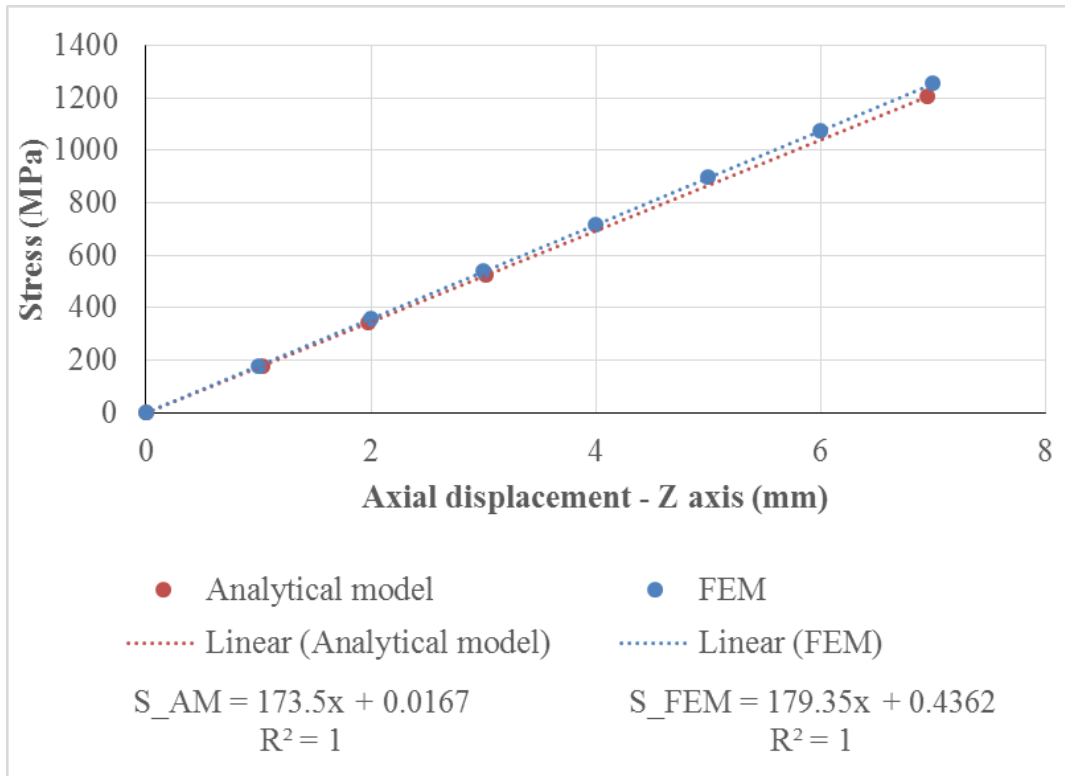


Figure 81. Stress comparison FE x Analytical model.

As a conclusion, the BC (no radial displacement) considered in the FE model seems to be reasonable since the results of this model agreed quite well with the analytical values.

APPENDIX C

CONTACT BETWEEN RESIN AND WIRE – FE MODEL

C.1. RESIN X WIRE CONTACT – FE MODEL X EXPERIMENTAL DATA

In this appendix, a FE model is used to find the best mesh size and also to validate the boundary condition (BC) applied in step 4 of the proposed folding/ unfolding FE model with regard to interaction between the resin and the wire. In step 4, the contact between tensile armor wire and resin is an important parameter to evaluate the stress decay along the wire and the stress relief.

The tensile armor wire and resin geometries are presented in Figure 82 – those dimensions were estimated in CAMPELLO (2014).

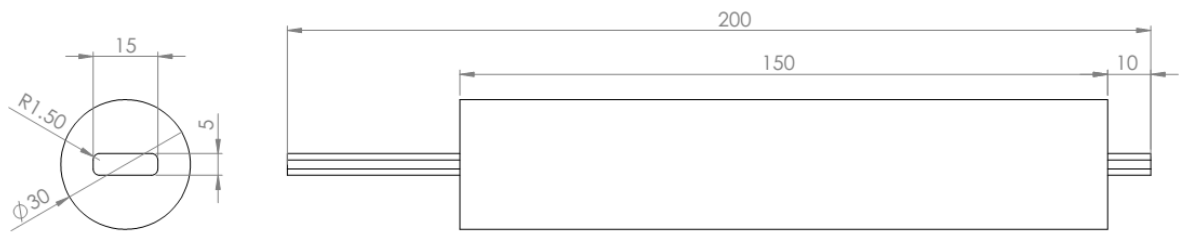


Figure 82. Resin x Wire FE model (dimensions in mm)

The boundary conditions are similar of the folding/ unfolding model. The applied BCs on the model are shown in Figure 83 and explained hereafter:

- a) BC-A – pilot node for displacement at wire section surface.
- b) BC-B – thermal load of 60°C to 20°C (red in Figure 83).
- c) BC-C – fixed surface.
- d) Contact – the contact between armor wire and resin is frictional. The coefficients were adjusted to fit with the experimental data from CAMPELLO (2014).

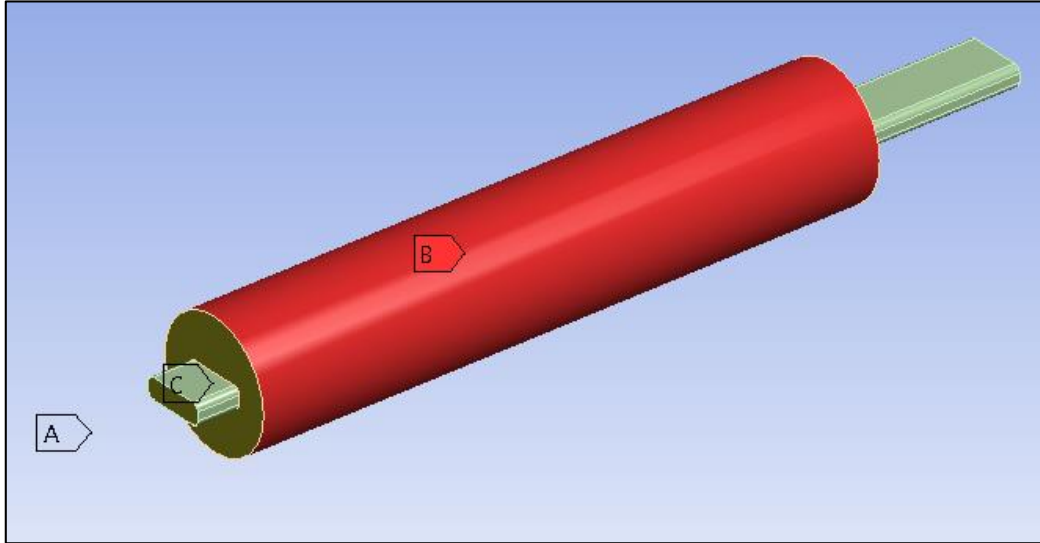


Figure 83. Boundary conditions of the ‘resin x wire’ model

The mesh of this model is hexahedral for the resin and tensile armor wire. The mesh test was performed with only three meshes: the first one with 45266 nodes, the second one with 91215 nodes and the third one with 127446 nodes. Figure 84 shows the mesh 3. The characteristics of all meshes are present in Table 23.

Table 23. Mesh characteristics – ‘resin x wire’ model.

Mesh n°	Resin n° of nodes	Resin n° of elements	Wire n° of nodes	Wire n° of elements	Element type
1	33693	7257	11573	2240	SOLID 186
2	62557	13752	28658	5976	SOLID 186
3	84295	18960	43151	8944	SOLID 186

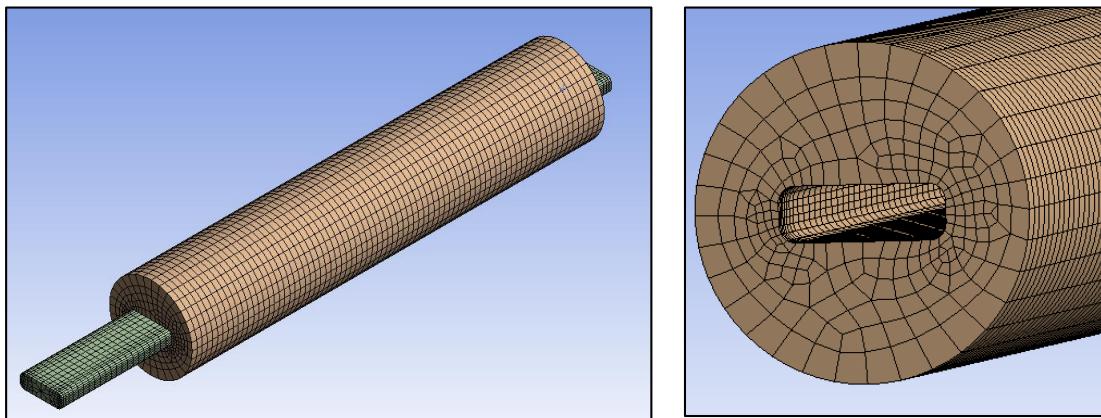


Figure 84. Resin x Wire contact FE model’ mesh n° 3.

C.2. RESULTS AND CONCLUSIONS

In Figure 85 and Figure 86, the colour scale means utilization factor ($UF = \sigma_{VM}/\sigma_y$). The von Mises equivalent stress (σ_{VM}) after the resin contraction (thermal load in Figure 85) and axial load (Figure 86) have the same magnitude of the results presented in CAMPELLO (2014).

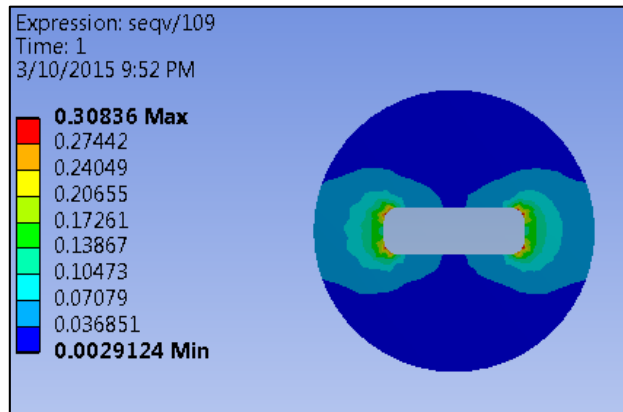


Figure 85. Thermal load result.

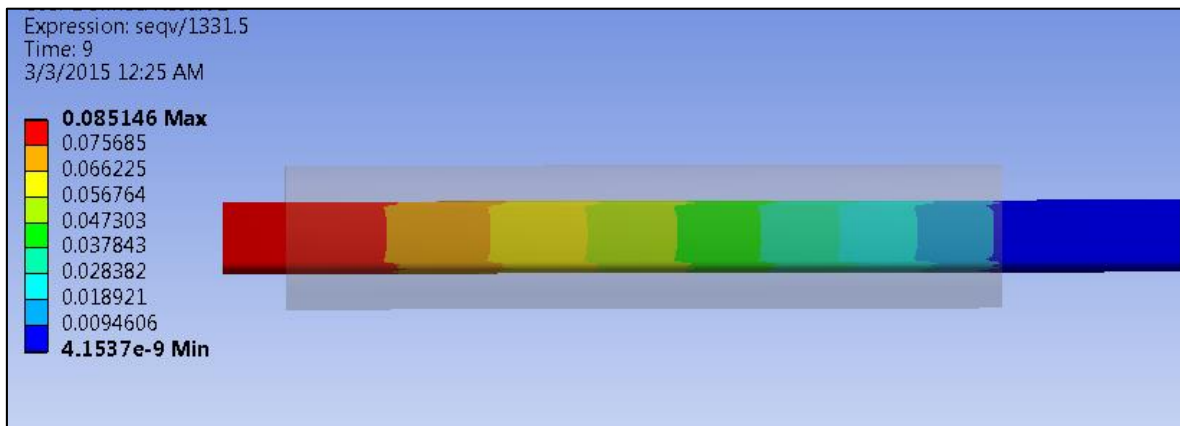


Figure 86. Axial load result.

One of the most important results is the ‘force x displacement’ curve presented in Figure 78, where the FE model results are compared to the experimental data. In order to fit the FE model results with experimental data, the following parameters are adjusted in the frictional contact input parameters: static ($\mu_s = 0.5$) and dynamic ($\mu_d = 0.25$) frictional coefficients and the exponential decay coefficient ($\beta = 0.8$).

In Figure 87, the meshes with 90 k and 125 k nodes (meshes 2 and 3) have the same result and show a good agreement with the experimental data.

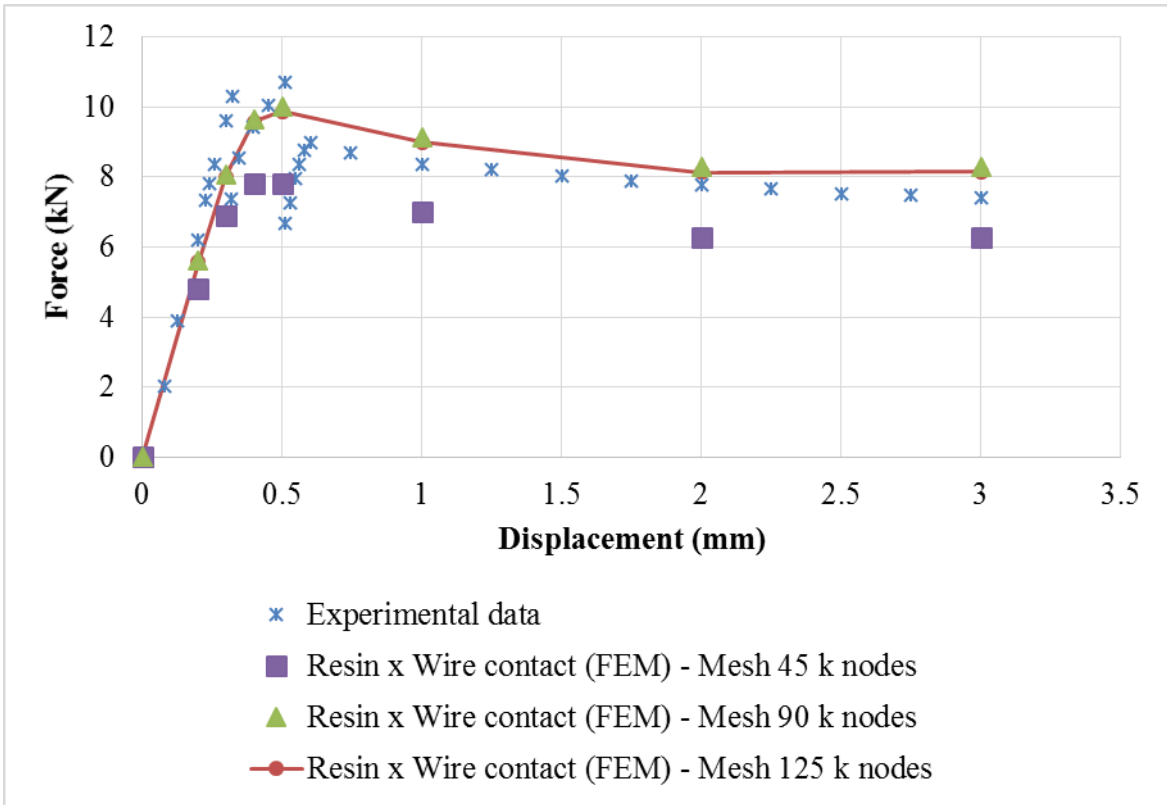


Figure 87. Experimental data x 'resin x wire' model results – experimental data from (CAMPELLO, 2014).